Frustration induced quantum spin liquids and topological properties

Tristan Lugan

THÈSE

Pour obtenir le grade de

DOCTEUR DE L'UNIVERSITÉ GRENOBLE ALPES

Spécialité : **Physique Théorique**

Arrêté ministériel : 25 mai 2016

Présentée par

Tristan LUGAN

Thèse dirigée par **Arnaud RALKO**, maître de conférences à l'Université Grenoble Alpes
codirigée par **Ludovic JAUBERT**, chargé de recherche au Laboratoire Ondes et Matière d'Aquitaine

préparée au sein de **l'Institut Néel, CNRS**
dans **l'École Doctorale de Physique de Grenoble**

Liquides de spin quantiques et propriétés topologiques induites par la frustration

Frustration induced quantum spin liquids and topological properties

Thèse soutenue publiquement le **25/01/2022**,
devant le jury composé de :

Mme Julia MEYER
Professeur à l'Université Grenoble Alpes, Président
M. Sylvain CAPPONI
Professeur à l'Université Paul Sabatier, Rapporteur
M. Tommaso ROSCILDE
Maître de conférences à l'École Normale Supérieure de Lyon, Rapporteur
Mme Laura MESSIO
Maître de conférences à Sorbonne Université, Examinateur

M. Arnaud RALKO
Maître de conférences à l'Université Grenoble Alpes, Directeur de thèse
M. Ludovic JAUBERT
Chargé de recherche au Laboratoire Ondes et Matière d'Aquitaine, Co-directeur de thèse

Acknowledgments

Je tiens tout d'abord à remercier mes deux directeurs de thèse, Arnaud et Ludovic, qui m'ont permis de travailler tout au long de la thèse dans un très bon environnement, malgré les périodes d'isolations liées à la pandémie. Merci d'avoir été là régulièrement pour discuter, répondre à mes questions et m'indiquer des pistes toujours intéressantes à explorer. J'ai appris beaucoup en faisant de la physique à vos côtés et, au-delà du travail, j'ai passé de très bons moments avec vous ces dernières années.

Je remercie ensuite tous mes amis du laboratoire, qu'ils aient fini leur thèse ou non. J'ai passé et continuerai à passer des moments incroyables avec vous. Ces deux dernières années, des circonstances que nous ne pouvons pas contrôler nous on malheureusement séparés plus que nous le voulions. Cependant, je suis fier de la manière dont chacun a traversé cette période difficile, et je n'aurais pas pu le faire sans vous.

Une pensée pour mes amis de Lyon (Bruxelles, Manheim, Nice, Paris et j'en passe) et pour ma famille, que j'aime de tout mon cœur et qui m'ont toujours soutenu dans la voie que j'ai choisi et qui continueront à le faire pendant longtemps. Merci à tous, et à Julien !

Merci aussi à une personne toute particulière qui, non contente de m'inspirer tous les jours, m'a soutenu plus que n'importe qui. Elle se reconnaîtra très certainement.

Enfin, je remercie bien sûr toutes personnes que je n'ai pas déjà cité et avec qui j'ai pu travailler, que ce soit au laboratoire ou pendant mes différentes activités extérieures, en vulgarisation ou à l'université.

Contents

List of Figures

Chapter 1

Introduction

1.1 Frustration in quantum magnetism

Introduced by Toulouse in 1977 to study spin glass physics [1], the term frustration refers to the impossibility to energetically satisfy all interactions in a system. Although not named as such, frustration was already at play in the study of a solid phase of water by Pauling in 1935 [2] where it was responsible for a finite entropy at zero temperature - a phenomenon we will come back to later on, in the case of interacting spins on a lattice. In quantum magnetism, such systems have been the subject of much attention in the past decades for they are expected to host exotic magnetic states. Among them are quantum spin liquids, disordered states hosting fractionalized excitations and exhibiting topological properties. Throughout this manuscript, we will only focus on the study of frustrated spin systems and the exotic magnetic states they give rise to. Let us start by describing the concept of frustration and its effects.

To rapidly grasp the concept of frustration, let us imagine a spin system where the magnetic moments can only take two values $\uparrow$ and $\downarrow$. These spins interact antiferromagnetically which means that the energetically favorable configuration is the one where the two spins are anti-aligned. However, when these spins are placed on a lattice, this favorable configuration cannot necessarily be satisfied for all pairs of spins depending on the geometry of the system. It is the case for the simplest geometrically frustrated unit, the triangle, represented in figure 1.1 (left) with three spins at its vertices. If we satisfy the antiferromagnetic constraint on a bond by fixing two of the three spins, it is then not possible for the third spin to satisfy the two constraints on the two remaining bonds. This is an example of geometric frustration where the spin interactions cannot all be satisfied because of the topology of the system.

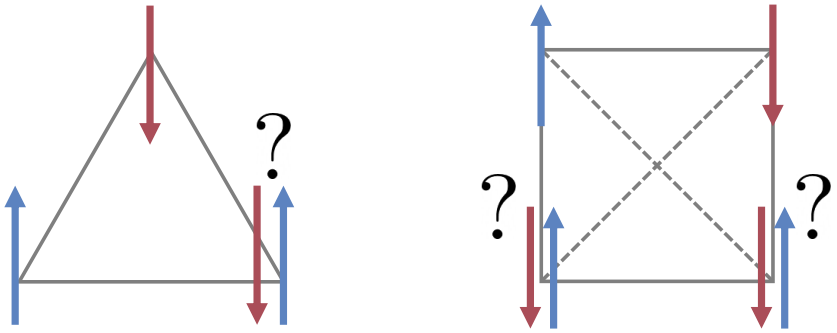

Figure 1.1: Principle of geometrical frustration with antiferromagnetically interacting spins $\sigma = \uparrow, \downarrow$ on the vertices of a triangle (left). Starting by satisfying the antiferromagnetic constraint on a bond by fixing two spins, it is then not possible for the third spin to energetically satisfy the constraints on the two remaining bonds. Principle of frustration due to competing interactions on a square (right). With both nearest-neighbor (gray lines) and next-nearest-neighbor (gray dashed lines) antiferromagnetic couplings on a square, it is impossible to find a spin configuration energetically satisfying all the antiferromagnetic bonds.

Another type of frustration arises when multiple interactions between spins are competing on a lattice. Let us consider the simple example of a square with four spins at its vertices, as represented on figure 1.1 (right). The spins are interacting via a nearest-neighbor coupling (gray lines) and a next-nearest-neighbor coupling (dashed gray lines). Again, fixing two spins to satisfy the antiferromagnetic constraint on a nearest-neighbor bond, it is impossible to find a spin configuration for the two remaining spins that satisfies all the other constraints of the system. In this case, frustration is linked to the competing interactions and not exclusively to the geometry.

It was shown through these two simple examples that frustration, wether due to the geometry or the interactions of the system, corresponds to the impossibility to simultaneously satisfy all bond interactions between two spins. Moving towards more realistic frustrated systems, let us use the isolated triangle of figure 1.1 as a fundamental building block. Connecting these triangular units either by their edges or by their corners yields different types of frustrated lattices, as represented in figure 1.2 by the triangular (upper left) and kagome (upper right) lattices for example. This distinction is related to the fact that frustration induces different effects depending on the connectivity of the lattice, as will be explained in the next section. In two dimensions, the kagome lattice is not the only lattice composed of corner-sharing triangles. A different configuration with triangles arranged around a square yields the square-kagome lattice, as represented in figure 1.2 (bottom left). Finally, frustration also takes place in three-dimensional systems, such as the pyrochlore lattice, where tetrahedral units are also connected by their corners, as in figure 1.2 (bottom right).

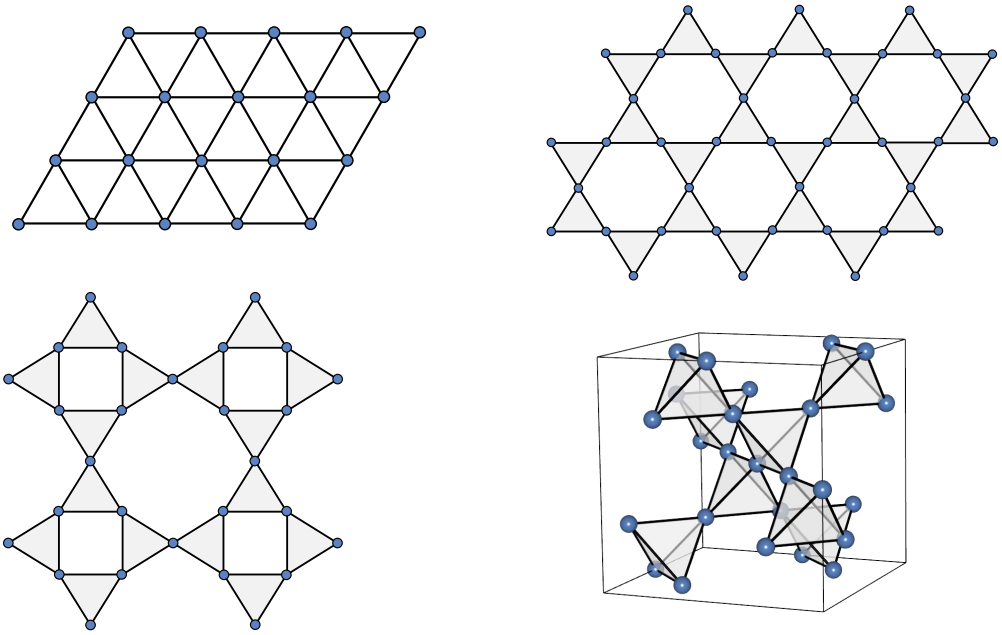

Figure 1.2: Example of frustrated lattices: triangular lattice (upper left), kagome lattice (upper right), square-kagome lattice (bottom left) and pyrochlore lattice (bottom right).

The interesting thing behind these frustrated spin systems, and one of the reason they are thoroughly studied, is the existence of many experimental compounds exhibiting some of the frustrated geometries of figure 1.2. For instance, there are various three-dimensional rare-earth magnets presenting pyrochlore geometry, such as $Dy_2Ti_2O_7$ and $Ho_2Ti_2O_7$ [3, 4]. In two dimensions, there are several compounds formed by Cu^{2+} ion layers surrounded by non-magnetic atoms such as herbertsmithite ($ZnCu_3(OH)_6Cl_2$) [5] for the kagome lattice and the recently synthesized $KCu_6AlBiO_4(SO_4)_5Cl$ for the square-kagome lattice [6]. Each of the compounds cited here are meticulously investigated because they are thought to display exotic magnetic states, such as spin ice physics or potential spin-liquid ground states.

In this manuscript, we will focus on the theoretical study of quantum spin$-1/2$ systems on perfect frustrated lattices in the Mott insulator regime [7], *i.e.* where exactly one electron is localized at each lattice site. The interaction between the spins will be described by the quantum Heisenberg Hamiltonian:

$$\mathcal{H} = \frac{1}{2}\sum_{i,j} J_{ij}\hat{\mathbf{S}}_i \cdot \hat{\mathbf{S}}_j \tag{1.1}$$

where $\hat{\mathbf{S}}_i$ is the quantum spin operator on site i and the couplings are antiferromagnetic with $J_{ij} \geq 0$.

After introducing some effects of frustration as well as the exotic phases it can give rise

to, both in the classical and quantum cases, we will study two frustrated systems by means of the Schwinger boson mean-field theory (SBMFT). After introducing SBMFT and the associated numerical method in chapter 2, we will then turn to the study of the $J_1 - J_2$ Heisenberg model on the square-kagome lattice in chapter 3 which is a perfect example of the stabilization of exotic magnetic states driven by geometrical frustration. Finally, we will study the combined effects of frustration from geometry and competing interactions with the $J_1 - J_2 - J_3$ Heisenberg model on the kagome lattice in chapter 4.

1.2 The classical case

1.2.1 Ground-state degeneracy

Let us first describe some effects of frustration in the classical case, that is, in the limit $S \to +\infty$ where spins can either be considered as $\mathbb{Z}_2$ variables (Ising), as planar vectors (XY) or as three-dimensional vectors (Heisenberg). Taking the example of the unfrustrated square lattice with Ising spins, the ground state of the model is the well-known Néel state, represented on figure 1.3. It is a long-range order defined by two sublattices of spins pointing in opposite directions and characterized by a local order parameter which is the following staggered magnetization:

$$M_{stagg} = \frac{1}{N} \sum_{i=1}^{N} \eta_i \sigma_i^z \tag{1.2}$$

with N the total number of Ising spins σ_i^z and $\eta_i = \pm 1$ depending on the sublattice of the site i.

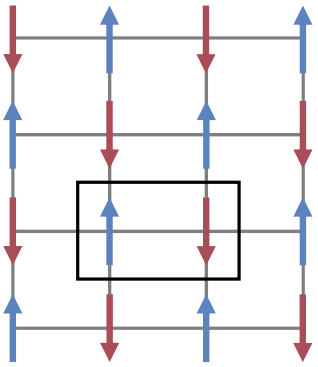

Figure 1.3: Representation of the Néel spin configuration on the square lattice. This long-range order can be defined by a unit cell composed of two sublattices (black rectangle) as well as a non-zero staggered magnetization.

Contrarily to the Néel ground state on the square lattice which is uniquely determined (up to a global rotation), it is simply not possible to define a single ordered ground state for many frustrated systems. In the case of Ising spins on the simple triangular

unit of figure 1.1 (left), the choice of the third spin leaves two different lowest-energy configurations with $E = -J$. Associating many such triangles in order to construct the triangular lattice results in a multiplication of lowest-energy states. This characteristic leads to a finite residual entropy per site at zero temperature $S = k_B \ln \Omega$ with Ω the number of ground states. This means that in this system, the number of lowest-energy states is growing faster than the number of lattice sites. In the thermodynamic limit on the triangular lattice, Wannier showed that the entropy per site has a finite value of $S \simeq 0.323 k_B$ [8]. In other words, this particular system presents an extensive ground-state degeneracy and we consequently define the ground state of the triangular lattice with Ising spins as disordered.

Such disordered phases are called classical spin liquids and cannot be described by any conventional local order parameter. They are, however, characterized by non-zero decaying spin correlations in real space justifying the analogy with liquid states. These correlations can either decay exponentially, which is for instance the case for the Ising model on the kagome lattice [9], or algebraically, in the case of the Coulomb phase on the pyrochlore lattice for example [10]. Finally, these disordered magnetic states can be further characterized by fractionalized excitations such as the magnetic monopoles in spin ice [11, 12]. In the remaining of this section, we will present an example of a classical spin liquid on the kagome lattice before describing some effects of frustration in the quantum case.

1.2.2 Example of a classical spin liquid

The geometry of the lattice is not the only parameter to take into account when studying frustrated systems. The sheer nature of the classical spin, that can either be a $\mathbb{Z}_2$ variable or a vector, also plays a role on the potential disordered nature of the ground state. Let us consider the example of XY spins, *i.e.* planar vectors, on the triangular and kagome lattices with a nearest-neighbor antiferromagnetic coupling J. For both lattices, the Hamiltonian can be expressed through the contribution of each triangular unit as follows:

$$\mathcal{H} = \frac{J}{2} \sum_{\triangle} \left(\mathbf{S}_1 + \mathbf{S}_2 + \mathbf{S}_3 \right)^2 + c \tag{1.3}$$

where each triangle is composed of three sites indexed from 1 to 3 and c is a constant term.

Following equation 1.3, the lowest-energy states on both lattices corresponds to a spin configuration where the sum of the spins on each triangular unit is zero. On a single triangle, this can be achieved in two ways for XY spins (up to a global rotation). These two spin configurations are represented on figure 1.4.

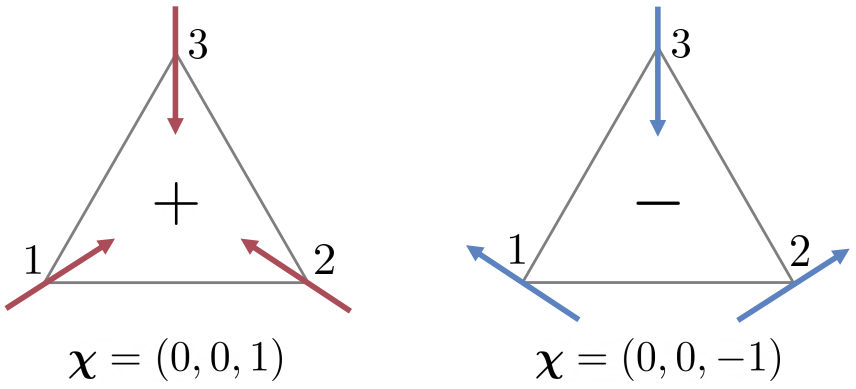

Figure 1.4: Two configurations minimizing the energy for XY spins on a single triangle and associated positive (left) and negative (right) chiralities.

Each of the two configurations of figure 1.4 are discriminated by the vector chirality defined below:

$$\boldsymbol{\chi} = \frac{2}{3\sqrt{3}} \frac{1}{S^2} (\mathbf{S}_1 \times \mathbf{S}_2 + \mathbf{S}_2 \times \mathbf{S}_3 + \mathbf{S}_3 \times \mathbf{S}_1) \tag{1.4}$$

Computing $\boldsymbol{\chi}$ for the left configuration of figure 1.4 we get $\boldsymbol{\chi} = (0, 0, 1)$ while we have $\boldsymbol{\chi} = (0, 0, -1)$ for the right configuration. We can thus discriminate the two lowest-energy configurations on a single triangle by a positive and negative chirality.

A final ingredient playing a role in inducing frustration in a system is the lattice connectivity. We have chosen to look at both the triangular and kagome lattices because they differ in their construction from the initial triangular unit. We have already seen that the triangular lattice is composed of edge-sharing triangles while the kagome lattice is composed of corner-sharing triangles. For the triangular lattice, the choice of the positive or negative chirality on one of the triangle will automatically fix the chirality of all others, as depicted in figure 1.5 (upper pannels). Consequently, the ground state of the triangular lattice will be uniquely determined (up to a global rotation) and corresponds to a long-range order with an entropy per site of $S = 0$ at zero temperature.

For the kagome lattice, on the other hand, fixing the chirality of an initial triangle does not constraint the chirality of the neighboring triangles simply because, unlike on the triangular lattice, the triangular units are connected by their corners. In figure 1.5 (lower pannels), starting from the same triangle with positive chirality, we see that two different spin configurations are already available when taking into account only two other triangular units. This phenomenon, directly linked to the connectivity of the kagome lattice, is responsible for an extensive ground-state degeneracy for XY spins. This degeneracy is described by a Potts model with $q = 3$ colors corresponding to the three possible orientations of the spins [13]. It is also characterized by an entropy per site at zero temperature of $S = 0.168 k_B$ [14].

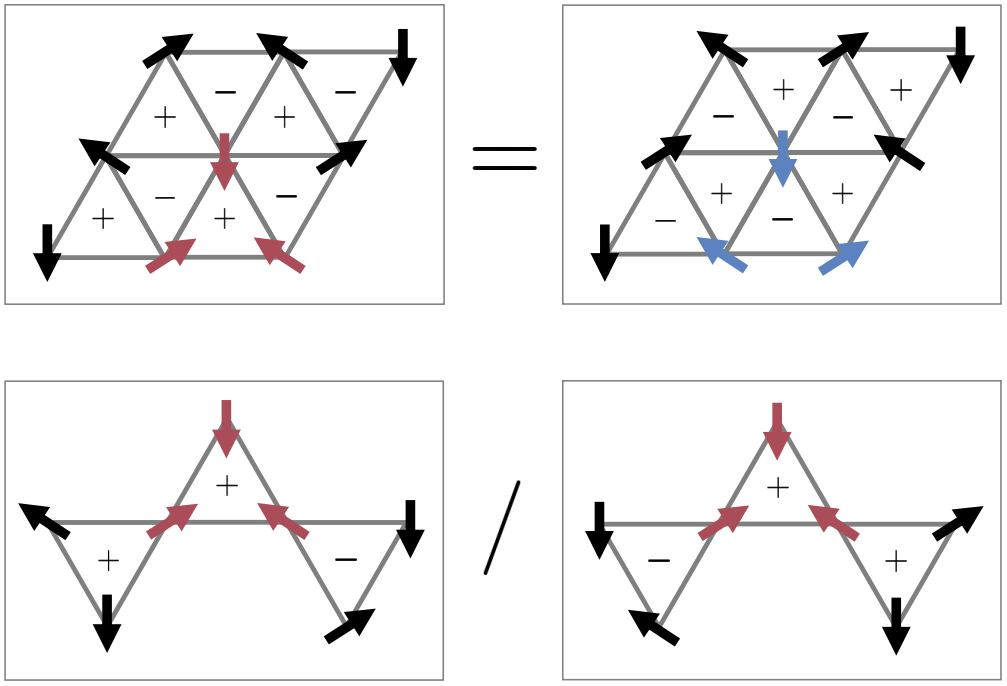

Figure 1.5: Lowest-energy state for XY spins on the triangular lattice starting from an initial triangle with positive (upper left pannel) or negative (upper right pannel) chirality. In the thermodynamic limit, these two states are equivalent since fixing a spin configuration on one triangle constraints the chirality of all the others. Two examples of XY spin configurations on the kagome lattice starting from an initial triangle with positive chirality (lower pannels). Here, fixing a spin configuration on the first triangle does not constraint the chirality of the other triangles of the lattice. This leads to an extensive ground-state degeneracy in the thermodynamic limit.

In the case of Heisenberg spins, *i.e.* three-dimensional vectors, the degeneracy of the ground state is not discrete anymore but becomes continous. Consequently, spins on a triangular unit have an additional rotational degree of freedom while still respecting the constraint $\sum_{\triangle} \left(\mathbf{S}_1 + \mathbf{S}_2 + \mathbf{S}_3\right)^2 = 0$.

Interestingly, in the case of the kagome lattice, a mechanism of order by disorder due to thermal fluctuations selects some specific states out of the ground-state manifold. These entropically favored states correspond to coplanar spin configurations maximizing the entropy of the system [15, 16]. Among which are two noteworthy magnetic orders dubbed $\mathbf{Q} = 0$ and $\sqrt{3} \times \sqrt{3}$ [15–17] that are both represented on figure 1.6.

The $\mathbf{Q} = 0$ order, on figure 1.6 (left), corresponds to the repetition of the same triangular unit inducing the same chirality for all triangles. This spin configuration allows the rotation of specific spins without any energy change. These zero-energy spin excitations span the whole lattice in one of its natural direction and are represented by dashed ovals on figure 1.6 (left). The $\sqrt{3} \times \sqrt{3}$ order, on the other hand, is not defined on a

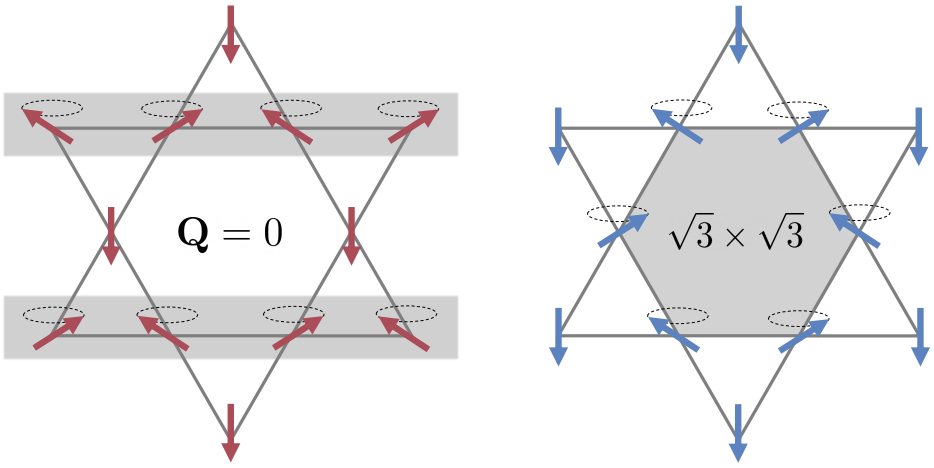

Figure 1.6: $\mathbf{Q} = 0$ ordered configuration on the kagome lattice (left). The zero-energy modes (dashed ovals) span the whole lattice in one of its natural direction (gray area). $\sqrt{3} \times \sqrt{3}$ ordered configuration on the kagome lattice defined on three different triangular units. The so-called weather-vane modes are localized around the hexagons of the lattice.

single triangular unit. The spin configuration is composed of three such triangles, as represented on figure 1.6 (right), and displays alternating chiralities from one triangle to the other. The zero-energy excitations are also slightly different, since they only occur around the hexagons of the lattice. Such localized excitations are called "weather-vane" modes [18–20].

Monte Carlo study of the Heisenberg model on the kagome lattice [17], allows one to study the nature of the state as a function of temperature. A way to do so is to compute the specific heat per spin C/N as a function of the temperature T for large system sizes. Figure 1.7 shows three different regions in the specific heat graph taken from [17]. The first one at high temperature corresponds to the well-known paramagnet state with weak spin correlations between neighboring spins. The second one corresponds to a classical spin liquid (or cooperative paramagnet) with decaying long-distance spin correlations. The final region corresponds to a coplanar state for $T < 0.004J$.

In conclusion, we have shown an example of disordered classical spin-liquid states on the frustrated kagome lattice. We will now explore the different unconventional phases frustration can give rise to in the quantum case.

1.3 The quantum case

As the spin length S gets smaller and close to 1/2, as is the case for the Cu^{2+} ions in many experimental compounds, considering zero-point motion caused by the Heisenberg uncertainty principle becomes compulsory. Such quantum fluctuations can sometimes lead

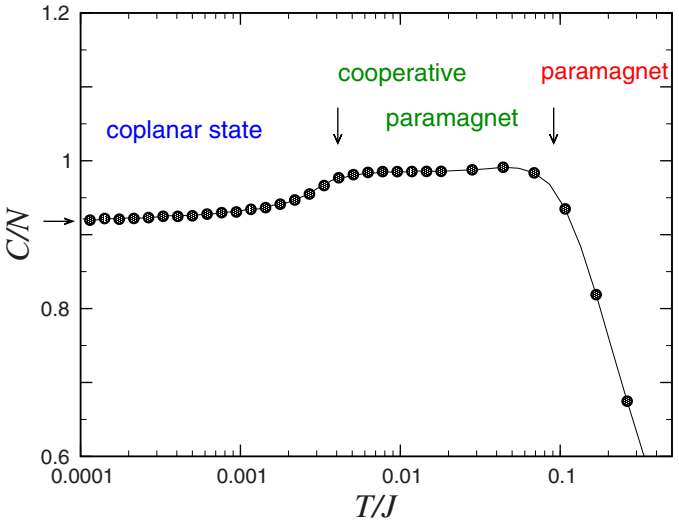

Figure 1.7: Monte Carlo temperature dependence of the specific heat for a finite size kagome lattice with Heisenberg spins, taken from [17]. The specific heat shows three different regions where the ground state of the model is either a coplanar ordered state, a classical spin liquid (or cooperative paramagnet) or a conventional paramagnet.

to rather simple perturbative effects on the classical ground states. On the square lattice antiferromagnet, for instance, the quantum ground state corresponds to a semi-classical order with a Néel spin configuration where quantum fluctuations cause a reduction of the staggered magnetization from $M = 0.5$ in the classical case to $M \simeq 0.307$ in the quantum case [21, 22]. In this section, we will describe stronger quantum effects linked to frustration as well as the unconventional phases they can give rise to.

1.3.1 Valence bond crystals

Classically, two spins coupled antiferromagnetically by J are in their lowest-energy state when they are anti-aligned. For quantum spins, this is not the case because of the presence of a spin-0 singlet state with energy $E_s = -3J/4$. Such a singlet state on a bond between spins $\hat{\mathbf{S}}_a$ and $\hat{\mathbf{S}}_b$, dubbed $|ab\rangle$, is schematically represented on figure 1.8 (left). In the case of two quantum spins, the singlet state is separated by an energy gap $\Delta E = J$ from the three degenerate triplet states with $E_t = J/4$, as represented on figure 1.8 (right). ΔE, also called spin gap, corresponds to the energy required to break a singlet creating two unpaired spins.

The valence bonds, where two spins are maximally entangled, are the building block of many magnetic quantum phases. For instance, it is possible to arrange such singlets on the nearest-neighbor bonds of the square lattice so that each spin belongs to only one valence bond. Some of these arrangements correspond to ordered configurations of nearest-neighbor singlets, also called valence bond crystals (VBC). Two such ordered patterns of singlets on the square lattice are represented on figure 1.9.

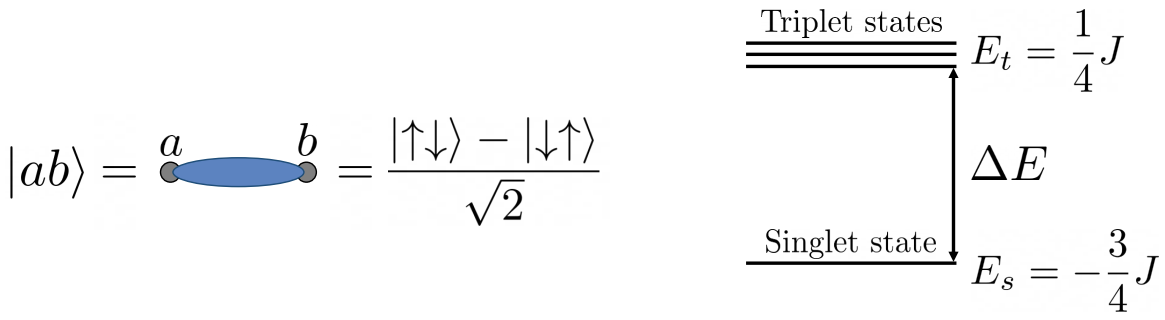

Figure 1.8: Singlet state schematization on a bond between two spins $\hat{\mathbf{S}}_a$ and $\hat{\mathbf{S}}_b$ (left). Energies of the singlet state and the three triplet states for two quantum spin$-1/2$ separated by a spin gap Δ_E (right).

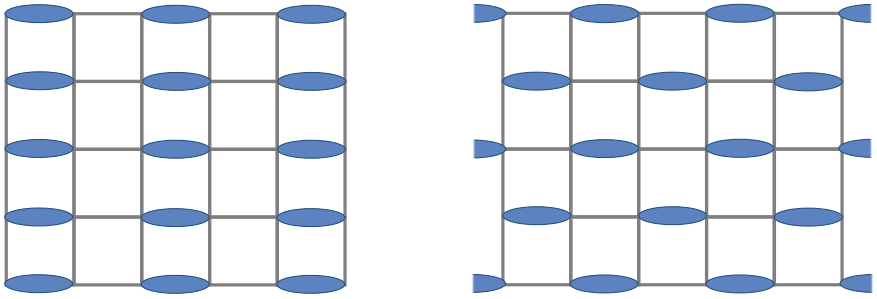

Columnar VBC Staggered VBC

Figure 1.9: Two valence bond crystal states on the square lattice. Here, valence bonds are located on the nearest-neighbor bonds of the lattice and each spin belongs to one singlet only. Both the columnar VBC (left) and the staggered VBC (right) break the translational and rotational symmetries of the lattice.

In both the columnar and staggered valence bond crystals of figure 1.9, the translational and rotational symmetries of the lattice are broken. In the frame of Landau's theory of phase transitions, this symmetry breaking characterizes an ordered phase. The ordered nature of the VBC states are further confirmed by their dimer correlations in real space that do not go to zero for arbitrary large distances. The spin correlations in real space do go to zero meaning that the spins in such VBC states are disordered. However, these VBC states are not eigenstates of the Hamiltonian, except in rare cases [23]. Still, VBC states can be found as the ground state of effective models [24]. For instance, the phase diagram of the quantum dimer model on the triangular lattice contains three different VBC states as well as a spin liquid phase [25].

Another valence bond configuration on the square lattice is the plaquette VBC represented on figure 1.10 (left), which breaks the translational but not the rotational symmetry of the lattice. Each square plaquette is formed by two resonating singlet configuration around a square as depicted in figure 1.10 (right). The valence bond being subject to quantum fluctuations, it is common to observe resonance processes between

different valence bond configurations on closed loops, with the probability to observe such configurations decaying exponentially with the length of the loop. The possibility to consider resonating singlet configurations is in fact at the heart of the resonating valence bond (RVB) theory which allows one to construct disordered magnetic states with no long-range order of the valence bonds.

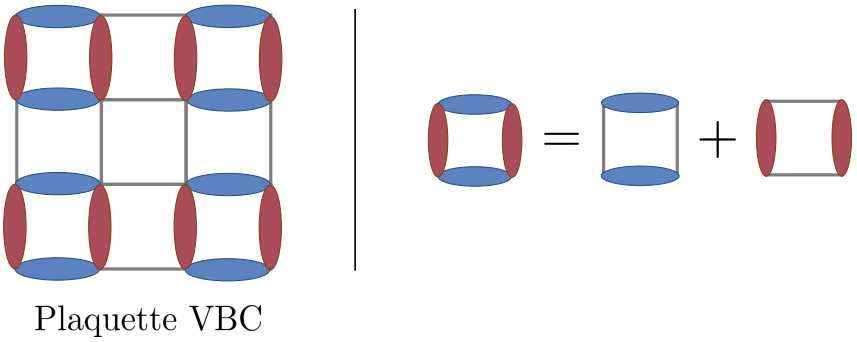

Figure 1.10: Plaquette valence bond crystal on the square lattice (left). Each resonating plaquette is a superposition of two valence bond configurations around a square (right).

1.3.2 RVB states

Resonating valence bond states were first introduced in 1987 by Anderson as a potential connection between quantum spin liquids (QSL) and high-temperature superconductivity [26, 27]. These states are based on a superposition of different valence bond coverings of the lattice. The previous valence bond crystals of figure 1.9 are a good example of such coverings. A more formal definition would be:

$$|c\rangle = |ab\rangle \otimes |cd\rangle \otimes \cdots \otimes |yz\rangle \tag{1.5}$$

which corresponds to a product of singlet states on the bonds of the lattice where every spin belongs to exactly one singlet.

Then, the resonating valence bond wavefunction $|\Psi\rangle$ is defined as the following superposition:

$$|\Psi\rangle = \sum_c \phi(c)\,|c\rangle \tag{1.6}$$

where the summation is over all possible valence bond covering c on the lattice. The $\phi(c)$ are the weights associated to each covering in the superposition.

In this formalism, the VBC states of figure 1.9 would then correspond to weights of $\phi(c) = 0$ except for the associated ordered valence bond covering made of nearest-neighbor singlets. In the RVB theory, however, singlets are not restricted to nearest-neighbor bonds and the superposition of equation 1.6 can be composed of many different

long-range valence bond coverings. A schematic representation of such a RVB state is given in figure 1.11. This means that the RVB wavefunctions are not restricted to valence bond crystals. For instance, the quantum state described by an RVB wavefunction $|\Psi\rangle$ can in some cases, *i.e.* with appropriate $\phi(c)$ coefficients and long-range singlets coverings, correspond to a semi-classical long-range order, such as the Néel order on the square lattice [21]. In many cases, if the distribution of these coverings is broad, there is no preference for a particular valence bond covering meaning that all the symmetries of the system are restored. Such disordered states correspond to quantum spin liquids.

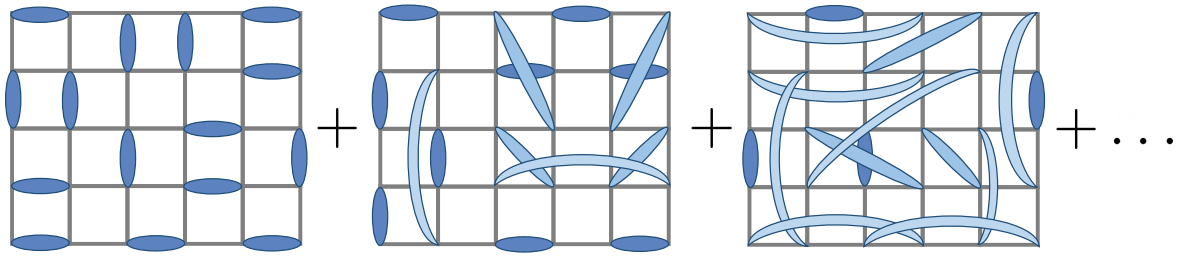

Figure 1.11: Schematic representation of a resonating valence bond state on the square lattice. This state is composed of many different valence bond coverings that can contain both short-range (darker blue) and long-range (lighter blue) singlets.

1.3.3 Quantum spin liquids

We have seen above that RVB states can describe many different magnetic quantum ground states from semi-classical orders to quantum spin liquids. A generic feature of RVB wavefunctions associated to quantum spin liquids is that they are completely symmetric and cannot be described by any local order parameter [28]. Thus, they exhibit no long-range order on any spin, dimer or higher-order correlation functions, contrarily to magnetic orders or valence bond crystals.

Another feature distinguishing valence bond crystals and quantum spin liquids is the nature of their spin excitations. For a VBC, the simplest spin excitation corresponds to the breaking of a valence bond which is depicted on figure 1.12 (left) and resulting in the creation of a magnon. This process, originating for instance from the inelastic scattering of a neutron, modifies the total spin of the system of $\Delta S = 1$ and changes the singlet $|ab\rangle$ to a spin-1 triplet state $|\uparrow_a\uparrow_b\rangle$. In an ordered valence bond covering, it is impossible to separate the two resulting spins because of the energy cost caused by rearranging the singlets. This is illustrated in figure 1.12 (right), where bonds are highlighted in red when a singlet had to be rearranged in order to separate the two spins.

The red path in figure 1.12 (right) can be compared to a string with tension [29] connecting the two spins. The spin-1 excitation in this VBC state cannot be decomposed

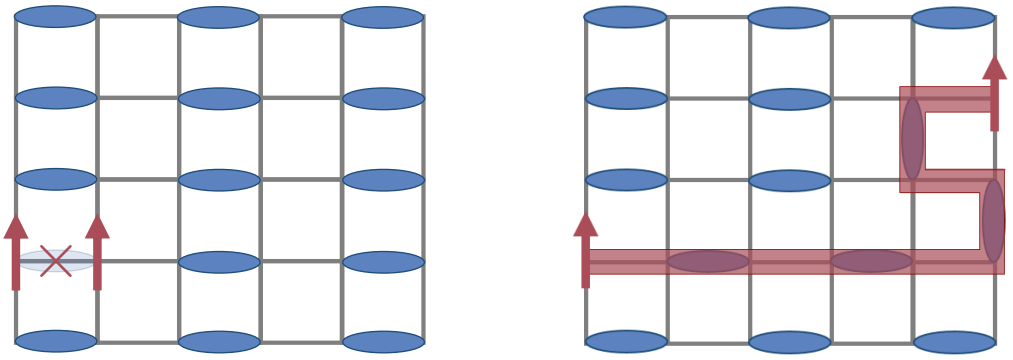

Figure 1.12: Triplet excitation for a valence bond crystal. This excitation corresponds to the breaking of a singlet with a change of spin $\Delta S = 1$ (left). These two spins cannot be separated by an arbitrary large distance because of the energy cost of rearranging the valence bonds on the latice. The bonds requiring a rearrangement of the singlets are highlighted in red.

into two separate spin$-1/2$ excitations, called spinons, that can freely propagate on the lattice. This is not the case for quantum spin liquids. Indeed, since the RVB ground state is composed of a superposition of many valence bond coverings, moving apart the two spins from the triplet state simply consists in reshuffling the valence bond coverings in the superposition [28]. In other words, for a quantum spin liquid, the red string of figure 1.12 (right) becomes tensionless so that the initial spin-1 excitation becomes two spin$-1/2$ excitations. These spinons correspond to fractionalized excitations, since they only carry a fraction of the spin of the original triplet excitation. In a QSL phase, the spinons are deconfined since they can freely propagate while they are confined in a VBC state.

These fractionalized excitations can be of several types. Spinons can be gapped, meaning they correspond to an excitation of finite energy, or gapless. They can also obey different statistics corresponding to either bosons, fermions or even anyons [29]. This variety of excitations reflects the variety of possible quantum spin liquids. Indeed, in the framework of RVB theory, it is possible to construct different kind of quantum spin liquid states. First, by considering only short-range valence bond coverings in the superposition of equation 1.6, it is possible to get gapped spin liquid states, called $\mathbb{Z}_2$ spin liquids. Second, by considering enough long-range valence bond coverings, the RVB function can describe gapless spin liquids, called U(1) spin liquids. These are also called algebraic spin liquids because many of their correlation functions are decaying algebraically. We will provide now a simplistic explanation of the gapped or gapless nature of these phases. For $\mathbb{Z}_2$ spin liquids, all valence bond coverings in the superposition are short-range meaning that any valence bond requires a finite energy to break. The spinons are then gapped excitations. For U(1) spin liquids, on the other hand, since

some singlets connects spins at an arbitrary large distance, the energy cost of breaking such singlets becomes negligeable and spinons are then gapless.

Inside the $\mathbb{Z}_2$ and U(1) categorizations, many different quantum spin liquid phases exist and it is interesting to try to classify them on specific models. For instance, Wen found 196 different $\mathbb{Z}_2$ spin liquids compatible with the spin$-1/2$ Heisenberg antiferromagnet on the square lattice [30]. This study was carried out using a projective symmetry group approach through a parton construction of the Hamiltonian. This method allowed the classification of mean-field spin-liquid states respecting all the symmetries of the studied system. We will further describe the projective symmetry group approach in the next chapter, in the case of the Schwinger boson mean-field theory.

Finally, some quantum spin liquids possess the distinguishing characteristic of not respecting all the symmetries of the system. A first example are the spin liquid states with hidden nematic order that break the rotational symmetry of the lattice and that can be found for instance in the triangular lattice with four particle ring-exchange [31]. A second example are chiral spin liquids, breaking the time-reversal symmetry of the system, that can be found for instance in the Schwinger boson framework as the ground state of the kagome spin$-1/2$ antiferromagnet [32]. We have actually encoutered both kinds of spin liquids as the ground state of two different frustrated systems studied in chapters 3 and 4.

Now that we have described essential concepts behind frustration and its effect on magnetic systems, we will end this chapter by showing concrete applications of these concepts in the form of an overview of recent works on two frustrated magnetic systems.

1.4 Application to concrete models

1.4.1 The paradigmatic kagome lattice

The possibility to discover exotic quantum states, such as the ones presented above, has been even more strengthened by the synthesis of experimental compounds exhibiting various frustrated geometries. The most famous example of such compounds undoubtedly being herbertsmithite where Cu^{2+} layers form a perfect two-dimensional kagome lattice with spin $S = 1/2$, as represented on figure 1.13. We have already described some characteristics of the kagome antiferromagnet in the classical case in section 1.2.2. In the quantum case, the spin$-1/2$ Heisenberg model with nearest-neighbor couplings is an archetypal example of how complex the determination of the ground state of a frustrated system can be. Indeed, the nature of this model's ground state is a long-standing debate both from a theoretical and experimental standpoint.

The quantum Heisenberg model on the kagome lattice has been extensively studied in the

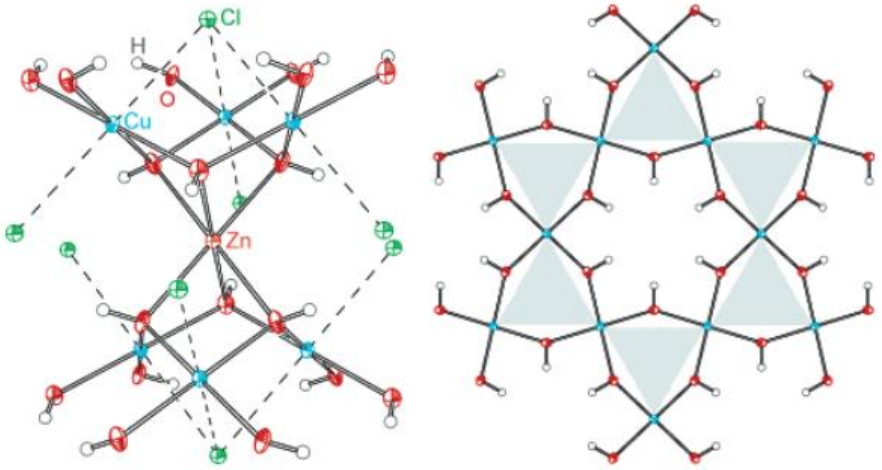

Figure 1.13: Three-dimensional crystal structure of the experimental compound herbertsmithite (left). Two-dimensional kagome layers formed by the Cu^{2+} ions in blue (right). Figure taken from [5].

past decades. Still, the exact nature of its ground state remains difficult to determine and a plethora of potential ground-state candidates have been proposed over the years using many different numerical methods. Among these candidates are quantum spin liquids, in particular gapless U(1) Dirac spin liquids [33–39], gapped $\mathbb{Z}_2$ spin liquids [40–42] and even a chiral spin liquid [32]. Several VBC states were also proposed [38, 43–45].

The use of numerical methods to determine the ground state of this system is paramount since the quantum Heisenberg Hamiltonian is analytically intractable. This is why the above studies on the kagome lattice employed a variety of numerical methods including quantum Monte Carlo [33–35], exact diagonalization [39], density matrix renormalization group (DMRG) [37, 40–42], quantum dimer model derivations [38, 45], Schwinger boson mean-field theory [32] as well as other methods [36, 43, 44]. Unfortunately, each method contains biases or approximations hindering a definitive answer on the exact nature of the ground state. For instance, exact diagonalization does not imply any approximations but is limited to rather small system sizes while other techniques such as the Schwinger boson mean-field theory simply cannot take into account all correlations.

Another route to realize a quantum spin-liquid ground state on the kagome lattice is to turn to experimental results on availabe compounds. In the case of the kagome lattice, several experimental compounds are available and are usually studied through magnetic susceptibility measurements, muon spin relaxation, NMR, inelastic neutron scattering or thermodynamic measurements. For the structurally perfect spin$-1/2$ kagome antiferromagnet realized in herbertsmithite, the exact nature of the ground state is not yet completely understood since there is still a debate on the ground state's low-energy magnetic excitations that could either be gapped or gapless [46, 47]. Moreover, the physics

in herbertsmithite displays two main deviation from the standard Heisenberg Hamiltonian with a simple antiferromagnetic coupling J. First, because of a non-negligeable Dzyaloshinskii-Moriya interaction with an amplitude $D/J \sim 0.06$ [48, 49] due to spin-orbit coupling and second, because of site mixing between Cu^{2+} and Zn^{2+} ions in the magnetic layers [50].

The other kagome compounds do not provide a definitive answer either. For instance, the compound vesignieite [51] also presents kagome layers with $S = 1/2$ and nearest-neighbor coupling J. However, the ground state corresponds to a long-range order below $T = 9$ K [52] which is probably linked to a rather strong Dzyaloshinskii-Moriya interaction of $D/J \sim 0.14$ [53]. Other compounds exist but their physics is usually defined by further-neighbor couplings and yield a variety of ground states ranging from a gapless spin liquid in kapellasite [54] to a long-range order in volborthite [55] as well as a VBC in $Rb_2Cu_3SnFn_{12}$ [56].

In the end and despite varying results from different approaches, there seems to be an agreement on the disordered nature of the ground state as well as the presence of a considerable number of low-lying singlet states below the first magnetic excitation [57–59] for the spin$-1/2$ kagome antiferromagnet. These numerous singlet states are yet another indicator of the richness of this system where the presence of many competing ground-state candidates hinders the exact determination of the true ground state.

1.4.2 An overview of the square-kagome lattice

Stepping aside from the problematic ground state determination on the kagome lattice, let us turn to another frustrated system with promising exotic ground-state candidates. The square-kagome lattice [6, 60–70], also named shuriken lattice [71, 72], squagome lattice [73, 74] or L4-L8 net [75], is composed of corner-sharing triangles like the kagome lattice. It is further characterized by two inequivalent sublattices u and v as well as two different nearest-neighbor couplings J_1 and J_2, which are represented in figure 1.14. Interest in determining the ground state of the associated spin$-1/2$ Heisenberg model was further spurred by the recent synthesis of the experimental compound $KCu_6AlBiO_4(SO_4)_5Cl$ with square-kagome geometry and spin $S = 1/2$ [6].

The idea behind this final section is to provide an overview of recent progress made in determining the ground state of this system both theoretically and experimentally which will add some context to the study presented in chapter 3. We will start by unveiling some results on the classical and quantum phase diagrams obtained via analytical and numerical approaches to finally present recent experimental results obtained on the experimental compound.

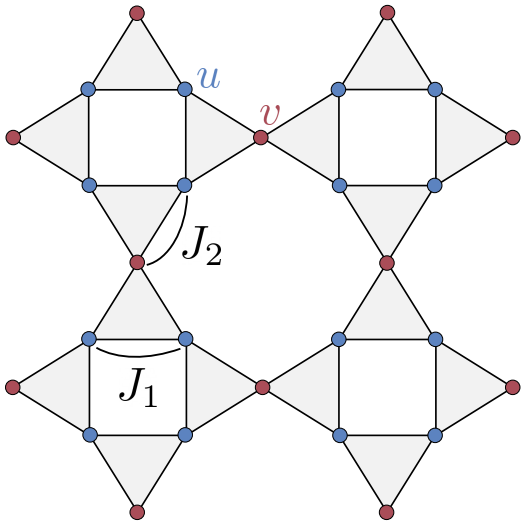

Figure 1.14: Representation of the square-kagome lattice with its two inequivalent sublattices u and v. The antiferromagnetic coupling J_1 connects two neighboring u sites on a square plaquette while J_2 connects neighboring u and v sites.

1.4.2.1 Classical Phase Diagram

The phase diagram of the square-kagome lattice has been studied for Ising spins by Pohle *et al.* [72] as a function of temperature and the ratio $x = J_2/J_1$. It is represented on figure 1.15 (a) and was computed using a combination of numerical Monte Carlo simulations as well as analytical Husimi-tree calculations.

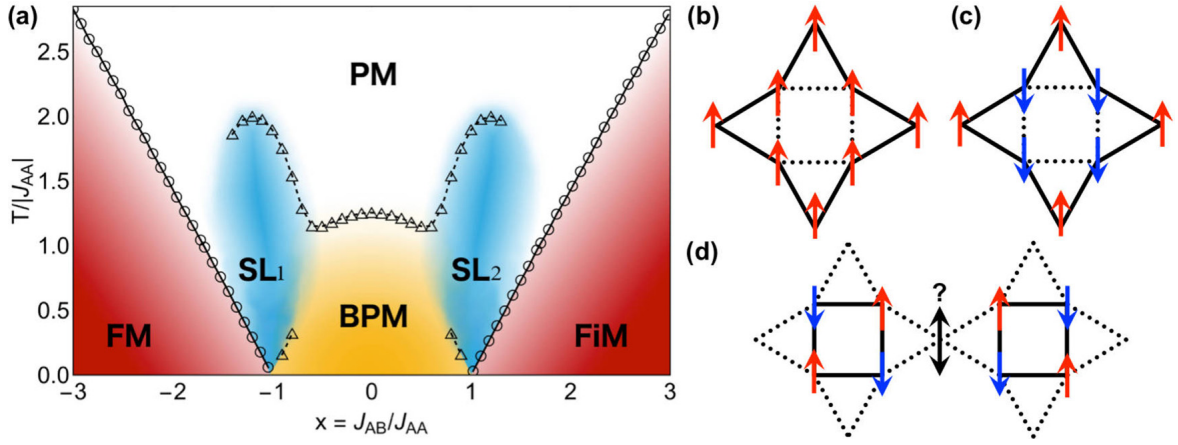

Figure 1.15: Classical phase diagram for the Ising model on the square-kagome lattice as a function of $x = J_2/J_1$ and $T/|J_1|$ (a). There are six different ground states: two long-range orders with ferromagnetic or ferrimagnetic spin configurations as well as four disordered phases, among which a paramagnetic state, a binary paramagnet and two spin liquids. Representation of the ferromagnetic and ferrimagnetic ordered spin configurations as well as the binary paramagnet state (b)-(d). In the binary paramagnet state, spins on the u sites form antiferromagnetically-ordered square plaquettes decoupled from the v site spins. Figure taken from [72].

For $T = 0$, the classical ground state is ordered for $|x| > 1$ with either ferromagnetic or ferrimagnetic long-range orders, see figure 1.15 (b) and (c). The ferrimagnetic order corresponds to a spin configuration with ferromagnetically-ordered square plaquettes formed by the u sites with v site spins pointing in the opposite direction. This phase is reminiscent of Lieb ferrimagnetism [76] with a total moment $M = 1/3$ despite the two antiferromagnetic couplings J_1 and J_2. For $|x| < 1$, however, the ground state is composed of antiferromagnetically-ordered square plaquettes which are completely decoupled from the v site spins. In other words, this disordered phase, named binary paramagnet, can be described by two different and completely uncorrelated degrees of freedom: the spins on the v sites and the "superspins" formed by the antiferromagnetic square plaquettes. At high temperature, we unsurprisingly find the paramagnetic state. For intermediate temperature and around $x = 1$, two spin-liquid phases appear with an extensive ground-state degeneracy, dubbed SL_1 and SL_2. They exhibit exponentially decaying spin correlations but are still distinguishable from the paramagnetic state by their inhomogenous static structure factor. In short, this phase diagram is very rich and contains multiple phase transitions (resp. crossovers) between both disordered and ordered ground states, represented by circles (resp. triangles) on figure 1.15 (a) and obtained via Monte Carlo simulations (resp. Husimi-tree calculations).

Another very interesting phenomenon emerging in this model is the reentrance mechanism occuring between the paramagnetic and binary paramagnet phases, which can be observed for instance at $x \approx 0.9$ on figure 1.15 (a). While reentrance is usually used to characterize the presence of a disordered phase between two ordered ones [77, 78], this notion is slightly twisted in this system. Indeed, starting from the paramagnetic phase around $x = 0.9$ and lowering the temperature, two crossovers take place to yield first a spin-liquid phase and finally the binary paramagnet, so that both the low- and high-temperature ground states are less correlated than the intermediate one. This behavior can also be observed through key features such as the nonmonotonic behavior of the reduced susceptibility, double peaks in the specific heat, an entropy plateau as well as a multistep Curie law crossover [72]. This reentrance phenomenon is another example of the effects of frustration and competing disordered phases in a magnetic system.

As for the case of classical Heisenberg spins, the phase diagram at zero temperature was obtained in [75]. It is composed of a spin-liquid phase with extensive ground-state degeneracy for $x < 2$ as well as a ferrimagnetic long-range order for $x > 2$. Similarly to the kagome lattice, the Heisenberg Hamiltonian can be decomposed as a sum of the following contribution $\mathcal{H}_\triangle$ for each triangular unit of the square-kagome lattice:

$$\mathcal{H}_\triangle = J_1 \mathbf{S}_1 \cdot \mathbf{S}_2 + J_2 \mathbf{S}_2 \cdot \mathbf{S}_3 + J_2 \mathbf{S}_3 \cdot \mathbf{S}_1 \tag{1.7}$$

The classical Heisenberg phase diagram can then be understood as a result of the minimization of the energy on each triangular units. This yields a coplanar configuration defined as:

$$\begin{cases} \mathbf{S}_1 = \mathbf{x} \\ \mathbf{S}_2 = \cos(\phi_2)\mathbf{x} + \sin(\phi_2)\mathbf{y} \\ \mathbf{S}_3 = \cos(\pi + \frac{\phi_2}{2})\mathbf{x} + \sin(\pi + \frac{\phi_2}{2})\mathbf{y} \end{cases} \tag{1.8}$$

where we have chosen $(\mathbf{x}, \mathbf{y})$ as the plane of reference. The value of ϕ_2 as a function of x is determined by:

$$\phi_2 = \begin{cases} \cos^{-1}(\frac{x^2}{2} - 1), & 0 \leq x \leq 2 \\ 0, & x \geq 2 \end{cases} \tag{1.9}$$

This result is coherent with the 120° ordering of the spins on a triangle at $x = 1$, reminiscent of the $\mathbf{Q} = 0$ or $\sqrt{3} \times \sqrt{3}$ states on the kagome lattice. It is also coherent with the ferrimagnetic order presented above for $x > 2$.

1.4.2.2 Quantum Phase Diagram

Despite many studies on the magnetic and thermodynamic properties of the square-kagome lattice in presence of a magnetic field [61–67, 69–71, 75] only a few works have been interested in its quantum phase diagram and potential ground states at zero field and zero temperature beyond the $x = 1$ point [70, 75]. Still, early works at the point $x = 1$ agree on the disordered nature of the ground state and on the presence of a considerable number of low-lying singlet states below the first magnetic excitation [60, 64, 71, 73], similarly to the kagome lattice [57].

The quantum phase diagram in the full $x > 0$ region was studied for the first time by Rousochatzakis *et al.* [75] using exact diagonalization up to $N = 30$ sites, analytical strong-coupling theories and a resonating valence bond approach based on quantum dimer model derivations. First, in the limit $x \gg 1$, the ground state is a semi-classical long-range order corresponding to Lieb ferrimagnetism [76], reminiscent of the classical case. Here, quantum fluctuations are reducing the spin length but preserve the total moment of $M = 1/3$. This phase becomes the ground state for a value of x slightly smaller than the classical boundary of $x = 2$ for Heisenberg spins. On the other side of the phase diagram in the strong-coupling regime, *i.e.* for $x \ll 1$, the spins on the u sites form resonating square plaquettes, similarly to figure 1.10. As for the spins on the v sites, an infinitesimal J_2 is responsible for the presence of effective couplings between v sites stemming from virtual plaquette excitations. These couplings stabilize a crossed-dimer valence bond crystal, depicted in figure 1.16 and dubbed p-CD-VBC, with p standing for the resonating plaquettes.

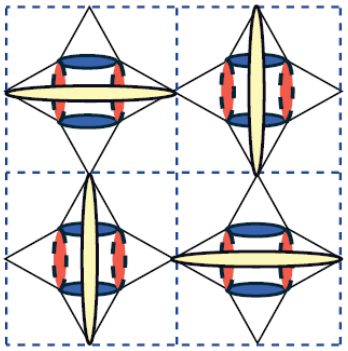

p-CD-VBC

Figure 1.16: Representation of the crossed-dimer valence bond state on the square-kagome lattice. The blue and red ovals denote resonating square plaquettes while yellow ovals correspond to singlets between v sites. Figure taken from [75].

The intermediate regime, for $1 \lesssim x \lesssim 2$, contains many competing low-lying singlet states below the first magnetic excitation and has proven harder to treat. Exact diagonalization points to at least two separate phase transitions in this regime, with corresponding ground states labelled "Ya" and "Yb". The exact diagonalization quantum phase diagram in the presence of a magnetic field is displayed in figure 1.17. The four phases we have just described and their region of stability are present at zero field in this diagram. We will not discuss the several other magnetic states present at higher fields in figure 1.17. The possibility of additional ground states between the Yb phase and the ferrimagnetic long-range order is not ruled out. Unfortunately, exact diagonalization results remain inconclusive in this regime due to limitations in system size.

To gain more insight, the resonating valence bond picture was used to determine the resonance processes controlling the physics of the ground state in the region around $x = 1$ [75]. On the square-kagome lattice, the dominant tunneling process corresponds to the resonating square plaquettes formed by the u sites. Contrarily to the strong-coupling regime, it is not energetically favorable to have resonating singlets on all square plaquettes with no singlets on the v sites. Around $x = 1$, the ground state that maximizes the presence of square plaquettes on the lattice rather corresponds to the pinwheel valence bond crystal represented on figure 1.18 (left) where one in two square plaquettes present resonating singlets.

The discrepancies between the exact diagonalization and resonating valence bond approaches of [75] suggest that quantum fluctuations beyond the nearest-neighbor valence bond basis should be taken into account. The associated longer-range resonant processes were later considered in [68]. This study challenged the pinwheel VBC scenario by putting forth another valence bond crystal, called loop-six VBC and represented in

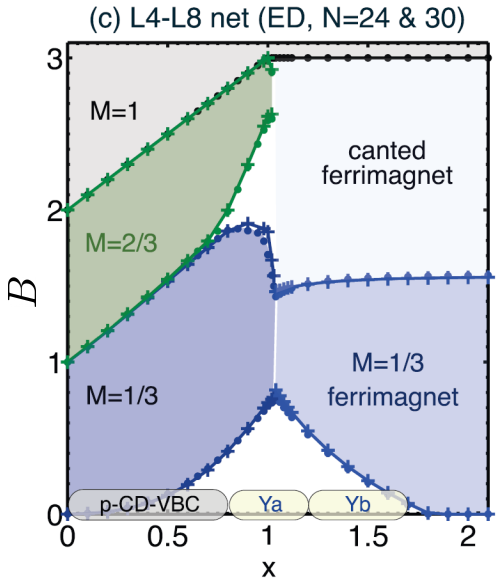

Figure 1.17: Quantum phase diagram of the square-kagome lattice in the presence of magnetic field B computed via exact diagonalization with $N = 24$ or $N = 30$ sites. At zero field, there are at least four ground states: the p-CD-VBC phase, the two disordered Ya and Yb phases and the ferrimagnetic semi-classical order. Several other magnetic states are present at higher field but will not be discussed here. Figure taken from [75].

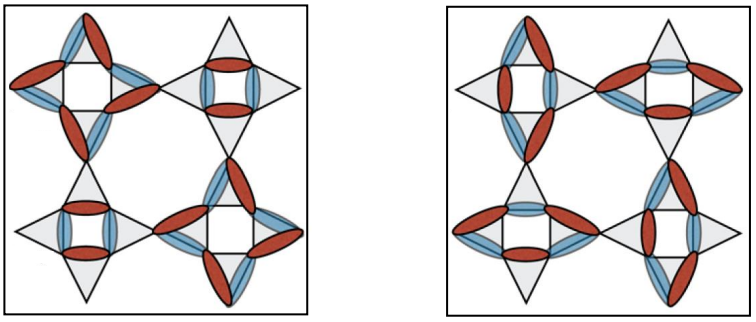

Figure 1.18: Representation of the pinwheel VBC on the square-kagome lattice (left). Blue and red ovals represent resonating singlets. Representation of the loop-six VBC on the square-kagome lattice (right). Figure taken from [68].

figure 1.18 (right). The huge tunneling energy separation between the loop-four (square plaquettes) and loop-six resonant processes in the nearest-neighbor valence bond basis is completely modified when taking into account longer-range virtual singlets which yields tunneling amplitude that do not exponentially decay with the length of the loop. This phenomenon stabilizes the loop-six VBC which would otherwise be much higher in energy than the pinwheel VBC at the minimum truncation level.

In conclusion, despite two VBC candidates and multiple potential ground states from exact diagonalization, the intermediate region of the quantum phase diagram has yet

to be more deeply understood. This will be the subject of the Schwinger boson study carried out in chapter 3.

1.4.2.3 Newly synthesized experimental compound

Last but not least, the recent synthesis of the experimental compound reported in [6] could shed a new light on the nature of the ground state on the square-kagome lattice. The compound $KCu_6AlBiO_4(SO_4)_5Cl$ is composed of two-dimensional layers of Cu^{2+} ions separated by non-magnetic atoms as represented on figure 1.19 (left). The Cu^{2+} layers form two-dimensional square-kagome lattices and the presence of non-magnetic atoms between them leads to an enlarged interlayer spacing which better prevents interlayer magnetic coupling. Moreover, the difference in valence number between the Cu^{2+} ions and the other non-magnetic atoms prevents site mixing. No significant Dzyaloshinskii-Moriya interaction in the compound was reported yet.

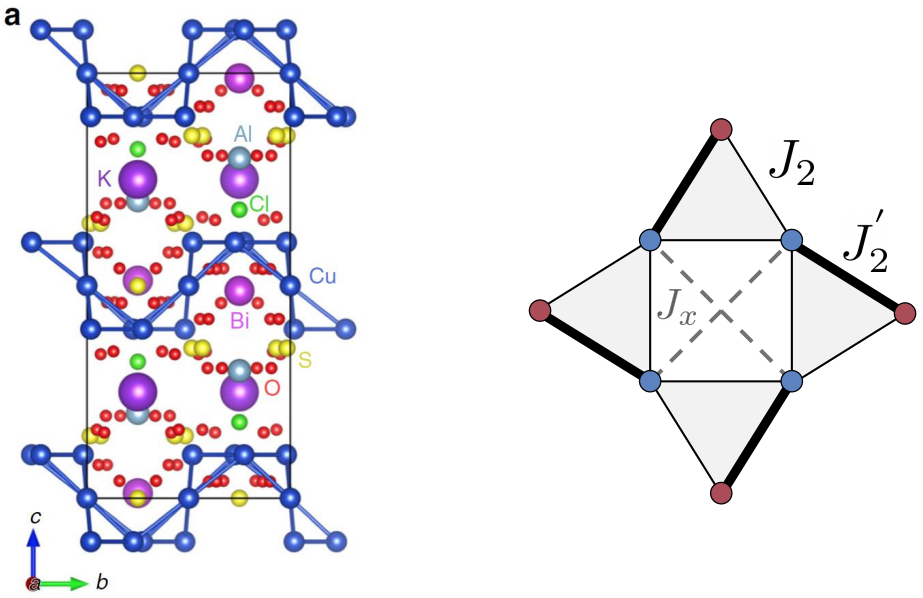

Figure 1.19: Crystal structure of $KCu_6AlBiO_4(SO_4)_5Cl$ composed of two-dimensional layers of Cu^{2+} ions with square-kagome geometry (left). The presence of non-magnetic atoms between the magnetic square-kagome layers enlarges the interlayer spacing. Figure taken from [6]. Representation of the $J_1 - J_2 - J_2'$ Heisenberg model on the square-kagome lattice thought to describe the physics of the experimental compound and studied via exact diagonalization by Morita *et al.* [70] (right). The additiional J_x coupling used in the DMRG study of [6] is represented in dashed gray lines. The J_1 coupling is not represented here.

Antiferromagnetic exchange in the Cu^{2+} layers arise from superexchange interactions occuring through $Cu - O - Cu$ bonds. Three different bond angles yields three different nearest-neighbor antiferromagnetic couplings J_1, J_2 and J_2'. They are represented on the square-kagome lattice on figure 1.19 (right). The J_1 coupling (not represented on the figure) still connects u sites while J_2 and J_2' are connecting u and v sites.

The first experimental measurements on $KCu_6AlBiO_4(SO_4)_5Cl$ reported in [6] contain magnetic and thermodynamic measurements, muon spin relaxation and inelastic neutron scattering experiments. First, magnetization, magnetic susceptibility as well as specific heat measurements did not find any evidence of long-range order or VBC behavior. These results are supported by muon spin relaxation that shows no long-range ordering down to 58 mK, which is roughly three orders of magnitude lower than the strongest magnetic coupling. Muon spin relaxation is also consistent with the formation of a quantum spin-liquid ground state at very low temperature. Finally, inelastic neutron scattering points to the presence of a gapless continuum of spinon excitations. In the end, all these measurements reveal the formation of a disordered gapless spin-liquid at very low temperature near the ground state.

These experimental results were compared to further theoretical work including exact diagonalization, finite temperature Lanczos and DMRG methods [6]. While the magnetic susceptibility and magnetization curves were reproduced for $J_1 = 135$ K, $J_2 = 162$ K and $J_2^{'} = 115$ K, the DMRG dynamical structure factors could not match the inelastic neutron scattering results, even by adding an additional coupling J_x, represented by the dashed gray lines in figure 1.19 (right). This means that the $J_1 - J_2 - J_2^{'}$ Heisenberg model does not contain all the elements describing the magnetic interactions of $KCu_6AlBiO_4(SO_4)_5Cl$ such as potential further-neighbor or Dzyaloshinskii-Moriya interactions. This argument is further confirmed by the exact diagonalization study of Morita *et al.* [70] on the $J_1 - J_2 - J_2^{'}$ model which associates a long-range ordered ground state to the coupling values describing the compound and not a gapless spin liquid.

In conclusion, further theoretical work is needed to understand the model describing the experimental compound. More insight could also be gained by the synthesis of other square-kagome compounds or by the possibility to study the square-kagome geometry in optical lattices [74].

Chapter 2

Theoretical and Numerical Tools

2.1 Schwinger boson formalism

2.1.1 Motivation

We have seen in the previous chapter that determining the quantum ground state of a seemingly simple Heisenberg model on a frustrated lattice turns out to be very challenging, the kagome lattice being one of the most famous example. Both the experimental and theoretical sides present difficulties that hinder a perfect comprehension of such systems. For instance, experimentally, some compounds may exhibit site mixing, additional Dzyaloshinskii–Moriya coupling, lattice distortion or further neighbor interaction [50, 56] as is the case for various kagome compounds such as herbertsmithite, vesignieite and kapellasite [5, 52, 54]. These various shifts from the ideal lattice geometry and from the nearest-neighbor Heisenberg Hamiltonian prevent one from experimentally probe what would correspond to a perfect theoretical model.

Numerically, other kinds of difficulties arise when simulating frustrated spin systems. A forthright method to simulate such systems, called exact diagonalization, consists in diagonalizing the exact Hamiltonian of dimensions $2^N \times 2^N$ where N is the number of spin$-1/2$ in the system. However, this method has a strong limitation caused by the exponential growth of the Hilbert space with the system size. For systems over about 40 sites, taking into account the 2^N states becomes computationally too challenging, even for highly symmetric models. To this day, the largest cluster on the kagome lattice used for exact diagonalization studies was composed of 48 sites [39]. This strong size limitation thus precludes the method to reach the thermodynamic limit and more importantly can prevent the method to capture essential characteristics of the ground state.

To circumvent this problem, it is possible to leave the exact resolution to perfom approximations on the model's Hamiltonian, for instance via a mean-field approach. An example of such methods is the cluster mean-field theory [79] which is based on a decomposition of the Hamiltonian with internal bonds treated exactly through exact diagonalization and external bonds treated via a mean-field decoupling. Such a mean-field approximation enables calculations in the mean-field thermodynamic limit but inevitably loses some information on the ground state by not taking into account all possible correlations. The remaining challenge to thoroughly study such frustrated systems is of course to gather the results from both types of methods, as well as experimental data, in order to gain the most insight on the nature of the model's ground state.

In this chapter, we will focus on the Schwinger boson mean-field theory (SBMFT) [80]. Starting from a parton construction of the spin operator using Schwinger bosons, we will show, by means of a mean-field decoupling, how we can use this method to determine full quantum phase diagrams of frustrated models. A strong advantage of this mean-field approach is that it allows for the study of systems of very large sizes often reaching the thermodynamic limit. On the downside, due to multiple approximations the results we get from the method remain qualitative. These results are nonetheless very useful, first to connect to experimental studies and second because they often present new insight into the physics of the model. For instance by revealing new ground-state candidates that would potentially be overlooked by exact but limited methods.

The Schwinger boson method has been very popular in the study of frustrated magnets, for one, because it is able to treat both ordered and disordered ground states on an equal footing. It has been successful on a variety of frustrated models to analytically study their ground states [81] and establish full phase diagrams [38, 82, 83]. It is also quite versatile as it can be extended to various other models such as the XXZ model [84] or the Heisenberg model with additional Dzyaloshinskii–Moriya coupling [85]. Finally, in the context of the projective symmetry group approach [86–88], it is also possible to classify all SBMFT spin-liquid states on a specific lattice.

We will first present the Schwinger boson formalism as well as the associated mean-field decoupling and its effect on the Heisenberg Hamiltonian. Then, we will explain in details the self-consistent procedure leading to the determination of the quantum ground states as well as the physical quantities we use to characterize them. We will close this chapter by the description of local Wilson loops operators needed to further distinguish mean-field spin-liquid states and their associated quantum orders.

2.1.2 Parton construction

As we have seen in section 1.3, a defining characteristic of spin-liquid states is the presence of fractionalized excitations. For the spin$-1/2$ Heisenberg model on frustrated lattices, these fractionalized excitations correspond to spinons that will change the magnetization of the system by $\pm 1/2$. In other words, the effect of a spinon represents only a fraction of a classical spin flip that changes S^z_{tot} by ± 1 and thus cannot be described by a local action of $\hat{S}^+_i$ or $\hat{S}^-_i$.

Consequently, it seems relevant to introduce spinon creation and annihilation operators in order to describe quantum spin-liquid states. This is the idea behind the parton construction of spin liquids, where we bring into play two types of spinons (up and down) on each site of the lattice. The spin operators are then:

$$\hat{S}^+_i = \hat{b}^\dagger_{i\uparrow}\hat{b}_{i\downarrow} \tag{2.1}$$

$$\hat{S}^-_i = \hat{b}^\dagger_{i\downarrow}\hat{b}_{i\uparrow} \tag{2.2}$$

$$\hat{S}^z_i = \frac{1}{2}(\hat{b}^\dagger_{i\uparrow}\hat{b}_{i\uparrow} - \hat{b}^\dagger_{i\downarrow}\hat{b}_{i\downarrow}) \tag{2.3}$$

In the Schwinger boson formalism we are interested in spinon operators displaying the following bosonic commutation relations:

$$\left[\hat{b}_{i\sigma}, \hat{b}^\dagger_{j\sigma'}\right] = \delta_{i,j}\delta_{\sigma,\sigma'} \tag{2.4}$$

$$\left[\hat{b}_{i\sigma}, \hat{b}_{j\sigma}\right] = \left[\hat{b}^\dagger_{i\sigma}, \hat{b}^\dagger_{j\sigma}\right] = 0 \tag{2.5}$$

Note that a similar decomposition into *fermionic* spinons is as legitimate and leads to the Abrikosov fermion formalism [30]. In any case, the statistics of the previous spinon operators should not influence the actual statistics of the physical excitations of the system [89]. However, Schwinger bosons will mostly be used to describe $\mathbb{Z}_2$ gapped spin liquids and long-ranged magnetic orders since $U(1)$ gapless spin liquids remain challenging to treat because of the condensation of the Schwinger bosons. These $U(1)$ spin liquids are still accessible in the Abrikosov fermion formalism though.

For the remaining chapters, we will only focus on the Schwinger boson formalism and the associated Schwinger boson mean-field theory (SBMFT). Using the bosonic spinon operators, the expression for the spin operator on a site i is:

$$\hat{\mathbf{S}}_i = \frac{1}{2}\sum_{\alpha,\beta}\hat{b}^\dagger_{i\alpha}\boldsymbol{\sigma}_{\alpha,\beta}\hat{b}_{i\beta} \tag{2.6}$$

where $\boldsymbol{\sigma}$ are the Pauli matrices and $\alpha, \beta = \uparrow, \downarrow$.

It is then straightforward to verify that such spin operators follow as expected the commutation relations:

$$\left[\hat{S}^u, \hat{S}^v\right] = i\epsilon_{u,v,w}\hat{S}^w \tag{2.7}$$

2.1.3 Construction of the Hamiltonian

The Heisenberg Hamiltonian is invariant by a global rotation of the spins. We want to find an expression of this Hamiltonian using bond operators of Schwinger bosons that respects this symmetry. Let us introduce the two following SU(2)-invariant [90] bond operators:

$$\hat{A}_{ij} = \frac{1}{2}(\hat{b}_{i\uparrow}\hat{b}_{j\downarrow} - \hat{b}_{i\downarrow}\hat{b}_{j\uparrow}) \quad \text{and} \quad \hat{B}_{ij} = \frac{1}{2}(\hat{b}^\dagger_{i\uparrow}\hat{b}_{j\uparrow} + \hat{b}^\dagger_{i\downarrow}\hat{b}_{j\downarrow}) \tag{2.8}$$

The $\hat{A}^\dagger_{ij}$ operators are associated with the creation of a singlet on the oriented bond $(i \to j)$. The need for oriented bond comes from the relation $\hat{A}_{ij} = -\hat{A}_{ji}$. On the other hand, the $\hat{B}_{ij}$ operator accounts for the possibility for a boson to hop from a site i to a site j. Such a behavior will be favored in an ordered background while the presence of singlets will tend to characterize a disordered phase.

The scalar product in the Heisenberg Hamiltonian can easily be computed using the expression 2.6 of the spin operator, yielding in terms of Schwinger boson bond operators:

$$\hat{\mathbf{S}}_i \cdot \hat{\mathbf{S}}_j =: \hat{B}^\dagger_{ij}\hat{B}_{ij} : -\hat{A}^\dagger_{ij}\hat{A}_{ij} \tag{2.9}$$

where $: \hat{\mathcal{O}}_{ij} :$ stands for the normal ordering of operator $\hat{\mathcal{O}}_{ij}$.

We now have the expression of the SU(2)-invariant Schwinger boson Heisenberg Hamiltonian:

$$\mathcal{H}_{SB} = \sum_l \sum_{\langle i,j\rangle_l} J_l\big(: \hat{B}^\dagger_{ij}\hat{B}_{ij} : -\hat{A}^\dagger_{ij}\hat{A}_{ij}\big) \tag{2.10}$$

where the index l corresponds to the different types of coupling in the studied model.

Having incorporated these new bond operators into the Hamiltonian, we can already see here that the Schwinger boson formalism will allow the study of both disordered phases and long-range magnetic orders on an equal footing.

The scalar product of equation 2.9 can be computed in several ways:

$$\hat{\mathbf{S}}_i \cdot \hat{\mathbf{S}}_j = S^2 - 2\hat{A}^\dagger_{ij}\hat{A}_{ij} \tag{2.11}$$

$$\hat{\mathbf{S}}_i \cdot \hat{\mathbf{S}}_j = 2 : \hat{B}^\dagger_{ij}\hat{B}_{ij} : -S^2 \tag{2.12}$$

Each of them leads to a different expression of the Heisenberg Hamiltonian but should give coherent results. However, we will be performing next a mean-field decoupling

that will discriminate these different models. In the rest of this work, we will focus on the $\hat{A}_{ij} - \hat{B}_{ij}$ formalism, as described in equation 2.10 since it allows one to describe the mixing of spin singlets and spin triplets on each bond of the system which is an essential mechanism in frustrated spin systems [32, 90]. Moreover, a better description of the excitation spectrum of various frustrated systems was found in reference [91] using this particular formalism.

2.1.4 Gauge invariance and boson constraints

The rewriting of the spin operators in terms of Schwinger bosons has two consequences. First, if we introduce the following local gauge transformation of the spinon operators:

$$\hat{b}_{j\sigma} \rightarrow e^{i\theta_j}\hat{b}_{j\sigma} \quad \text{with} \quad \theta_j \in [0, 2\pi[\tag{2.13}$$

we easily see that this transformation leaves the spin operator of equation 2.6 invariant. This result will be of great importance to define gauge invariant quantities that discriminate different spin-liquid states in section 2.5.

Second, by introducing two types of bosons on each site of the lattice, the number of possible quantum states on a single lattice site goes from two states in the case of a regular spin$-1/2$ to four states. This leads to an enlargement of the Hilbert space inherent to the Schwinger boson formalism. To ensure that we are in the Hilbert space of the initial spin system, a constraint on the number of boson per site must be respected:

$$\hat{b}^{\dagger}_{i\uparrow}\hat{b}_{i\uparrow} + \hat{b}^{\dagger}_{i\downarrow}\hat{b}_{i\downarrow} = \hat{n}_{i\uparrow} + \hat{n}_{i\downarrow} = \kappa \tag{2.14}$$

where $\kappa = 2S$.

However, it is very hard numerically speaking to fulfill the constraint 2.14 exactly. This is why it will be verified only on average using Lagrange multipliers μ_i on each site of the system. The constraints on each site are incorporated in the Hamiltonian through an additional term $\sum_i \mu_i(\hat{n}_{i\uparrow} + \hat{n}_{i\downarrow} - \kappa)$, so that each μ_i acts as a chemical potential for the presence of spinons on a site i. In the end, only states with an average boson density per site of κ will be selected which is the first approximation of our Schwinger boson approach. The second approximation, a mean-field decoupling of the bond operators $\hat{A}_{ij}$ and $\hat{B}_{ij}$, will be described in the next section.

2.2 The mean-field approach

We have until now been interested in the following Heisenberg Hamiltonian composed of quartic terms in bosonic operators:

$$\mathcal{H} = \sum_l \sum_{\langle i,j \rangle_l} J_l \big(: \hat{B}_{ij}^\dagger \hat{B}_{ij} : - \hat{A}_{ij}^\dagger \hat{A}_{ij} \big) + \sum_i \mu_i (\hat{n}_{i\uparrow} + \hat{n}_{i\downarrow} - \kappa) \tag{2.15}$$

The idea behind SBMFT is to perform a mean-field decoupling on the bond operators $\hat{A}_{ij}$ and $\hat{B}_{ij}$ to obtain a mean-field Hamiltonian quadratic in bosonic operators that can be diagonalized via a Bogoliubov transformation [92]. After diagonalization, we derive self-consistent equations which are then solved in order to determine the ground states of vavrious frustrated spin systems.

2.2.1 Mean-field decoupling

The mean-field decoupling in SBMFT consists in neglecting the fluctuations of the bond operators $\hat{A}_{ij}$ and $\hat{B}_{ij}$. Let us rewrite these operators as follows:

$$\begin{cases} \hat{A}_{ij} = \langle \hat{A}_{ij} \rangle + (\hat{A}_{ij} - \langle \hat{A}_{ij} \rangle) \equiv \langle \hat{A}_{ij} \rangle + \delta \hat{A}_{ij} \\ \hat{B}_{ij} = \langle \hat{B}_{ij} \rangle + (\hat{B}_{ij} - \langle \hat{B}_{ij} \rangle) \equiv \langle \hat{B}_{ij} \rangle + \delta \hat{B}_{ij} \end{cases} \tag{2.16}$$

The mean-field approximation considers that the $(\delta \hat{A}_{ij})^2$ and $(\delta \hat{B}_{ij})^2$ terms in the Hamiltonian are negligeable. We then get for the $\hat{A}_{ij}^\dagger \hat{A}_{ij}$ and $: \hat{B}_{ij}^\dagger \hat{B}_{ij} :$ terms in the Hamiltonian:

$$\begin{cases} \hat{A}_{ij}^\dagger \hat{A}_{ij} \to A_{ij} \hat{A}_{ij}^\dagger + A_{ij}^* \hat{A}_{ij} - A_{ij}^* A_{ij} \\ \hat{B}_{ij}^\dagger \hat{B}_{ij} \to B_{ij} \hat{B}_{ij}^\dagger + B_{ij}^* \hat{B}_{ij} - B_{ij}^* B_{ij} \end{cases} \tag{2.17}$$

The mean-field parameters A_{ij} and B_{ij} correspond to the following expectation value:

$$\begin{cases} A_{ij} = \langle \Phi_0 | \, \hat{A}_{ij} \, | \Phi_0 \rangle \\ B_{ij} = \langle \Phi_0 | \, \hat{B}_{ij} \, | \Phi_0 \rangle \end{cases} \tag{2.18}$$

where $|\Phi_0\rangle$ is the ground state wavefunction of the system.

The expression of the Heisenberg Hamiltonian thus becomes:

$$\begin{aligned} \mathcal{H}_{MF} = & \sum_l \sum_{\langle i,j \rangle_l} J_l (B_{ij} \hat{B}_{ij}^\dagger + B_{ij}^* \hat{B}_{ij} - A_{ij} \hat{A}_{ij}^\dagger - A_{ij}^* \hat{A}_{ij} + |A_{ij}|^2 - |B_{ij}|^2) \\ & + \sum_i \mu_i (\hat{n}_{i\uparrow} + \hat{n}_{i\downarrow} - \kappa) \end{aligned} \tag{2.19}$$

Along with the constraint 2.14 being respected only on average, the mean-field decoupling of $\hat{A}_{ij}$ and $\hat{B}_{ij}$ operators represent the second approximation of the SBMFT formalism.

Finally, it is worth noticing that in the Schwinger boson formalism, the spin fluctuations $\langle \hat{\mathbf{S}}_i^2 \rangle$ are overshot by a factor 3/2 if we keep $\kappa = 2S$ [80] so that:

$$\langle \hat{\mathbf{S}}_i^2 \rangle = \frac{3}{8}\kappa(\kappa+2) \tag{2.20}$$

An alternate choice in the value of κ would allow one to get back the correct value of the spin fluctuations $\langle \hat{\mathbf{S}}_i^2 \rangle = S(S+1)$ instead of having a correct spin length [88] [93]. This is the choice we have made in all further calculations with $\kappa = \sqrt{3} - 1$ giving the expected $\langle \hat{\mathbf{S}}_i^2 \rangle = S(S+1)$ (see equation 2.20), albeit with a modified spin length of $\kappa/2 \approx 0.37$. It is also possible to treat κ as a continuous parameter in order to enhance or decrease quantum fluctuations in the system [32, 82, 93, 94].

2.2.2 Fourier transform of the Hamiltonian

In the next chapters, we will study frustrated spin systems on finite size lattices with periodic boundary conditions. Let us note n_c the number of unit cell in our system with $n_c = l \times l$ for a linear system size l. We also define n_u as the number of sublattice in a unit cell. Working on such periodic lattices, it is useful to define the (inverse) Fourier transform of the spinon operators:

$$\hat{b}_{i\sigma} = \frac{1}{\sqrt{n_c}} \sum_{\mathbf{k}} e^{i\mathbf{k}\cdot\mathbf{r}_i} \hat{b}^{\alpha}_{\mathbf{k}\sigma} \tag{2.21}$$

where the site i is located at the position $\mathbf{r}_i$ and belongs to a sublattice α, the summation is over the first Brillouin zone.

The first step to diagonalize the mean-field Hamiltonian is to express it in Fourier space using equation 2.21. Doing so, we obtain a generic form of the SBMFT Hamiltonian which is displayed in appendix A.1. Though a simpler way to express this Hamiltonian consists in using the following spinor:

$$\Psi_{\mathbf{k}} = (\hat{b}^1_{\mathbf{k}\uparrow}, \dots, \hat{b}^{n_u}_{\mathbf{k}\uparrow}, \hat{b}^{1\dagger}_{-\mathbf{k}\downarrow}, \dots, \hat{b}^{n_u\dagger}_{-\mathbf{k}\downarrow})^T \tag{2.22}$$

The SBMFT Hamiltonian then becomes:

$$\mathcal{H} = \sum_{\mathbf{k}} \Psi^{\dagger}_{\mathbf{k}} M_{\mathbf{k}} \Psi_{\mathbf{k}} + \Lambda_0 \tag{2.23}$$

where $M_{\mathbf{k}}$ is a $(2n_u \times 2n_u)$ matrix containing all the quadratic terms listed in appendix A.1.

If more quadratic terms in boson operators were present in the computation of the Hamiltonian, an enlarged spinor would be needed to conserve the structure of equation 2.23, as is for instance the case in some mean-field decoupling in the Abrikosov fermion formalism. Such a spinor of size $4n_u$ would take the form:

$$\Psi'_{\mathbf{k}} = (\hat{b}^1_{\mathbf{k}\uparrow}, \dots, \hat{b}^{n_u}_{\mathbf{k}\uparrow}, \hat{b}^1_{-\mathbf{k}\uparrow}, \dots, \hat{b}^{n_u}_{-\mathbf{k}\uparrow}, \hat{b}^{1\dagger}_{\mathbf{k}\downarrow}, \dots, \hat{b}^{n_u\dagger}_{\mathbf{k}\downarrow}, \hat{b}^{1\dagger}_{-\mathbf{k}\downarrow}, \dots, \hat{b}^{n_u\dagger}_{-\mathbf{k}\downarrow})^T \tag{2.24}$$

The last term in equation 2.23 is a constant with:

$$\Lambda_0 = \sum_l \sum_{\langle i,j\rangle_l} J_l(|A_{ij}|^2 - |B_{ij}|^2) - \sum_\alpha \mu_\alpha(\kappa + 1)n_c \tag{2.25}$$

where the sum indexed by α runs over all the n_u sublattices of the lattice.

For the remaining of this work, we will assume that the phases we want to study can be described on a unit cell of reference composed of n_u sublattices that will be repeated n_c times in real space. The size of this unit cell of reference has to be chosen carefully depending on the studied system. It has to be large enough to account for all potential symmetry breakings of the ground states while not being so large that the determination of the ground states becomes too computationally expensive. In the two SBMFT studies of chapters 3 and 4, once the choice of a minimal unit cell of reference is done, we always control that the use of larger unit cells yields the same ground states and does not change the physics of the system.

2.2.3 Diagonalization of the Hamiltonian

After this mean-field decoupling, the final step before gaining access to the energy of the system is the block-diagonalization of the Hamiltonian in Fourier space. To do so, we perform a Bogoliubov transformation which is a generic transformation allowing the diagonalization of Hamiltonians that are quadratic in creation and anihilation operators [92]. Let us start by introducing a new type of operator, called Bogoliubov boson operators, and the associated spinor:

$$\Gamma_{\mathbf{k}} = (\hat{\gamma}^1_{\mathbf{k}\uparrow}, \dots, \hat{\gamma}^{n_u}_{\mathbf{k}\uparrow}, \hat{\gamma}^{1\dagger}_{-\mathbf{k}\downarrow}, \dots, \hat{\gamma}^{n_u\dagger}_{-\mathbf{k}\downarrow})^T \tag{2.26}$$

These new operators correspond to a new basis in which we want the mean-field Hamiltonian to be diagonal, that is to say:

$$\mathcal{H}_{MF} = \sum_{\mathbf{k}} \Gamma^{\dagger}_{\mathbf{k}} \omega_{\mathbf{k}} \Gamma_{\mathbf{k}} + \Lambda_0 \tag{2.27}$$

where the matrix $\omega_{\mathbf{k}}$ is diagonal of size $2n_u \times 2n_u$, with:

$$\omega_{\mathbf{k}} = \begin{pmatrix} \varepsilon^1_{\mathbf{k}\uparrow} & & & & & & \\ & \ddots & & & & & \\ & & \varepsilon^{n_u}_{\mathbf{k}\uparrow} & & & & \\ & & & \ddots & & & \\ & & & & \varepsilon^1_{-\mathbf{k}\downarrow} & & \\ & & & & & \ddots & \\ & & & & & & \varepsilon^{n_u}_{-\mathbf{k}\downarrow} \end{pmatrix} \tag{2.28}$$

The matrix $\omega_{\mathbf{k}}$ contains the $2n_u$ eigenvalues of the Hamiltonian, which verify $\varepsilon^{\alpha}_{\mathbf{k}\uparrow} = \varepsilon^{\alpha}_{-\mathbf{k}\downarrow}$, in the case of non-chiral magnetic phases [95]. Were time-reversal symmetry to be broken for a particular ground state, we would then see a difference between the eigenvalues $\varepsilon^{\alpha}_{\mathbf{k}\uparrow}$ and $\varepsilon^{\alpha}_{-\mathbf{k}\downarrow}$ [95], as is the case for the chiral states of chapter 4.

Performing the Bogoliubov transformation to obtain a diagonalized Hamiltonian requires to determine the transformation matrix $T_{\mathbf{k}}$ connecting both types of bosonic operators:

$$\Psi_{\mathbf{k}} = T_{\mathbf{k}} \Gamma_{\mathbf{k}} \tag{2.29}$$

The first relation characterizing the transformation matrix is:

$$T^{\dagger}_{\mathbf{k}} M_{\mathbf{k}} T_{\mathbf{k}} = \omega_{\mathbf{k}} \tag{2.30}$$

It ensures that the mean-field Hamiltonian is indeed diagonal in the new basis. However, because of the bosonic nature of the operators, a regular diagonalization of the Hamiltonian is not enough. The bosonic commutation relations of the Bogoliubov operators are to be preserved which yields another condition on the nature of the transformation matrix $T_{\mathbf{k}}$:

$$T^{\dagger}_{\mathbf{k}} g_{n_u} T_{\mathbf{k}} = g_{n_u} \tag{2.31}$$

Here, g_{n_u} is the so called "para-unit matrix" [96], expressed as:

$$g_{n_u} = \begin{pmatrix} \mathcal{I}_{n_u} & \\ & -\mathcal{I}_{n_u} \end{pmatrix} \tag{2.32}$$

with $\mathcal{I}_{n_u}$ the identity matrix of size n_u.

After the Bogoliubov transformation, we end up with an Hamiltonian from which it is straightforward to extract the free energy of the system at zero temperature. This energy is computed in the vacuum of the Bogoliubov bosons and corresponds to:

$$\mathcal{F} = \sum_{\mathbf{k},\alpha} \varepsilon^{\alpha}_{\mathbf{k}\uparrow} + \Lambda_0 \tag{2.33}$$

Another simple method to gain access to this free energy is to compute the eigenvalues of the matrix $g_{n_u} M_{\mathbf{k}}$. Indeed if we combine the two relations 2.30 and 2.31, we obtain:

$$T_{\mathbf{k}}^{-1} g_{n_u} M_{\mathbf{k}} T_{\mathbf{k}} = g_{n_u} \omega_{\mathbf{k}} \tag{2.34}$$

This means that diagonalizing the matrix $g_{n_u} M_{\mathbf{k}}$ yields an energy spectrum composed of the eigenvalues $\varepsilon^{\alpha}_{\mathbf{k}\uparrow}$ and the eigenvalues $-\varepsilon^{\alpha}_{-\mathbf{k}\downarrow}$.

The computation of the free energy is one way to perform the self-consistent procedure at the heart of SBMFT. However, it is not the only one and we have actually chosen to focus on a method requiring the computation of the transformation matrix $T_{\mathbf{k}}$ in order to evaluate the mean-field parameters in the Bogoliubov boson vacuum. This self-consistent procedure is described in detail in the next section.

2.3 Self-consistent resolution

2.3.1 Description of the procedure

The expression of the Hamiltonian in the Schwinger boson formalism after a mean-field decoupling has been described above. The energy of the ground state is easily computed once a Bogoliubov transformation is performed to block-diagonalize the Hamiltonian in Fourier space. We now have all the ingredients to perform the SBMFT self-consistent procedure.

Let us take the example of the square-kagome lattice, described in section 1.4, to describe the SBMFT algorithm on a concrete system. Figure 2.1 (left) depicts such a system, composed of $n_c = l \times l$ unit cells. As said, we make the assumption that the phases we study are translationally invariant, that is they are described by a set of mean-field parameters $\{A_{ij}, B_{ij}, \mu_{\alpha}\}$ associated with a unit cell of reference. Such a set of mean-field parameters is called an *Ansatz*.

For this particular example we choose a unit cell of $n_u = 6$ sublattice, represented in figure 2.1 (right), where an *Ansatz* is composed of 30 mean-field parameters, *i.e.* A_{ij} and B_{ij} parameters for the 12 bonds of the unit cell as well as 6 Lagrange multipliers

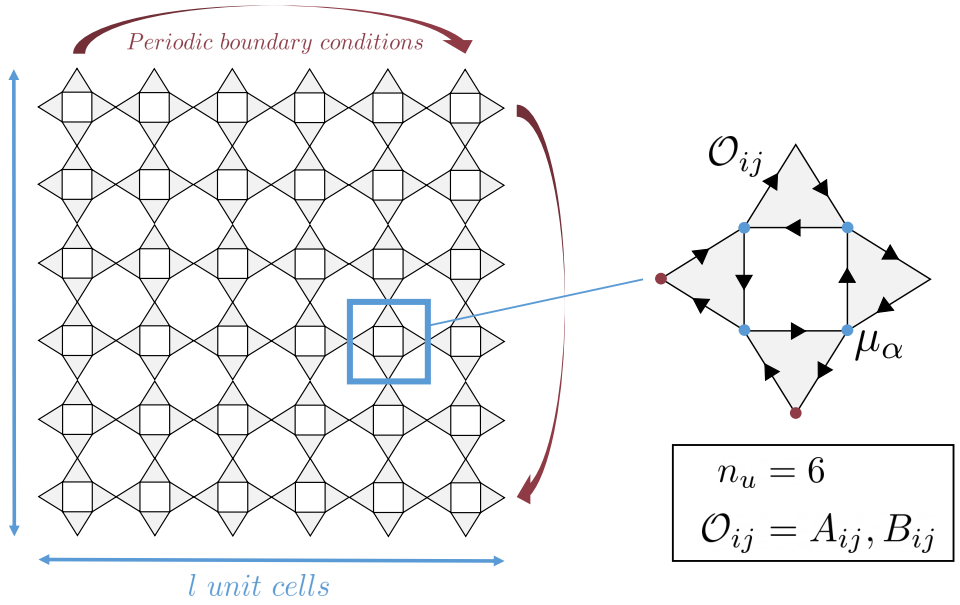

Figure 2.1: Concrete example of a square-kagome system of $n_c = l \times l$ unit cells with periodic boundary conditions (left). In this particular example each unit cell is composed of $n_u = 6$ sublattices. Representation of the $n_u = 6$ square-kagome unit cell with its 12 oriented bonds (right). An *Ansatz* describing this unit cell is composed of 30 mean-field parameters, 12 parameters A_{ij}, 12 parameters B_{ij} as well as 6 Lagrange multipliers μ_α.

μ_α. In the SBMFT study on the square-kagome lattice of chapter 3, we have controlled that using bigger unit cells of reference up to $n_u = 24$ does not change the physics of the system, nor its phase diagram.

Starting from an initial *Ansatz*, the first step of the procedure consists in finding the set $\{\mu_\alpha\}$ of Lagrange multipliers that fulfills the constraint on the number of bosons. This step will be detailed later. The mean-field Hamiltonian is then computed and diagonalized. Next, new values for the A_{ij} and B_{ij} parameters are computed via two possible methods. The first one consists in minimizing the free energy of the system whereas the second one evaluates the mean-field parameters in the Bogoliubov boson vacuum. Both methods are presented next. These steps are repeated until convergence is reached and we have used an arbitrary tolerance of at least 10^{-9} on the mean-field parameters. We also monitor the convergence of the ground state energy with a 10^{-12} tolerance.

2.3.2 The free energy method

The first way to obtain self-consistent equations on the mean-field parameters is to use the free energy of equation 2.33. The idea is to find a fixed point in the parameter space of all A_{ij}, B_{ij} and μ_α. To do so, the free energy must be extremized with respect to the

potentially complex mean-field parameters. This gives a set of self-consistent equations:

$$\frac{\partial \mathcal{F}}{\partial A_{ij}} = 0, \quad \frac{\partial \mathcal{F}}{\partial A^*_{ij}} = 0, \quad \frac{\partial \mathcal{F}}{\partial B_{ij}} = 0, \quad \frac{\partial \mathcal{F}}{\partial B^*_{ij}} = 0 \quad \text{and} \quad \frac{\partial \mathcal{F}}{\partial \mu_\alpha} = 0 \tag{2.35}$$

that are solved numerically yielding a new set of mean-field parameters.

The other way to obtain self-consistent equations on the mean-field parameters corresponds to the one we have used in our algorithm. It bypasses the need for numerical derivatives and instead relies on the coefficients of the transformation matrix $T_{\mathbf{k}}$ computed via a Cholesky decomposition. This requires the computation at each step of a new set of mean-field parameters, that can be compared to the old set until convergence is reached.

2.3.3 The Cholesky decomposition method

The second method uses the transformation matrix $T_{\mathbf{k}}$ to compute the expectation values of the bilinears of bosonic operators $\{b^\alpha_{\mathbf{k}\sigma}\}$ in the ground state $|\Phi_0\rangle$. Here, the ket $|\Phi_0\rangle$ corresponds to the ground state of the Bogoliubov bosonic operators. For future calculations, it is useful to consider the following block form of the transformation matrix $T_{\mathbf{k}}$:

$$T_{\mathbf{k}} = \begin{pmatrix} U_{\mathbf{k}} & X_{\mathbf{k}} \\ V_{\mathbf{k}} & Y_{\mathbf{k}} \end{pmatrix} \tag{2.36}$$

where each of the blocks corresponds to a $(n_u \times n_u)$ matrix.

The expression for the new values of the A_{ij} and B_{ij} parameters are derived in detail in appendix A.2 and are given by:

$$A_{ij} = \frac{1}{2n_c} \sum_{\mathbf{k}} \left(\phi^*_{ij} \sum_d U_{\alpha,d,\mathbf{k}} V^*_{\beta,d,\mathbf{k}} + \phi_{ij} \sum_d Y^*_{\alpha,d,\mathbf{k}} X_{\beta,d,\mathbf{k}} \right) \tag{2.37}$$

$$B_{ij} = \frac{1}{2n_c} \sum_{\mathbf{k}} \left(\phi_{ij} \sum_d X^*_{\alpha,d,\mathbf{k}} X_{\beta,d,\mathbf{k}} + \phi^*_{ij} \sum_d V_{\alpha,d,\mathbf{k}} V^*_{\beta,d,\mathbf{k}} \right) \tag{2.38}$$

where we have used $\phi_{ij} = e^{i\mathbf{k}\cdot\boldsymbol{\delta}_{ij}}$ and $\boldsymbol{\delta}_{ij}$ being the difference of position between sites i and j. The index α (resp. β) corresponds to the sublattice of the site i (resp. j).

We now see that the computation of the new set of mean-field parameters requires to know the coefficients of the transformation matrix $T_{\mathbf{k}}$. To obtain this matrix, we follow a method first described by Colpa in reference [96], where a Cholesky decomposition of the mean-field Hamiltonian is needed.

The Cholesky decomposition states that for an hermitian matrix, such as $M_{\mathbf{k}}$ in equation 2.23, one can find a complex triangular matrix $K_{\mathbf{k}}$ such that $M_{\mathbf{k}} = K^\dagger_{\mathbf{k}} K_{\mathbf{k}}$. Once this

decomposition is done, the next step to find the transformation matrix $T_{\mathbf{k}}$ is to solve the eigenvalue problem for the matrix $K_{\mathbf{k}} g_{n_u} K_{\mathbf{k}}^{\dagger}$. The associated diagonalized matrix is called $L_{\mathbf{k}}$ so that we have:

$$L_{\mathbf{k}} = U_{\mathbf{k}}^{\dagger} K_{\mathbf{k}} g_{n_u} K_{\mathbf{k}}^{\dagger} U_{\mathbf{k}} \tag{2.39}$$

The important thing here is to arrange the eigenvectors of $K_{\mathbf{k}} g_{n_u} K_{\mathbf{k}}^{\dagger}$ in the matrix $U_{\mathbf{k}}$ in such a way that the first n_u diagonal elements of $L_{\mathbf{k}}$ are positive and the last n_u are negative. Doing so, we obtain the diagonal matrix $E_{\mathbf{k}} = g_{n_u} L_{\mathbf{k}}$ with its first n_u diagonal elements being the SBMFT energies $\varepsilon_{\mathbf{k}\uparrow}^{\alpha}$. The last n_u elements are the same up to an additional minus sign.

We now have all the ingredients to compute the Bogoliubov transformation matrix using the relation:

$$T_{\mathbf{k}} = K_{\mathbf{k}}^{-1} U_{\mathbf{k}} E_{\mathbf{k}}^{1/2} \tag{2.40}$$

One problem still has to be adressed for this method to work. Unfortunately, the Cholesky decomposition is possible if and only if the matrix $M_{\mathbf{k}}$ is positive definite for all wave-vector $\mathbf{k}$. In other words, if the eigenvalues of $M_{\mathbf{k}}$ for a particular wave-vector are not all stricly positive, then the previous decomposition is not realisable. Numerically, we check for such an issue at each step of the self-consistent procedure. If one or more of the $M_{\mathbf{k}}$ matrices would not be positive definite, it is possible to add a small $\epsilon > 0$ on the diagonal to allow the Choleksy decomposition problem to be solvable [97]. Once the convergence is reached, it is of course necessary to verify that the final Hamiltonian is positive definite for all $\mathbf{k}$, as it should.

Compared to the free energy method, the Cholesky decomposition naturally takes into account the potential complex nature of the mean-field parameters. It is easy to check that equations 2.37 and 2.38 are also valid for complex values of A_{ij} and B_{ij}. This feature is particularly relevant for the study of the chiral states, later presented in chapter 4.

2.3.4 Lagrange multiplier optimization

Unlike the free energy method, the Cholesky decomposition does not give optimized values for the Lagrange multipliers on its own. That is why, for each step of the self-consistent algorithm, we first need to ensure that the boson constraints are fulfilled by tuning the values of $\{\mu_\alpha\}$.

Basically, we want to set the values of the Lagrange multipliers $\{\mu_\alpha\}$ so that the following relation is respected for each of the n_c unit cell of the system:

$$\sum_{\alpha=1}^{n_u} \mu_\alpha (\hat{n}_{\alpha\uparrow} + \hat{n}_{\alpha\downarrow} - \kappa) = 0 \tag{2.41}$$

More precisely, we want this relation to be verified only on average which allows one to express it as a function of the coefficients of the transformation matrix $T_{\mathbf{k}}$:

$$\sum_{\mathbf{k}}\sum_{\alpha}\mu_{\alpha}\Big(\sum_{d}X^{*}_{\alpha,d,\mathbf{k}}X_{\alpha,d,\mathbf{k}}+\sum_{d}V_{\alpha,d,\mathbf{k}}V^{*}_{\alpha,d,\mathbf{k}}\Big)-\sum_{\alpha}\mu_{\alpha}(\kappa+1)n_{c}=0 \tag{2.42}$$

In order to fulfill equation 2.42, we use a simple least squares algorithm finding the optimal n_u Lagrange multipliers that fulfill the bosonic constraint on average. However, we have to restrict the possible values of these Lagrange multipliers during this least squares routine. Indeed, some of these values might lead to a non positive-definite Hamiltonian which would be problematic for the Cholesky decomposition that follows. To overcome this issue, we first compute a threshold μ_{min} above which the values of the Lagrange multipliers yield a positive definite mean-field Hamiltonian. We then perform the least squares routine in the range $[\mu_{min}, +\infty[$. If the least squares routine were to find a set $\{\mu_\alpha\}$ with some of the Lagrange multipliers verifying $\mu_\alpha < \mu_{min}$, the Cholesky decomposition could not be performed and the self-consistent procedure could not go on.

The determination of μ_{min} consists in a simple dichotomy with the constraint of having strictly positive eigenvalues of $M_{\mathbf{k}}$ for all wave-vector $\mathbf{k}$. For this dichotomy, we first make the broad assumption that a single Lagrange multiplier value μ_{min} sets the threshold for the Hamiltonian to be positive definite or not. In reality, the value of μ_{min} can vary between the different sublattices in a unit cell, but it is very hard to determine all $\mu_{min,\alpha}$ independently. However, determing one μ_{min} for all sublattices, proceeding with the least squares method in the range $[\mu_{min}, +\infty[$ and adding a small $\epsilon > 0$ during the Cholesky routine if needed is usually enough to go through with the self-consistent procedure.

2.3.5 Resolution

Let us summarize how the ground state of a frustrated model is determined in the SBMFT framework. Starting from an initial *Ansatz*, modelled from a physical intuition, a classical configuration or chosen at random, we perform the self-consistent procedure described above and schematized in figure 2.2. The value of μ_{min} is determined through a dichotomy to ensure that the mean-field Hamiltonian is positive definite for all wave-vectors $\mathbf{k}$ if $\mu_\alpha > \mu_{min}$. Then, using a least squares optimization scheme, we find the values of all Lagrange multipliers $\mu_\alpha > \mu_{min}$ that fullfill the boson constraint on average. The next step is the Cholesky decomposition of the Hamiltonian to compute the new values of the mean-field parameters thanks to the coefficients of the transformation matrix $T_{\mathbf{k}}$. Finally, we monitor the convergence of the mean-field parameters (as well

as the ground state energy) and start over if an arbitrary low tolerance is not reached.

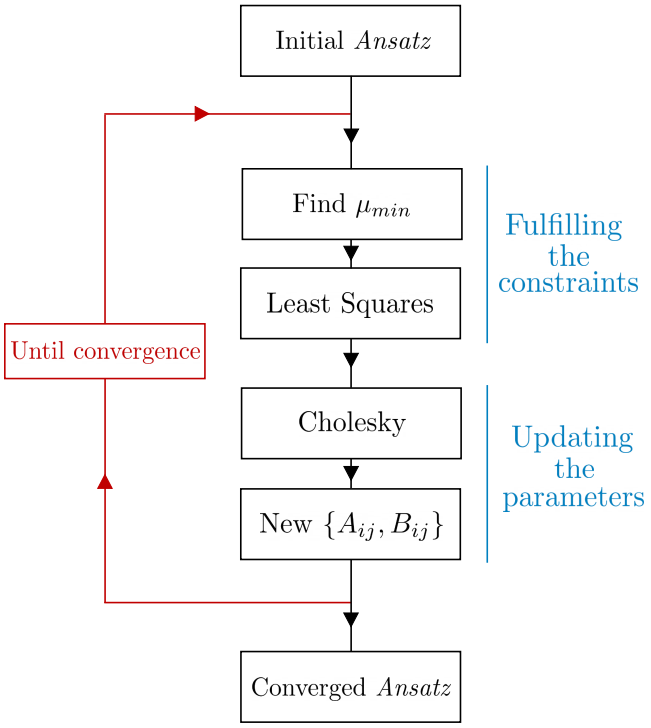

Figure 2.2: Schematic representation of the SBMFT self-consistent algorithm. Starting from an initial *Ansatz* the Lagrange multipliers are optimized to fulfill the constraints. Then, by means of a Cholesky decomposition, a new set of mean-field parameters is computed in the Bogoliubov boson vacuum. This new set is compared with the old one and the procedure ends if convergence is reached.

Once convergence is reached we have found a phase described by a well-defined *Ansatz* that is candidate to be the ground state of the system. This numerical resolution allows the system to choose its actual ground state in a completely unrestricted way, without, in principle, any preexisting *Ansätze*. In practice, the initial conditions for the mean-field parameters have to be chosen with caution in order to help the algorithm converge to an acceptable physical solution.

By performing this procedure many times with various initial conditions we maximize our chances to rule out any local minimum of the energy and to find the true ground state in the SBMFT formalism. Repeating this process for various values of the couplings describing some kind of Heisenberg model leads to a full SBMFT phase diagram.

Now that we know how to determine ground states, we want to be able to describe their characteristics in details. This is the subject of the next section where several physical quantities relevant to the description of various quantum ground states will be calculated in the SBMFT formalism.

2.4 Computing valuable physical quantities

2.4.1 Dispersion relation and energy gap

The first physical quantity essential to describe the quantum ground state obtained after the SBMFT self-consistent procedure is the spinon gap associated to the spinon dispersion relation. Going back to equation 2.33, we see that the dispersion relation is composed of n_u bands. The spinon gap Δ is then computed as the global minimum of the lowest energy band:

$$\Delta = \min_{\mathbf{k},\alpha} \varepsilon^{\alpha}_{\mathbf{k}\uparrow} \tag{2.43}$$

The energy gap Δ is an important characteristic of the ground state. In the case of a gapless phase, associated with a condensation of the Schwinger boson, the ground state is thus a long-range magnetic order with a well-defined ordering wave-vector $\mathbf{Q}$. If the ground state presents a finite gap, then it is disordered and further investigation will be needed to determine its exact nature.

However, working on finite systems, a small but finite gap scaling with n_c will always be present. To overcome this issue, we perform finite size studies to monitor the behavior of Δ as a function of the system size. Our SBMFT procedure being able to reach very large system sizes due to its mean-field approximation, typically tens of thousands of sites, we can most of the time obtain the value of the energy gap in the thermodynamic limit through finite size studies. If the gap goes to zero in the thermodynamic limit, the ground state is then long-range ordered.

2.4.2 Real space spin correlations

Another useful observable determining if the ground state presents long-range order are the spin correlations in real space. Starting from a spin of reference, we compute all values of $\langle \hat{\mathbf{S}}_{\text{ref}} \cdot \hat{\mathbf{S}}_j \rangle$ for all sites i of the system. For a disordered state, these correlations are expected to decay with the distance from the site of reference while they should remain constant for a long-range magnetic order.

In the Schwinger boson formalism, we have access to such correlations through the following relation:

$$\langle \hat{\mathbf{S}}_{\text{ref}} \cdot \hat{\mathbf{S}}_j \rangle = |B_{\text{ref},j}|^2 - |A_{\text{ref},j}|^2 \tag{2.44}$$

However, for a mean-field *Ansatz*, we only have access to the values of the A_{ij} and B_{ij} parameters on the unit cell of reference. That is why we need to compute the values of $A_{\text{ref},j}(\mathbf{R})$ and $B_{\text{ref},j}(\mathbf{R})$ for an arbitrary distance $\mathbf{R}$ between the site of reference and the

site j. The derivation is very similar to the one presented in appendix A.2 and yields:

$$A_{\mathrm{ref},j}(\mathbf{R}) = \frac{1}{2n_c}\sum_{\mathbf{k}}\left(\phi^*(\mathbf{R})\sum_d U_{\alpha,d,\mathbf{k}}V^*_{\beta,d,\mathbf{k}} + \phi(\mathbf{R})\sum_d Y^*_{\alpha,d,\mathbf{k}}X_{\beta,d,\mathbf{k}}\right) \quad (2.45)$$

$$B_{\mathrm{ref},j}(\mathbf{R}) = \frac{1}{2n_c}\sum_{\mathbf{k}}\left(\phi(\mathbf{R})\sum_d X^*_{\alpha,d,\mathbf{k}}X_{\beta,d,\mathbf{k}} + \phi^*(\mathbf{R})\sum_d V_{\alpha,d,\mathbf{k}}V^*_{\beta,d,\mathbf{k}}\right) \quad (2.46)$$

where $\phi(\mathbf{R}) = e^{-i\mathbf{k}\cdot(\boldsymbol{\delta}_\alpha - \mathbf{R} - \boldsymbol{\delta}_\beta)}$ with δ_α (resp. δ_β) the position of the sublattice of the site of reference (resp. the site j) inside its unit cell.

Using equations 2.45 and 2.46, we then have access to the spin correlations in real space for any distance $\mathbf{R}$ and any sublattices α and β.

2.4.3 Static structure factor

The static structure factor is another way to discriminate between an ordered and a disordered phase. Typically, by the presence of a Bragg peak at an ordering wave-vector $\mathbf{Q}$ for long-range magnetic orders. The static structure factor corresponds to the Fourier transform of the spin correlations in real-space, and its expression for two sublattices α and β is given below:

$$S^{\alpha\beta}(\mathbf{k}) = \frac{1}{n_c}\sum_{i,j} e^{i\mathbf{k}\cdot(\mathbf{R_i}-\mathbf{R_j})}\langle \hat{\mathbf{S}}^\alpha_i \cdot \hat{\mathbf{S}}^\beta_j\rangle \quad (2.47)$$

where $\mathbf{R_i}$ and $\mathbf{R_j}$ are the position of sites i and j.

At the end of the self-consistent procedure, the static structure factor is computed via the coefficients of the transformation matrix $T_\mathbf{k}$. A detailed derivation is given in Appendix A.3 which yields the following expression:

$$\begin{aligned} S^{\alpha\beta}(\mathbf{k}) = \frac{1}{4n_c}\sum_{\mathbf{q}}\sum_{d,d'}[\ & 2X^*_{\alpha,d,\mathbf{q}}Y^*_{\alpha,d',\mathbf{k}-\mathbf{q}}(Y_{\beta,d',\mathbf{k}-\mathbf{q}}X_{\beta,d,\mathbf{q}} + Y_{\beta,d,\mathbf{q}}X_{\beta,d',\mathbf{k}-\mathbf{q}}) \\ & + 2V_{\alpha,d,-\mathbf{q}}U_{\alpha,d',\mathbf{q}-\mathbf{k}}(U^*_{\beta,d',\mathbf{q}-\mathbf{k}}V^*_{\beta,d,-\mathbf{q}} + U^*_{\beta,d,-\mathbf{q}}V^*_{\beta,d',\mathbf{q}-\mathbf{k}}) \\ & + X^*_{\alpha,d,\mathbf{q}}U_{\alpha,d',\mathbf{q}-\mathbf{k}}(U^*_{\beta,d',\mathbf{q}-\mathbf{k}}X_{\beta,d,\mathbf{q}} - Y_{\beta,d,\mathbf{q}}V^*_{\beta,d',\mathbf{q}-\mathbf{k}}) \\ & + V_{\alpha,d,-\mathbf{q}}Y^*_{\alpha,d',\mathbf{k}-\mathbf{q}}(-U^*_{\beta,d,-\mathbf{q}}X_{\beta,d',\mathbf{k}-\mathbf{q}} + Y_{\beta,d',\mathbf{k}-\mathbf{q}}V^*_{\beta,d,-\mathbf{q}})\ ] \end{aligned} \quad (2.48)$$

The static structure factor can also make connections between our theoretical work and potential neutron scattering experiments. This is also the case for the next physical feature, the dynamical structure factor.

2.4.4 Dynamical structure factor

The dynamical structure factor provides us with information on the excitation spectrum of each ground states. Moreover, it enables us to compute numerically the experimental signatures of the ground states so that they can be compared with inelastic neutron scattering experiments. The expression of the dynamical structure factor is the following:

$$S^{\alpha\beta}(\mathbf{k},\omega) = \frac{1}{n_c}\sum_{i,j} e^{i\mathbf{k}\cdot(\mathbf{R}_i-\mathbf{R}_j)} \int_{-\infty}^{+\infty} e^{-i\omega t}\langle \hat{\mathbf{S}}_i^{\alpha}(t)\cdot\hat{\mathbf{S}}_j^{\beta}(0)\rangle dt \tag{2.49}$$

Similarly than for the static structure factor, it is possible to express $S^{\alpha\beta}(\mathbf{k},\omega)$ as a function of the coefficients of the matrix $T_{\mathbf{k}}$ and compute it that way at the end of the self-consistent procedure [95].

All these physical quantities allow one to characterize in detail our SBMFT ground states when a symmetry breaking is at work. Last but not least, we introduce a quantity that is relevant to characterize the disordered ground states and their hidden quantum orders.

2.5 Local Wilson loops

2.5.1 Definition and gauge invariance

We will define in this section the gauge fluxes associated to local Wilson loop operators that will further characterize and differentiate disordered ground states. Let us begin by applying the gauge transformation of equation 2.13 on the bond operators $\hat{A}_{ij}$ and $\hat{B}_{ij}$:

$$\hat{A}_{ij} \rightarrow e^{i(\phi_i+\phi_j)}\hat{A}_{ij} \tag{2.50}$$

$$\hat{B}_{ij} \rightarrow e^{i(\phi_j-\phi_i)}\hat{B}_{ij} \tag{2.51}$$

Keeping these relations in mind, it is now possible to construct loop operators composed of a combination of $\hat{A}_{ij}$ and $\hat{B}_{ij}$ operators that will be invariant under this gauge transformation. For instance, by taking a three site triangular loop with sites i, j and k, the following operator is indeed gauge invariant:

$$\hat{B}_{ij}\hat{B}_{jk}\hat{B}_{ki} \rightarrow e^{i(\phi_j-\phi_i+\phi_k-\phi_j+\phi_i-\phi_k)}\hat{B}_{ij}\hat{B}_{jk}\hat{B}_{ki} = \hat{B}_{ij}\hat{B}_{jk}\hat{B}_{ki} \tag{2.52}$$

Such a string of operators is called a Wilson loop operator. Spin-liquid states in the Schwinger boson formalism can be differentiated through the values of gauge fluxes associated with such local Wilson loops. These fluxes are obtained from the Wilson

loop operators by the relation:

$$\Phi_B = \arg(\langle \hat{B}_{ij}\hat{B}_{jk}\hat{B}_{ki}\rangle) \tag{2.53}$$

where the expectation values are computed in the ground state $|\Phi_0\rangle$.

In this mean-field approach, the expectation value of the product of $\hat{B}_{ij}$ operators corresponds to the the product of the associated B_{ij} parameters:

$$\langle \hat{B}_{ij}\hat{B}_{jk}\hat{B}_{ki}\rangle = B_{ij}B_{jk}B_{ki} \tag{2.54}$$

The gauge flux Φ_B is not limited to three site loops but can be computed on loops of arbitrary finite lengths and even on the entire system size. Interestingly, the Wilson loop operator of equation 2.52 is not the only gauge invariant operator that can be constructed with $\hat{A}_{ij}$ and $\hat{B}_{ij}$ operators. For instance, we can also define a gauge flux Φ_A computed from a Wilson loop only composed of $\hat{A}_{ij}$ operators:

$$\Phi_A = \arg\big(\hat{A}_{ij}(-\hat{A}^*_{jk})\dots\hat{A}_{yz}(-\hat{A}^*_{zi})\big) \tag{2.55}$$

Note that it is also possible to construct Wilson loop operators with both $\hat{A}_{ij}$ and $\hat{B}_{ij}$, as long as the expression remains gauge invariant by the transformation 2.13.

2.5.2 An example on the triangular lattice

Let us briefly apply the above considerations on the Wilson loop operators on a concrete system: the Heisenberg antiferromagnet on the triangular lattice. Before doing so, we will give a brief overview of the projective symmetry group method, to better understand how to characterize spin-liquid *Ansätze* via the local Wilson loops gauge fluxes.

2.5.2.1 A brief introduction to the projective symmetry group

The projective symmetry group allows a complete classification of mean-field spin-liquid states on a specific lattice. As was mentioned in section 1.3.3, this method was first introduced by Wen [30] for Abrikosov fermion mean-field states. It has later been adapted to the SBMFT formalism by Wang on the triangular and kagome lattices [86] and was since then used on various systems ranging from the honeycomb and square lattices [87, 98] to three dimensional systems [99, 100].

To classify all spin-liquid states on a lattice, we need to find states described by *Ansätze* which respect all the symmetries of the system. That is, for an *Ansatz* $\{\mathcal{A}\}$, applying any combination $\mathcal{C}$ of symmetries of the system should not result in any change of $\{\mathcal{A}\}$.

Let us express it this way:

$$\{\mathcal{A}\} \xrightarrow{\mathcal{C}} \{\mathcal{A}\} \tag{2.56}$$

The symmetries contained in the transformation $\mathcal{C}$ can correspond to point group symmetries and translations of the lattice as well as spin-rotation and time-reversal symmetries. Note that in some projective symmetry group approaches, some of those symmetries are allowed to be broken in order to classify more exotic spin-liquid states. For instance, allowing time-reversal symmetry to be broken gives acces to chiral spin liquids [88]. The same is true for point group symmetries of the lattice and nematic spin liquids [101].

However, the U(1) gauge freedom of equation 2.13 makes this picture slightly more demanding. Let us examine an *Ansatz* $\{\mathcal{A}\}$ not invariant by application of $\mathcal{C}$, that is $\{\mathcal{A}\} \xrightarrow{\mathcal{C}} \{\mathcal{A}'\}$. Now suppose the existence of a gauge transformation $\mathcal{G}$ turning the *Ansatz* $\{\mathcal{A}'\}$ back into $\{\mathcal{A}\}$. We would then have:

$$\{\mathcal{A}\} \xrightarrow{\mathcal{C}} \{\mathcal{A}'\} \xrightarrow{\mathcal{G}} \{\mathcal{A}\} \tag{2.57}$$

This means that we are looking for *Ansätze* that are invariant to a combined operation of a symmetry of the system and a U(1) gauge transformation. For a specific *Ansatz*, we call the set of all transformation leaving it invariant the projective symmetry group [30].

The projective symmetry group contains a particular subgroup, called the invariant gauge group (IGG). It is composed of pure gauge transformations leaving a specific *Ansatz* invariant without any supplementary symmetry transformation. In other words for $\mathcal{G} \in IGG$ we would have $\{\mathcal{A}\} \xrightarrow{\mathcal{G}} \{\mathcal{A}\}$. For the remaining of this section, we will restrict the discussion to the case of a $\mathbb{Z}_2$ IGG. This means that the subsequent classification will only concern $\mathbb{Z}_2$ spin liquids which are the natural spin-liquid states in the Schwinger boson framework [86].

Contrarily to the above discussion where we determined the set of transformation leaving a particular *Ansatz* invariant, also called invariant projective symmetry group, let us now focus on the symmetries of the model, without considering any prior *Ansatz*. The

algebraic relations between these symmetries can be used to classify all possible spin-liquid states. For the triangular lattice these algebraic relations are:

$$T_1 T_2 = T_2 T_1 \tag{2.58}$$
$$\sigma = \sigma^{-1} \tag{2.59}$$
$$C_6^5 = C_6^{-1} \tag{2.60}$$
$$T_1 C_6 = C_6 T_2^{-1} \tag{2.61}$$
$$T_2 C_6 = C_6 T_1 T_2 \tag{2.62}$$
$$T_1 \sigma = \sigma T_2 \tag{2.63}$$
$$C_6 \sigma C_6 = \sigma \tag{2.64}$$

where T_1 and T_2 are two translations, σ is a mirror symmetry and C_6 the six-fold rotational symmetry of the triangular lattice.

To classify spin-liquid states on a specific lattice, one needs to make sure that the algebraic relations between the symmetries of the system are verified, at least projectively, that is up to a gauge transformation. The algebraic relations will thus produce constraints on these possible gauge transformation and consequently on the spin-liquid states available on the lattice. The set of gauge transformations allowing one to projectively respect all symmetry relations correspond to the so-called algebraic projective symmetry group. Once it is determined, the set of such transformations gives a direct access to the possible spin-liquid states on the lattice.

On the triangular lattice for instance, Wang used the algebraic relations 2.58 to 2.64, to determine eight different set of gauge transformations corresponding to eight different SBMFT spin-liquid states [86].

2.5.2.2 0-flux and π-flux states on the triangular lattice

Assuming that nearest-neighbor A_{ij} amplitudes are not zero - which we can expect for a nearest-neighbor Heisenberg model - Wang further selected the remaining *Ansätze* to finally end up with only two states. These are called the 0-flux and π-flux states and are represented on figure 2.3.

The name of these two *Ansätze* is directly related to the local gauge flux of the rhombic Wilson loop represented by the dotted blue line in figure 2.3. The fluxes are of the form of the Φ_A flux in equation 2.55, meaning they are computed only from A_{ij} parameters. Following an oriented bond $(i \to j)$ on figure 2.3 yields a positive value of the corresponding A_{ij}. For both *Ansätze*, the amplitudes $|A_{ij}| = \mathcal{A}$ are uniform.

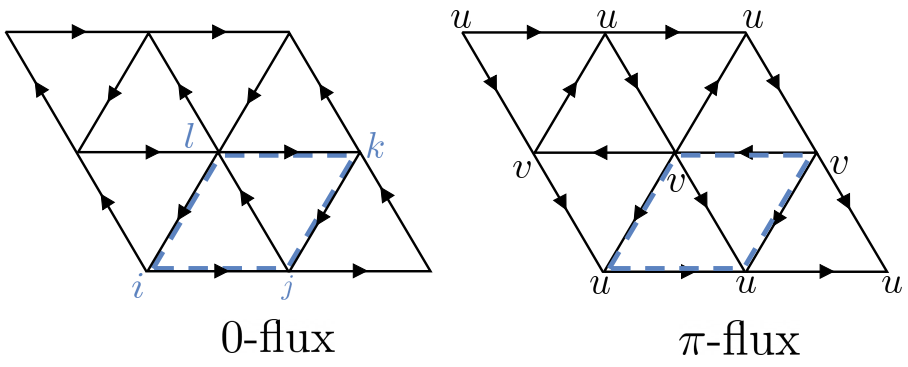

Figure 2.3: *Ansatz* of the 0-flux state on the triangular lattice (left). The oriented bond correspond to positive values of the A_{ij} mean-field parameters, the B_{ij} parameters are not represented. The flux of 0 is associated with the Wilson loop formed by the rhombus (dashed blue line). This loop is only composed of $\hat{A}_{ij}$ operators as in equation 2.55. *Ansatz* of the π-flux state on the triangular lattice (right). The unit cell needed to represent this state is doubled and both sublattices u and v are indicated on the figure.

Following the rhombus from site i to l on figure 2.3 (left), we compute the associated flux:

$$\Phi_A = \arg(\mathcal{A}^4 e^{i(0-2\pi+\pi-\pi)}) = 0 \tag{2.65}$$

Similarly for the *Ansatz* of figure 2.3 (right), starting from the u site on the bottom left and continuing clockwise, we have:

$$\Phi_A = \arg(\mathcal{A}^4 e^{i(0-2\pi+0-\pi)}) = \pi \tag{2.66}$$

In summary, the two *Ansätze* found by Wang, while they both respect all the symmetries of the triangular lattice (up to a gauge transformation), are actually characterized by the value of the local flux Φ_A on a rhombus that can be either 0 or π. We have thus shown a brief example where local Wilson loops help distinguish between different spin-liquid states.

Chapter 3

Topological Nematic Spin Liquid on the Square-Kagome Lattice

3.1 Motivations

The square-kagome lattice (SKL), composed of corner-sharing triangles, is a solid candidate to host various exotic phases due to its highly frustrated geometry. The simplest brick of frustration, the triangle, as already proven quite capable to foster debates on the nature of particular ground states, as is the case for the famous kagome spin$-1/2$ antiferromagnet. In this chapter, we will step aside from the cumbersome kagome problem to shed more light on the nature of the ground state of the spin$-1/2$ $J_1 - J_2$ Heisenberg model on the SKL.

The fact that the SKL is composed of two kinds of closed loops of length four (square plaquettes) and length eight (octagons), suggests that the resonance processes between singlet configurations are more local than in the case of the kagome lattice and thus hints at a potentially more tractable treatment of the quantum Hamiltonian. However, as we have seen in section 1.4.2.2, the nature of the quantum ground-state of the SKL remains elusive despite previous quantum studies [68, 70, 75]. Notably, around the point $J_1 = J_2 = 1.0$, reference [75] proposed a disordered ground state labelled "Y_a" and confirmed the presence of many low-lying singlets below the lowest magnetic excitation. In the framework of resonating valence bond theory, the ground state was thought to be the pinwheel VBC [75] while another study going beyond the nearest-neighbor valence bond basis found that the loop-six VBC was actually lower in energy [68].

Further study of the $J_1 - J_2$ square-kagome model is thus paramount to better understand the nature of its quantum ground states. This is where the unrestricted Schwinger boson algorithm will first show its strength. On top of its aforementioned versatility,

its mean-field nature allows the study of systems of very large sizes, which were inaccessible in previous calculations, especially in exact diagonalization. Consequently, we can better describe various quantities in reciprocal space such as the dispersion relations and static structure factors with an arbitrary low discretization, often reaching the thermodynamic limit.

Last but not least, the recent synthesis of an experimental compound exhibiting square-kagome geometry [6] represents further motivation for this quantum study. The characteristics of the model describing the experimental compound led us to consider the possibility of anisotropy between the J_2 bonds of the SKL in section 3.5, in order to connect our theoretical study to experiments.

The main results of our Schwinger boson study will be presented in the next section. We have established the full $J_1 - J_2$ quantum phase diagram on the SKL, provided a detailed description of the five different ground states as well as connection to future experimental results [102].

3.2 J_1-J_2 Phase Diagram

3.2.1 Methods and main results

In this section, a comprehensive description of the Schwinger boson quantum phase diagram will be provided. The corresponding model is the aforementioned spin$-1/2$ Heisenberg model:

$$\mathcal{H} = \sum_{\langle i,j \rangle} J_{ij} \hat{\mathbf{S}}_i \cdot \hat{\mathbf{S}}_j \tag{3.1}$$

with only nearest neighbor non-zero couplings J_1 and J_2, previously depicted in section 1.4.2. The analytical expression of the Schwinger boson mean-field Hamiltonian on the SKL is given in Appendix B.1.

Setting $J_1 = 1.0$ as the energy scale, we perform the self-consistent Schwinger boson algorithm for positive values of $x = J_2/J_1$ without imposing any *ad hoc Ansätze*. Still, many initial conditions were tested, some designed to mimic potential candidates such as the pinwheel and loop-six valence bond crystals from references [68, 75]. Others, and most of them, were completely randomized. Once the initial conditions selected, we recalculate the mean-field parameters by solving the Schwinger boson self-consistent equations until we reach convergence, ensuring at each step that the constraint on the number of boson is respected on average by modifying the Lagrange multipliers. Our criterion to ensure a correct convergence was an arbitrary tolerance of at least 10^{-9} on the mean-field parameters and 10^{-12} on the energy.

For most of the following calculations, we have used a unit cell of $n_u = 6$ sites since our

calculations on bigger unit cells, up to $n_u = 24$, yielded the same ground states. For the $n_u = 6$ unit cell, represented in figure 3.1, an *Ansatz* is composed of 6 Lagrange multipliers as well as 24 mean-field parameters. Each of the 12 oriented bonds composing the unit cell are described by two mean-field parameters A_{ij} and B_{ij}. The $n_u = 24$ unit cell will, however, be essential in determining the topological degeneracy of the spin-liquid ground state in section 3.2.6.

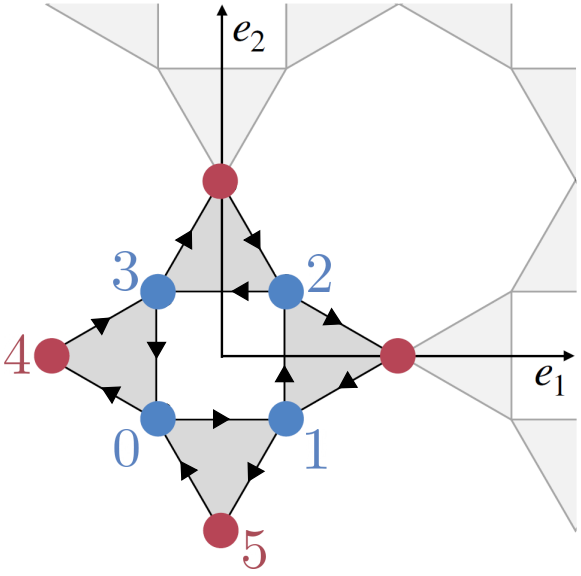

Figure 3.1: Unit cell for $n_u = 6$ on the SKL used for most of the following calculations. An *Ansatz* for this unit cell is composed of 6 Lagrange multipliers as well as 24 mean-field parameters. Each oriented bond corresponds to two mean-field parameters A_{ij} and B_{ij}. $\mathbf{e_1}$ and $\mathbf{e_2}$ are the translation vectors.

This work revealed five different ground states composing the full quantum phase diagram of the model. For low and large values of x, the presence of the plaquette and ferrimagnetic phases indicates that the algorithm is coherent with previous studies [70, 75]. Then, surrounding the $x \approx 1$ region, two gapless incommensurate magnetic orders appear (dubbed I1 and I2). Most interestingly these two long-range orders border a topological nematic spin liquid (TNSL), a disordered ground state present in an extended region around $x = 1$.

Before reviewing the characteristics of each ground state in detail, let us introduce three physical quantities that we will use throughout the description of the phase diagram. First, the energy gap Δ defined as the minimum of the lowest band of the dispersion relation. Its extrapolation in the thermodynamic limit is represented over the whole phase diagram on figure 3.2 (upper pannel). Then, the wave-vector $\mathbf{Q} = (Q, 0)$ or $(0, Q)$ minimizing the dispersion relation in the incommensurate orders and the TNSL phase is represented, after extrapolation in the thermodynamic limit, on figure 3.2 (middle

pannel). Finally, we define a flatness parameter σ corresponding to the cumulated standard deviations of each of the n_u bands of the dispersion relation:

$$\sigma \propto \sum_{\alpha=1}^{n_u} \sqrt{\sum_{\mathbf{k}} (\varepsilon^{\alpha}_{\mathbf{k}\uparrow} - \bar{\varepsilon}^{\alpha})^2} \tag{3.2}$$

where $\bar{\varepsilon}^{\alpha}$ is the average energy of the α-th band. For instance, this quantity is designed to be zero when all bands of the dispersion relation are flat. This flatness parameter is represented on figure 3.2 (lower pannel).

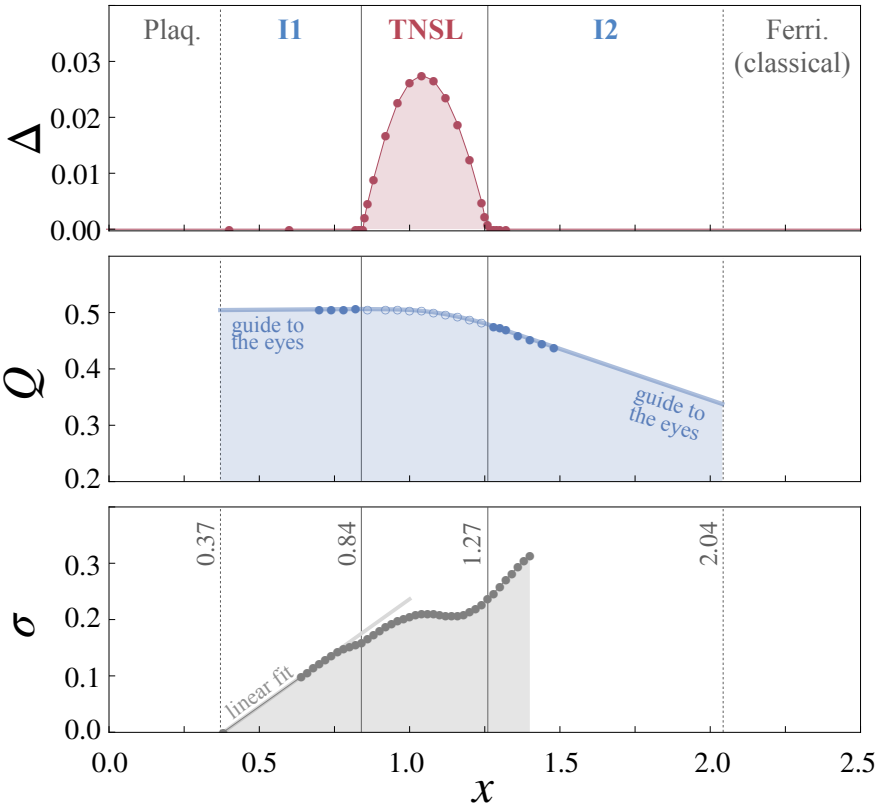

Figure 3.2: Quantum phase diagram of the SKL as seen through the energy gap Δ, the wave-vector $\mathbf{Q}$, extrapolated in the thermodynamic limit, as well as the flatness parameter σ. The wave-vector $\mathbf{Q} = (Q, 0)$ or $(0, Q)$ minimizes the dispersion relation of the TNSL (empty circles) and corresponds to the ordering wave-vector of the incommensurate orders (filled circles). The continuous (resp. dashed) vertical lines indicate second-order (resp. first-order) transitions.

3.2.2 The plaquette phase

The plaquette phase, previously described in [75] as the p-CD-VBC state and represented in figure 3.3 (left), is composed of resonating square plaquettes formed by the u sites. In our mean-field approach, spins on the v sites are uncorrelated which leads to a large degeneracy of this particular ground state. This degeneracy was hard to treat

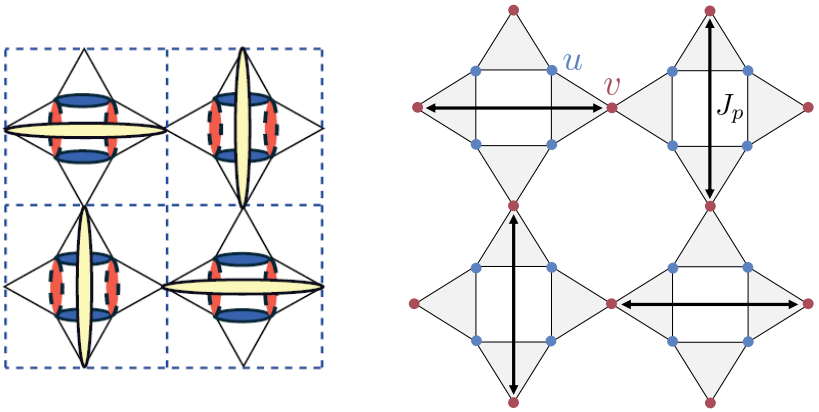

Figure 3.3: Crossed-dimer valence bond order configuration taken from [75] (left). Red and blue ovals represent the resonating square plaquettes while yellow ovals represent valence bonds connecting v sites. Configuration of the pertubative coupling J_p connecting v sites (right).

within our self-consistent algorithm because of the convergence issues it spawned. In order to overcome this issue, we introduced a perturbative antiferromagnetic coupling J_p between the v sites allowing one to lift the problematic degeneracy and proceed with the self-consistent procedure. We chose J_p to mimic the perturbative coupling responsible for the p-CD-VBC state which corresponds to the coupling represented in figure 3.3 (right).

Then, taking the limit $J_p \to 0$ and concretely speaking going as low as $J_p = 0.001$, we were able to trace back the actual energy of the plaquette phase on a large region of the phase diagram. Doing so, we ensured that the addition of J_p only lifted the degeneracy of the ground state without changing the physics of the system. Consequently, we found that the plaquette phase remains energetically stable up to $x \simeq 0.37(1)$ before the first incommensurate order becomes the ground state of the model through a first-order transition. Additionally, introducing J_p in the model leads to a gap opening for the plaquette phase, though it vanishes in the limit $J_p = 0$.

The resonating square plaquettes on the u sites correspond to local modes responsible for the presence of flat bands in the dispersion relation, reminiscent of the weather vane modes on the kagome lattice [103]. This is where the flatness parameter σ described earlier becomes relevant to define the boundary between the plaquette and I1 phases. Knowning that σ strictly equals zero in the plaquette phase, the flatness parameter is also measured in the I1 phase to determine the value of x at which it reaches zero. Computing σ implies to sum the standard deviation of all the bands of the dispersion relation of the I1 phase for a given x. Regrettably, the closer we get to the boundary with the plaquette phase, the more difficult it becomes to achieve convergence due in

particular to degeneracies and Bose condensations. Nonetheless, a linear extrapolation of σ, represented by the gray line in figure 3.2, shows that it vanishes when $x \simeq 0.38$. This is in good agreement with the previous energy consideration.

3.2.3 The ferrimagnetic phase

Let us turn to the $x \gg 1$ side of the phase diagram where the ground state is a Lieb ferrimagnet [76]. In the classical phase diagram, the ferrimagnetic phase is the ground state in the region $x > 2$ for Heisenberg spins [75] and in the region $x > 1$ for Ising spins [72]. As a reminder, the spin configuration of the ferrimagnetic order is represented on figure 3.4 (left).

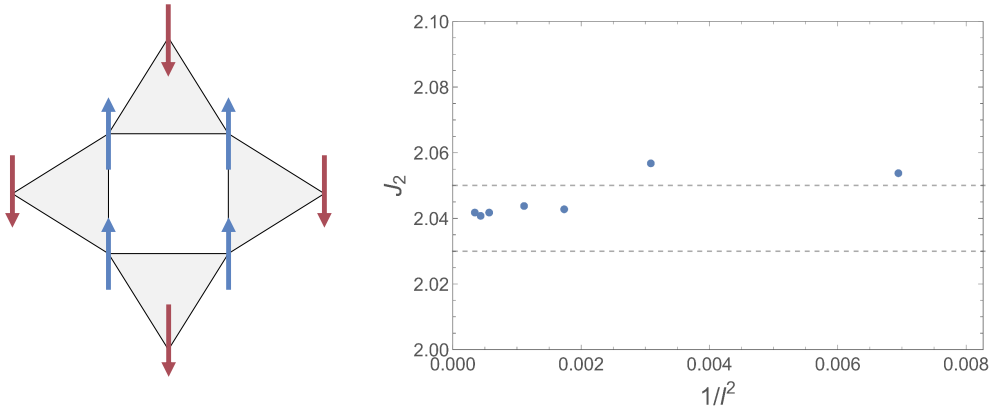

Figure 3.4: Configuration of the classical ferrimagnetic order on the SKL (left). Finite size study of the location of the boundary between the ferrimagnet and I2, up to $l = 54$. The boundary seem to go to $x \approx 2.04$ as the system size grows larger. Convergence issues prevented to reach larger system sizes.

Another problem arises for the determination of this boundary in the quantum case using SBMFT. In this formalism, convergence for quantum states outside the $S_z = 0$ sector is unattainable since the local constraints are violated, even on average [104]. Since it is the case for the present ferrimagnet, we were compelled to perform an alternative energy comparison to estimate the boundary with the second incommensurate order (I2). First, we define the classical energy of the ferrimagnetic phase per site, for a $n_u = 6$ unit cell on the SKL:

$$E_{\text{ferri}} = (4S^2 J_1 - 8S^2 J_2)/6 \tag{3.3}$$

Then, we monitor the level crossing between E_{ferri} and the extrapolated energy of I2 to determine the location of the boundary for a finite system size. Finally, we perform a finite size study up to $l = 54$ on the location of the boundary. This yields a value of $x \simeq 2.04$ compatible with the quantum boundary of $x \simeq 1.8$ in reference [75]. This finite size study is displayed in figure 3.4 (right).

The energy of I2 had to be extrapolated in the $x \approx 1.5 - 2.0$ region, once again due to convergence issues caused by Bose condensation. Because of this, we can not rule out the existence of an intervening additional phase in the region just below the ferrimagnet which could be similar to the "Ferri" phase described in reference [70] by a magnetization of $0 < M < 1/3M_{sat}$.

The locations of the ferrimagnetic and plaquette phases show how our SBMFT algorithm agrees with existing studies on the SKL. Let us now describe the incommensurate long-range orders I1 and I2 that were not reported in the literature so far.

3.2.4 The incommensurate orders

On both side of the central region of the phase diagram, two incommensurate long-range magnetic orders are found to be the ground states of the model. As said, these are the phases I1 and I2 on figure 3.2, extending up to the boundaries $x \simeq 0.37$ and $x \simeq 2.04$ described above.

Both I1 and I2 phases are described by condensation of the Schwinger bosons at an incommensurate wave-vector $\mathbf{Q}$ which takes the form $(Q, 0)$ or $(0, Q)$ by spontaneous symmetry breaking. The value of Q in the thermodynamic limit, displayed in figure 3.2 (middle pannel), was determined applying the procedure described in Appendix B.2. In short, performing a finite size study of the mean-field parameters of a given *Ansatz* shows that their values remain constant for large enough system sizes. We then use these values to bypass the self-consistent procedure and the associated convergence time allowing a much faster computation of physical quantities for larger sizes. Moreover, it is then possible to compute the dispersion relation in the continuum (limit of an infinite system size) and minimize it in order to find the value of Q in the thermodynamic limit.

Unfortunately, computing Q with this procedure is not always feasible for the incommensurate orders. Again due to convergence problems caused by Bose condensation, we do not have access to the asymptotic *Ansätze* described earlier for values of x near the boundaries with the plaquette and ferrimagnetic phases. It concerns for instance the whole $x \approx 1.5 - 2.0$ region for I2.

Keeping in mind the incommensurate value of the ordering wave-vector $\mathbf{Q}$, it is rather simple to understand why these long-range orders are not accessible through conventional exact diagonalization studies [70, 75]. The system size is a strong limiting factor in such computations (≈ 30 sites) while we were able to study systems up to 62424 sites thanks to the mean-field approach. However, working with twisted periodic conditions [105] could allow one to find such incommensurate orders even in the framework of exact diagonalization.

Using once more the procedure of Appendix B.2, we minimized the dispersion relation in the continuum using asymptotic mean-field *Ansätze* to find the value of the energy gap Δ in the thermodynamic limit. We were thus able to ensure that Δ is indeed zero in the whole region of I1 and I2. Openings of the energy gap at $x = 0.84$ and $x = 1.27$ define the boundaries with certainly the most interesting ground state of this model.

3.2.5 The topological nematic spin liquid

Let us now introduce the topological nematic spin-liquid phase stable on the region $x \in [0.84, 1.27]$.

First, the energy gap Δ becomes finite in this region even if it remains quite small (around 10^{-2}) indicating the absence of long-range dipolar order. The value of Δ in the thermodynamic limit was extracted with the same procedure used for the incommensurate orders (see Appendix B.2).

3.2.5.1 Nematic order parameter

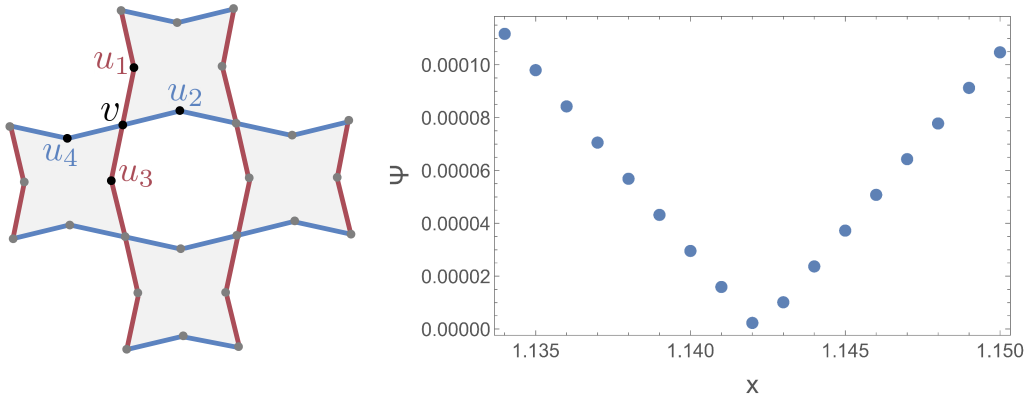

Figure 3.5: The J_2 bonds on the SKL form a decorated square-lattice with horizontal and vertical zig-zag lines (left). The amplitudes of the mean-field parameters on one type of zig-zag lines are uniform, but different wether they belong to the horizontal (blue) or vertical ones (red). The v site and its four u_d nearest neighbors are illustrating the computation of Ψ. Evolution of the directional order parameter Ψ in a small region around $x = 1.142$ (right). Interestingly, Ψ becomes zero for $x \approx 1.142$ yielding a true quantum spin liquid with no nematicity.

Second, a close look at the amplitudes of the A_{ij} and B_{ij} mean-field parameters reveals that they are uniform on the J_1 bonds of the lattice but surprisingly not on the J_2 bonds. The uniform singlets on the J_1 bonds are located on the square plaquettes. In turn, the J_2 bonds on the SKL form a decorated square lattice that can be represented with vertical and horizontal zig-zag lines, as can be seen on figure 3.5 (left).

The amplitudes of the mean-field parameters belonging to one type of zig-zag lines are uniform but a small discrepancy appears between the horizontal and vertical lines. This

results in a $\pi/2$-rotational symmetry breaking justifying the nematicity of the ground state. Naturally, this symmetry breaking leads to a twofold degeneracy of the TNSL.

The nematicity of the TNSL can be monitored thanks to a directional order parameter Ψ, defined as:

$$\Psi = |\sum_{d=1,4} (-1)^d \langle \hat{\mathbf{S}}_v \cdot \hat{\mathbf{S}}_{u_d} \rangle| \tag{3.4}$$

where we average over the four nearest neighbors u_d of a v site. For a symmetric spin liquid respecting all the symmetries of the system, the four $(v \to u_d)$ bonds are equivalent, yielding $\Psi = 0$. Ψ becomes non-zero in the TNSL phase since these four bonds are inequivalent because of the rotational symmetry breaking.

The nematicity of the TNSL remains small on the whole $x \in [0.84, 1.27]$ region, with $\Psi = 0.0014$ at $x = 1$ for example. However, for a particular value of $x \approx 1.142$, Ψ goes to zero restoring the rotational symmetry of the lattice. At this particular point, the ground state can be considered a true quantum spin liquid since all symmetries are restored. The evolution of Ψ in this region is depicted on figure 3.5 (right).

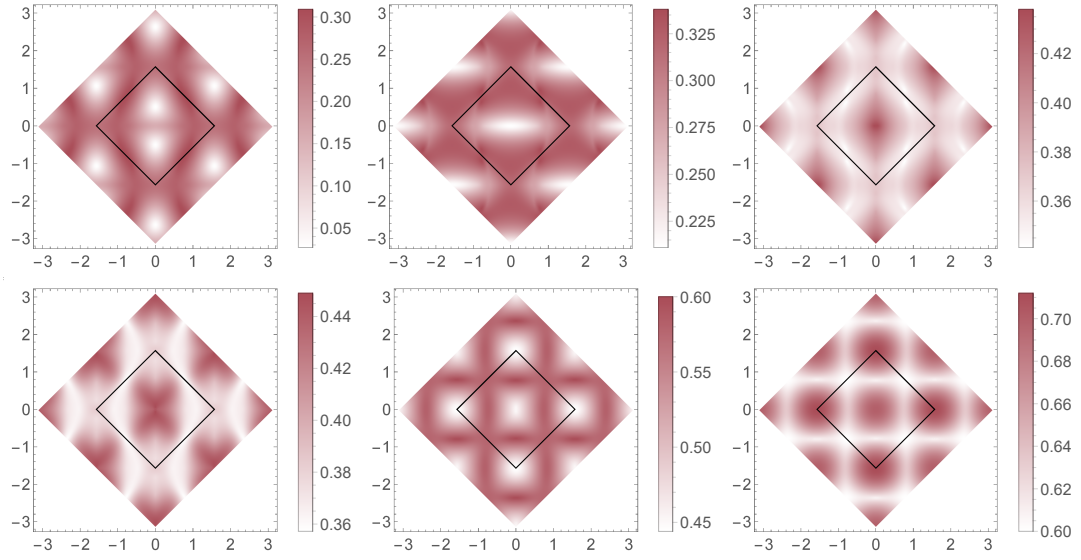

Figure 3.6: Dispersion relation of the TNSL at $x = 1$. Each graph correspond to the dispersion relation of one of the $n_u = 6$ bands. The first band (lowest energy) is displayed at the upper left, the second on its right and so on. The rotational symmetry breaking is clearly visible on the first two bands for instance.

A straightforward way to observe the nematicity of the TNSL consists in looking at its dispersion relation. The six dispersion relations, corresponding to the $n_u = 6$ bands of the system are represented on figure 3.6. For instance, the first two bands display a clear $\pi/2$ rotational symmetry breaking induced by the nematicity of the TNSL. This symmetry breaking is visible on other physical quantities describing the TNSL phase, such as its static structure factor and, as we will see later, its dynamical structure factor.

3.2.5.2 Local Wilson Loops

Third, the TNSL present non-zero fluxes on specific Wilson loops hinting at the structure of the associated quantum order. Fluxes on the square plaquette loops is strictly zero. Still, we have on the one hand elementary plaquettes of six sites for $\hat{A}_{ij}$ operator loops and, on the other, elementary triangles for $\hat{B}_{ij}$ operator loops, all of which displaying non-zero fluxes $\Phi_A = \pi$ or $\Phi_B = \pi$. These local Wilson loops are the smallest loops on the SKL with non-zero flux and are represented on figure 3.7.

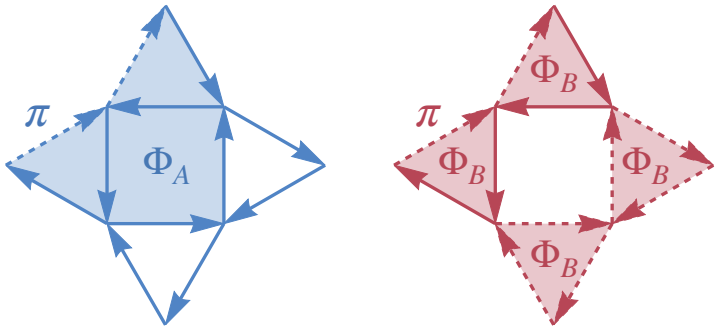

Figure 3.7: Local Wilson loops constructed with $\hat{A}_{ij}$ operators (left) and $\hat{B}_{ij}$ operators (right). The dashed lines represent the additional phase of π for the corresponding negative mean-field parameters on those links. A π rotation of the blue $\hat{A}_{ij}$ Wilson loop also yields a flux $\Phi_A = \pi$.

The expression of the fluxes Φ_A and Φ_B are the following:

$$\Phi_A = arg\big(\langle \hat{A}_{ij}(-\hat{A}^*_{jk})\hat{A}_{kl}(-\hat{A}^*_{lm})\hat{A}_{mn}(-\hat{A}^*_{ni})\rangle\big) \tag{3.5}$$

$$\Phi_B = arg\big(\langle \hat{B}_{ij}\hat{B}_{jk}\hat{B}_{ki}\rangle\big) \tag{3.6}$$

They are computed from the converged *Ansatz* of the TNSL taking into account the oriented links of the lattice and the negative sign of some mean-field parameters resulting in additional phases of π in the calculation (dashed lines of figure 3.7). Note that the six sites plaquettes forming the $\hat{A}_{ij}$ Wilson loop are invariant under rotation of π, but not under rotation of $\pi/2$ which is coherent with the nematicity of the TNSL.

These non-zero fluxes on specific Wilson loop could help in determining the underlying quantum order of the TNSL phase, especially in light of a future classification of all spin-liquid states on the SKL, using the projective symmetry group[1]. A thorough study of the fluxes of the TNSL could also determine the set of independant fluxes describing the TNSL [88] thus allowing the comparison with potential projective symmetry group *Ansätze*.

[1]This projective symmetry group study on the SKL would have to allow rotational symmetry breaking in order to classify not only all spin-liquid *Ansätze* but also all nematic phases such as our TNSL.

But before finishing the full characterization of the phase diagram, let us finally ensure that the TNSL possesses, as expected in the SBMFT formalism, a $\mathbb{Z}_2$ topological degeneracy.

3.2.6 Topological degeneracy of the TNSL

3.2.6.1 Winding Wilson Loops & Method

Projective symmetry group studies classifying Schwinger boson *Ansätze* [86–88] focus on finding states with a $\mathbb{Z}_2$ topological degeneracy. Here we make certain that the TNSL phase described earlier, after convergence of the self-consistent SBMFT algorithm on a finite system, indeed displays such a fourfold topological degeneracy.

Following the method described in reference [106], we want to construct the *Ansätze* that could correspond to the different topological sectors of the TNSL phase. First, we know that quantum spin-liquid states obtained from a parton construction remain locally indistinguishable degenerate states when one pierces the torus with additional gauge fluxes [106]. Moreover, in the case of $\mathbb{Z}_2$ spin-liquid states within SBMFT formalism only two options are available, that is the insertion of a flux of π or no flux insertion at all [106]. This flux insertion amounts to shifting the spinon boundary conditions from periodic (0-flux) to antiperiodic (π-flux). Consequently, we will now define the four topological sectors in unit of π as $(0,0)$, $(1,0)$, $(0,1)$ and $(1,1)$ directly showing a flux insertion or not in the two natural directions of the torus. These fluxes are easily accessible within SBMFT simply by considering two winding Wilson loops encompassing the whole torus in its two directions. They are represented on figure 3.8 and for the remaining of the section we will consider that they are computed using only $\hat{A}_{ij}$ operators. In short, computing the flux associated with these two non-local winding Wilson loops for a given spin-liquid *Ansatz* allows one to directly find the nature of the associated topological sector.

However, we first need to construct the different topological sector *Ansätze*. We do so, following [106], by introducing cut lines that pass through the bonds of the lattice, avoiding any lattice site. They are represented in red and blue in figure 3.9 (upper left pannel). The effect of such a cut line on any given *Ansatz* will be to change the sign of the mean-field parameters of every link that crosses that line.

Concretely, we use two operators $\hat{T}_1$ and $\hat{T}_2$ to mimic the effect of the cut lines. They act on a bond operator $\hat{\mathcal{O}}_{ij}$ as follows:

$$\hat{T}_{1,2}\hat{\mathcal{O}}_{ij} = \mp\hat{\mathcal{O}}_{ij} \tag{3.7}$$

where the minus sign is applied if the bond $(i \to j)$ crosses the cut line. Once the

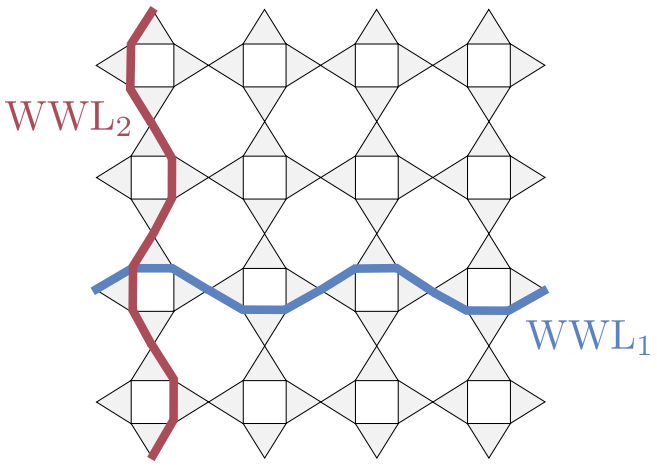

Figure 3.8: The two non-local winding Wilson loops in the two different direction of the torus for the SKL. Each loop has an associated gauge-invariant flux of either 0 or π leading to a potential fourfold topological degeneracy of the studied Ansatz.

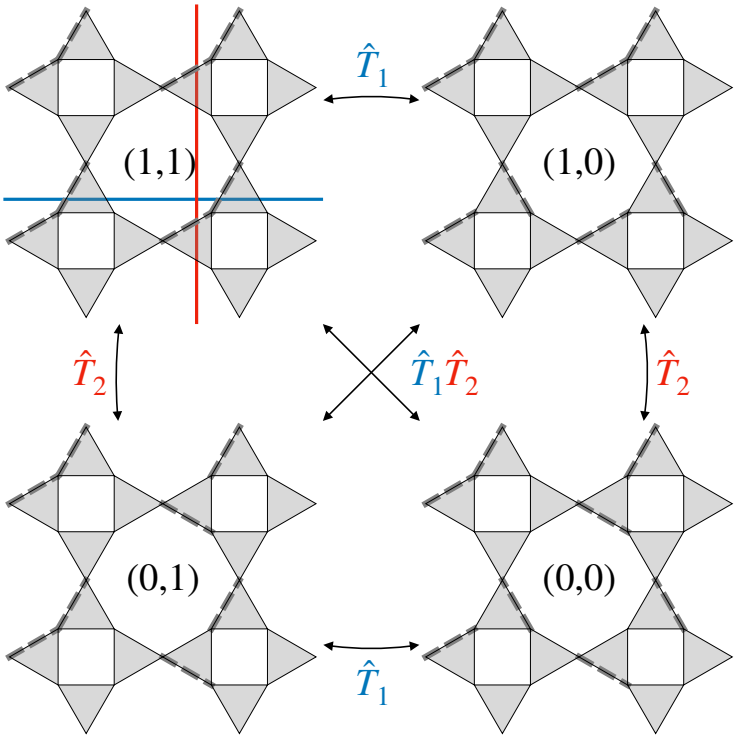

Figure 3.9: Description of the four topological sectors of the TNSL through their mean-field *Ansätze* on the $n_u = 24$ SKL. The gauge-invariant fluxes defining each sector are indicated at the center of the octagons, they are computed via the winding Wilson loops of figure 3.8. Going from one topological sector to another requires the application of $\hat{T}_1$ and/or $\hat{T}_2$. It corresponds to a shift in sign of the mean-field parameters on every link that crosses the $\hat{T}_1$ and/or $\hat{T}_2$ winding cut lines. The dashed bonds correspond to negative values of A_{ij}. The oriented links are not represented here for clarity.

operators $\hat{T}_1$ and/or $\hat{T}_2$ are applied on a whole *Ansatz*, it changes the corresponding mean-field parameters yielding a new *Ansatz* which belongs to a different topological sector. This method of constructing different topological sectors using cut lines on a lattice is reminiscent of the one used to determine topological order in quantum dimer model [107–109].

3.2.6.2 Topological Sectors of the TNSL

Starting from the TNSL *Ansatz* described above, we first compute the winding Wilson loops fluxes and find that the associated topological sector is $(1, 1)$, that is, an additional flux of π in the two natural directions of the torus. Then, by applying to this *Ansatz* the operators $\hat{T}_1$, $\hat{T}_2$ and finally $\hat{T}_1\hat{T}_2$ we construct the *Ansätze* of all four topological sectors. This process is depicted on figure 3.9 along with the operators needed to go from one sector to another. The dashed bonds on each *Ansatz* represent the negative mean-field parameters A_{ij} that need to be carefully taken into account when computing the winding Wilson loop fluxes. Finally, we ensured that the local properties as well as the physical parameters of each topological sector remained the same as in the TNSL phase.

The previous construction is quite straightforward to picture in real space, as represented in figure 3.9. In reality, working in Fourier space using our SBMFT algorithm, we have to pay closer attention to the matter. Indeed, by introducing a single cut line on the $n_u = 24$ unit cell of reference, we then generate l cut lines for our system of linear size l. As a consequence, an additional π flux per cut line in the unit cell of reference will result in a total additional flux of $l\pi$. Thus, it is worth emphasizing that no flux insertion is possible for systems of even linear sizes since $l\pi \equiv 0[2\pi]$. . Whereas systems with odd linear sizes have no restriction on having an additional flux of $l\pi \equiv \pi[2\pi]$.

3.2.6.3 Topological Degeneracy of the TNSL

A final calculation is needed to reveal the topological degeneracy of the TNSL. Now, we simply have to show that all of the four *Ansätze* that we constructed (see figure 3.9) are indeed degenerate. To do so, the energy of the four preceeding *Ansätze* as a function of the system size is given in figure 3.10. It is important to state that all of the four *Ansätze* passed the self-consistent procedure for the different system sizes of figure 3.10. We computed the energy of the TNSL in the thermodynamic limit, represented in light gray in the figure, using the method presented in Appendix B.2 for $l = 900$ unit cells.

As mentioned earlier, for even system sizes, we cannot insert any gauge flux through the torus. In this case, all of the four considered *Ansätze* are in the $(0, 0)$ sector and are degenerate. Their energy is represented in blue in figure 3.10. On the other hand, for odd and finite system sizes, the energy of the four topological sectors is different.

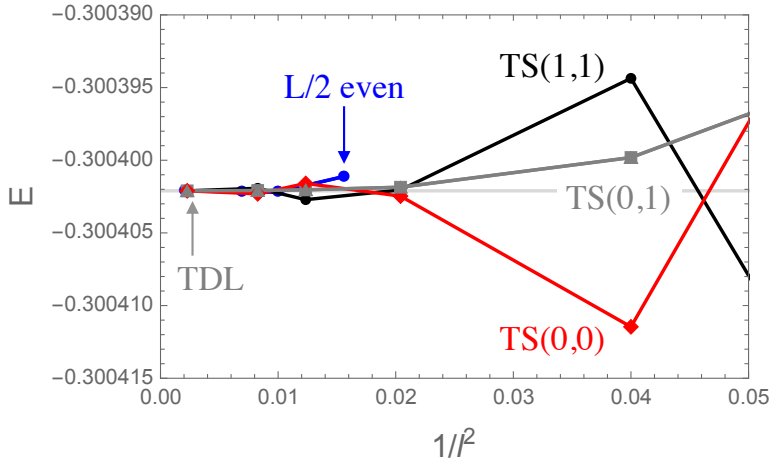

Figure 3.10: Energy of the four different topological sectors of the TNSL as a function of $1/l^2$ where l is the linear size of the system. The energy of the TNSL (lighter gray line) in the thermodynamic limit was obtained using an asymptotic *Ansatz* and a linear system size of $l = 900$ unit cells. For even system sizes, the energy of the four *Ansätze* is strictly the same and is represented in blue. For odd system sizes, the energies of the four topological sectors $(0, 0)$ (red line), $(1, 1)$ (black line), $(0, 1)$ and $(1, 0)$ (both darker gray line) all converge to the thermodynamic limit as the linear size of the system grows larger.

More precisely, we have three different energies, one for $(0, 0)$, a second for $(1, 1)$ and a third for $(1, 0)$ and $(0, 1)$. However, as the system size grows larger, all of these energies converge to the same thermodynamic limit. This is the final element needed to ensure that the TNSL indeed present a fourfold topological degeneracy, with four well-defined topological sectors. In each of these sectors, the local Wilson loop fluxes as well as the observable physical quantities are preserved. Finally, it is important to note that the fourfold degeneracy of the TNSL is in fact enhanced to eightfold when considering the additional twofold degeneracy induced by the rotational symmetry breaking of the lattice.

The study of the $\mathbb{Z}_2$ topological degeneracy of the TNSL concludes the description of this phase diagram. Before we focus on another model in chapter 4, let us address some important questions, such as the potential connection of this work to experiments as well as a discussion on the possibility to get insight on what happens beyond the mean-field approximation of the SMBFT formalism.

3.3 Going beyond mean-field

The properties of the different SBMFT ground states of the J_1-J_2 Heisenberg model on the SKL have now been described in detail. Naturally, a crucial question arises as to the potential stability of our spin-liquid ground states beyond the mean-field approximation.

We can start the discussion by providing information on several excited states above the TNSL at $x = 1$.

First, motivated by the weak nematicity of the TNSL, we examined a first excited state dubbed TSL where the rotational symmetry is restaured. Concretely speaking, the A_{ij} mean-field parameters are uniform on all the J_1 bonds *and* on all the J_2 bonds in this state. Next, going back to previous studies on the SKL [68, 75], we constructed two *Ansätze* that accomodate the pinwheel (PW) valence bond crystal as well as the loop-six (L6) valence bond crystal. To do so, we started with initial conditions in which the links containing a singlet on the valence bond configuration have a finite and real A_{ij} while the other links have A_{ij} set to zero. The non-zero $(i \to j)$ links are represented by blue singlets on the two top framed configurations of figure 3.11.

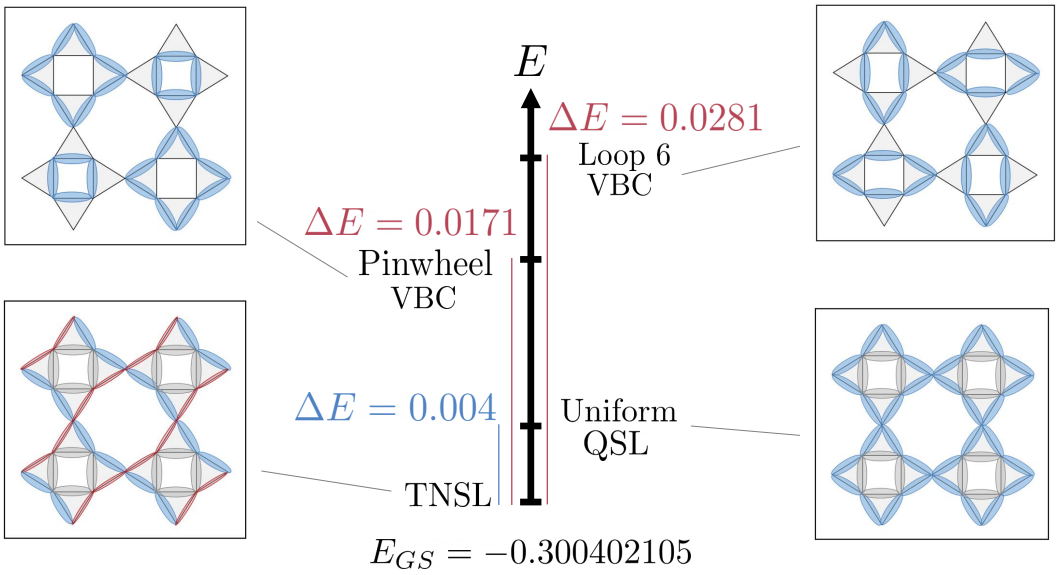

Figure 3.11: Energy landscape of the SKL model at $x = 1$. The ground state energy E_{GS} corresponds to the TNSL phase. The excitation energies of the TSL phase, the loop-six and pinwheel VBC are represented vertically. The four *Ansätze* are depicted with different colors representing singlets of different amplitudes.

After the usual self-consistent procedure, we managed to stabilize all three *Ansätze* confirming that they are metastable states of our model. Their respective excitation energies are represented on figure 3.11. They are also ordered below:

$$\Delta E_{\mathrm{TSL}} = 0.004 < \Delta E_{\mathrm{PW}} = 0.0171 < \Delta E_{\mathrm{L6}} = 0.0281 \tag{3.8}$$

The TSL phase is thus located closer to the ground state than the other two VBC, with an excitation energy one order of magnitude smaller. Moreover, if we compare the amplitudes of $\langle \hat{\mathbf{S}}_i \cdot \hat{\mathbf{S}}_j \rangle$ on either the J_1 and J_2 bonds between the TNSL and the TSL phases, we get less than 0.1% difference. These two arguments are in favor of a

spin-liquid scenario beyond mean-field, for instance in the form of a quantum spin liquid with hidden nematic order, as originally defined in reference [31]. They seem to discard the VBC scenario that was commonly accepted until then.

However, an important issue with our mean-field method is that we cannot determine the long-range ordered or disordered nature of the singlets. Consequently, we cannot establish the spin-liquid or VBC nature of the converged *Ansätze* with absolute certainty. Developing our SBMFT algorithm so that it would in some extent go beyond the mean-field approximation could provide more accurate answers than the previous development.

Another solution would be to get insight from alternative numerical methods such as DMRG that could potentially confirm the spin-liquid scenario we proposed using SBMFT. Fortunately for the SKL model, we can also expect further insight from future experimental studies since the synthesis of the compound in 2020 [6]. The next sections will be in fact dedicated to the connections between this theoretical work and experimental studies.

3.4 Experimental signature of the different ground states

Dynamical structure factors are very relevant physical quantities that allow forthright comparison of theoretical calculations and experimental measurements. As we have seen in section 2.4.4, the dynamical structure factors is on the one hand directly extractable from inelastic neutron scattering experiments and, on the other, directly computable within our SBMFT formalism.

We have chosen to compute $S(\mathbf{k}\ ,\omega)$ on a specific path connecting high symmetry points in the first Brillouin zone of the SKL. This path is represented in figure 3.12. It is composed of two similar subparts that are connected by a rotation of $\pi/2$. For the ground states where the rotational symmetry of the lattice is broken such as the TNSL, those two subparts should not be equivalent and should result in different spectral weights in the dynamical structure factor. In other words, this particular path is a tool to detect the nematicity of our ground states that could also be used in neutron scattering experiments.

After computing $S(\mathbf{k},\omega)$ for each of our ground states, we normalize them setting the maximum to unity, following reference [95]. The resulting dynamical structure factors for the plaquette phase, the incommensurate orders and the TNSL are displayed below in figure 3.13. We remind that it was impossible to reach convergence for the ferrimagnet phase with our procedure.

First, we observe the presence of flat bands on the structure factor of the plaquette

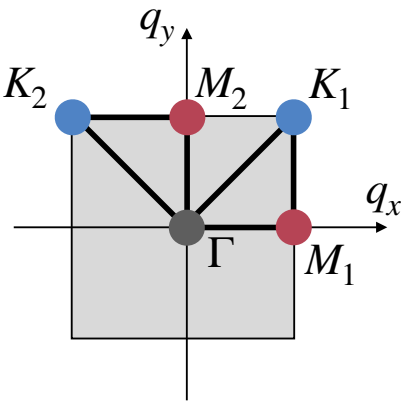

Figure 3.12: Path in the first Brillouin zone of the SKL used for the dynamical structure factors of the various ground states. This path is composed of two subparts related by a rotation of $\pi/2$ and connecting similar high symmetry points. This path will thus naturally reveal the nematicity of the TNSL phase in its dynamical structure factor.

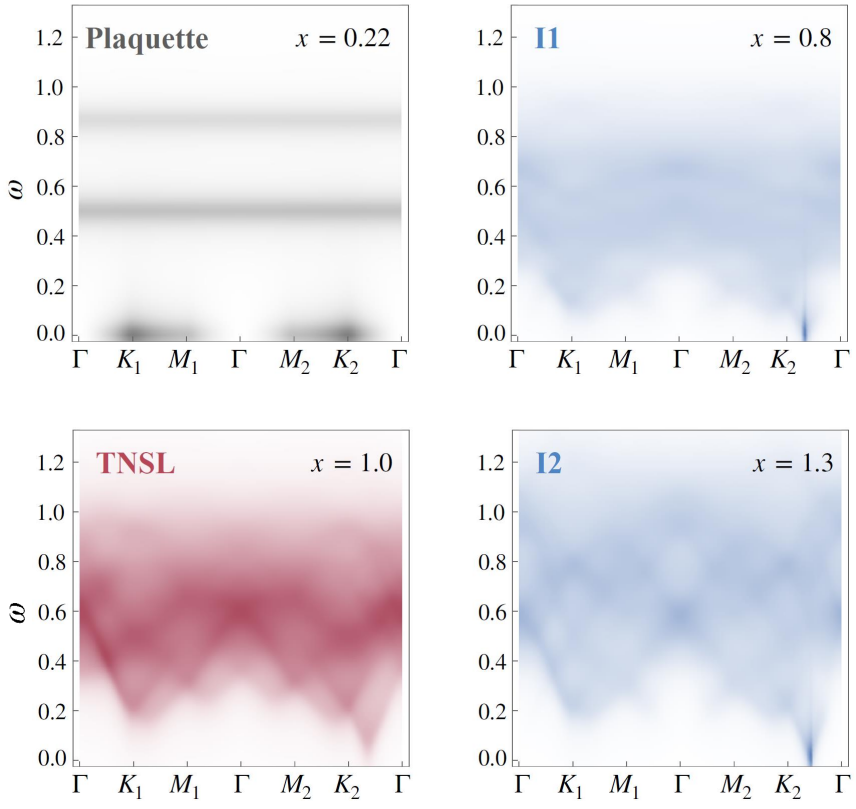

Figure 3.13: Dynamical structure factors of the ground states of the J_1-J_2 model. The maximum of $S(\mathbf{k}, \omega)$ is set to unity for each ground state. The right and left part of each plot correspond to a similar path but with a $\pi/2$ rotation (see figure 3.12). The nematicity of the TNSL phase is demonstrated since the two subparts of the path in the Brillouin zone are not equivalent. It is also the case for the incommensurate orders. The small gap of the TNSL is not visible at this scale. This is also the case for the gap of the plaquette phase, where we set $J_p = 10^{-3}$. The spectral weight for low values of ω in the plaquette phase is expected to extend down at $\omega = 0$ in the limit $J_p = 0$.

phase at $x = 0.22$. They correspond to local modes stemming from the localized square plaquettes on the J_1 bonds. We have set J_p at 10^{-3} to best minimize its effect. However, even if we see spectral weight for low values of ω, the perturbative coupling still induces a small energy gap of 1.6×10^{-4}, not visible at this scale.

The dynamical responses of the three remaining ground states are quite similar. The three of them present different spectral weight on the two subparts of the Brillouin zone's path indicating rotational symmetry breaking, as expected for the TNSL. As for the incommensurate orders, the loss of the lattice rotational symmetry simply corrresponds to the choice of the ordering wave-vector $\mathbf{Q}$ that can either be $(Q, 0)$ or $(0, Q)$. The gap of the TNSL is not visible at this scale since $\Delta = 0.02626$ at $x = 1$. Finally, it is essential for future experimental studies to note that a few key features such as the gap and the intensity would allow for the comparison and distinction of these three dynamical structure factors.

We now have all the arguments to advocate for the following scenario: The TNSL phase actually originates from the quantum melting of the two neighboring incommensurate orders. This statement is first corroborated by the strong similarity between their different dynamical structure factors. Second by the smooth evolution of the wave-vector $\mathbf{Q}$ minimizing the dispersion relation through the boundary between the long-range orders and the TNSL (see figure 3.2). And third, by the smooth evolution of the gap near the boudaries of the TNSL phase (see figure 3.2) suggesting a second order phase transition.

These experimental signatures represent the final information we obtained on the J_1-J_2 SKL model. They may also provide insight to potential future experimental measurements.

3.5 An experimentally accessible spin liquid?

3.5.1 Stability of the TNSL against experimental distortion

All calculations performed so far were done before the publication of reference [6] describing in details the synthesis of the first SKL compound as well as the first experimental measurements. Still, thanks to reference [70] we knew the compound's physics would certainly be best described by a nearest-neighbor Heisenberg model with a further anisotropy between non-equivalent J_2 bonds originating from a lattice distortion. Let us introduce this additional coupling $J_2^{'}$ in the model and represent it on figure 3.14 (left). We wanted to test the stability of our newly proposed ground state, against the anisotropy between non-equivalent J_2 bonds to explore the possibility for the TNSL to be the ground state of the experimental compound.

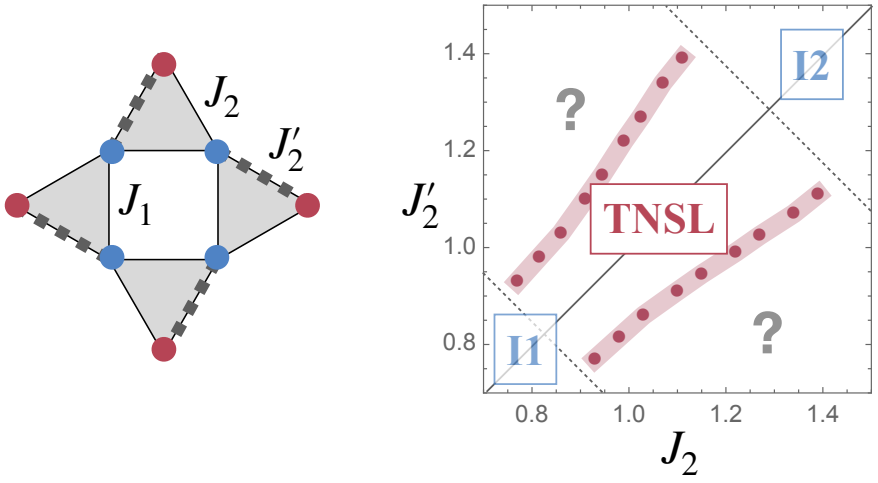

Figure 3.14: J_1-J_2-$J_2^{'}$ SKL model thought to model the compound's physics [6, 70] (left). Study of the stability of the TNSL against the J_2-$J_2^{'}$ anisotropy (right). The J_2=$J_2^{'}$ line corresponds to the phase diagram of figure 3.2. We monitored the point where the nematicity of the ground state was lost (red point) which corresponds to the TNSL's boundary. The TNSL phase remains stable in an extended region of this phase diagram. The thick red lines indicate the precision on the location of the boundary.

A partial J_2-$J_2^{'}$ phase diagram is depicted on figure 3.14 (right). The J_2=$J_2^{'}$ line corresponds to the phase diagram of the previous J_1-J_2 model of figure 3.2. The dashed line represent the boundaries previously described in section 3.2.5 at $x = 0.84$ and $x = 1.27$. Amongst the five ground states presented above, we have only tested the stability of the TNSL and did not explore the entire J_2-$J_2^{'}$ phase diagram.

In order to check rapidly the stability of the TNSL, we performed scans on lines perpendicular to the J_2=$J_2^{'}$ axis and carefully monitored the nematicity of the ground state, using the directional order parameter Ψ from section 3.2.5.1. The moment when Ψ goes to zero, that is when the nematicity of the ground state disappears, defines the location of the boundary of the TNSL. As depicted on figure 3.14 (right), the TNSL remains the ground state of the model in an extended region, whose boundaries are indicated by red circles. The thick red line represent our mesh precision on the location of the boundaries.

This result hints at the possibility for the experimental compound to host a quantum spin liquid with hidden nematic order as its ground state. However, since 2020, we have more information on the actual characteristics of the experimental compound [6].

3.5.2 Another candidate for the experimental ground state

The theoretical studies of reference [6] first seemed to indicate that the physics of the compound could be modelled with the previous J_1-J_2-$J_2^{'}$ Heisenberg Hamiltonian with

coupling strength of $J_2 = 1.2$ and $J_2' \equiv 0.85$ given here in units of J_1. These coupling values unfortunately fall outside the region of stability of the TNSL phase, as represented in figure 3.15 by the black star.

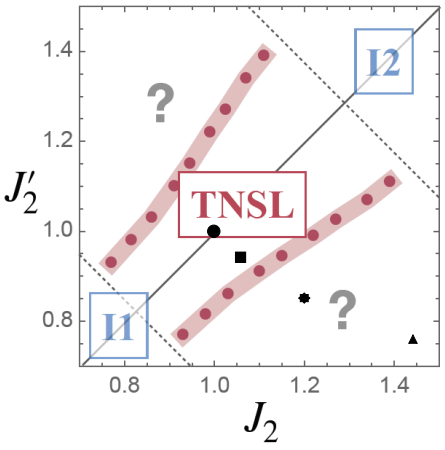

Figure 3.15: Location of the ground states studied in this section on the J_2-J_2' phase diagram. The black circle stands for the TNSL without anisotropy, the black square still corresponds to the TNSL but with $J_2 \neq J_2'$, the black star is located at coupling values coherent with the experimental compound and finally the black triangle is deeper in the new spin-liquid region.

With this new information in mind, it seems important to understand the nature of the ground state behind the boudary of the TNSL. We have yet again performed scans for various values of J_2 and J_2' but this time we did not stop when nematicity was lost. To illustrate our findings, we will study four different ground states alongside their experimental signatures to better understand this portion of the phase diagram. These four ground states correspond to the coupling values indicated in figure 3.15 by the black circle, square, star and triangle. The dynamical structure factors of these four phases are presented in figure 3.16.

The black circle corresponds to the TNSL phase at $x = 1$ without any anisotropy and was thouroughly described in section 3.2.5. The second ground state, represented by the black square, is still located in the region of stability of the TNSL but with some anisotropy between J_2 and J_2'. This ground state is still gapped and nematic and presents the same non-zero local Wilson loop fluxes than the TNSL at $x = 1$. Its dynamical structure factor shows a larger opening of the gap (on the right-hand side) with $\Delta \approx 0.0531032$ compared to $\Delta = 0.02626$ at $x = 1$ and still demonstrates the rotational symmetry breaking of the lattice.

Now, crossing the boundary of the TNSL, the black star corresponds to the values of the couplings describing the experimental compound. After applying the SBMFT self-consistent procedure, we found that the ground state was quite different from the

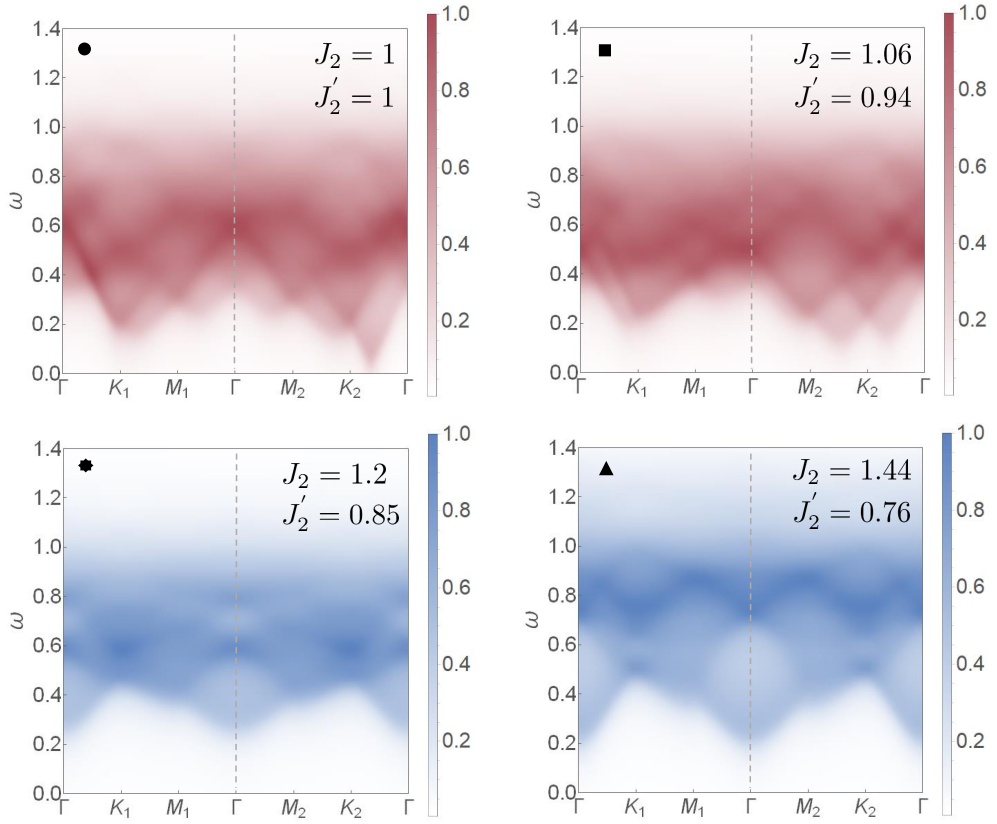

Figure 3.16: Dynamical structure factors of the four studied ground states on the J_2-J_2' model. The black circle corresponds to the previously studied TNSL phase without any anisotropy (upper left). The black square stands for the TNSL with a finite anisotropy (upper right). This phase is clearly gapped and we can still see the rotational symmetry breaking since the mirror symmetry of the paths in figure 3.12 is not present in the dynamical structure factor. The black star corresponds to a new gapped ground state (lower left). The nematicity is lost and the ordering wave-vector minimizing the dispersion relation is at the Γ point. The black triangle shows that this ground state also remains stable in an extended region of this phase diagram. As the anisotropy increases, the gap begins to close at the Γ point (lower right).

TNSL. Indeed, its experimental signature is significantly different, the nematicity is lost and the gap is much larger with $\Delta \approx 0.124623$. Moreover, the ordering wave-vector minimizing the dispersion relation is no longer incommensurate but coincides with the Γ point. All these characteristics are also present on the dynamical structure factor of figure 3.16 (lower left).

Focusing on the spin correlations in real space interestingly provides more information on this phase. The correlations are represented in real space for a system of linear size $l = 12$ in figure 3.17 (left). Starting from a site of reference, here the u site at the bottom, we display a blue dot for spins positively correlated with the spin of reference, that is $\langle \hat{\mathbf{S}}_{\text{ref}} \cdot \hat{\mathbf{S}}_j \rangle > 0$, and a red dot for negative correlations with the spin of reference.

The size of each dot is directly proportional to the amplitude of the correlation.

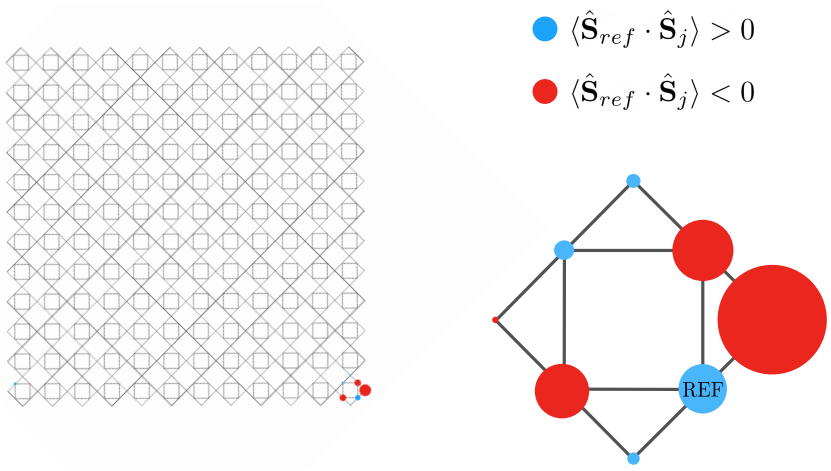

Figure 3.17: Spin correlations in real space for the new gapped phase (black star) on a 12×12 unit cells system with periodic boundary conditions (left). A blue dot indicates a positive correlation with the spin of reference while a red dot indicates a negative one. The amplitude of the correlations are proportional to the size of the dots. Correlations are non-zero close to the spin of reference (u site on the bottom right) but decrease rapidly in real space as expected for a gapped phase. Close-up view on the unit cell containing the site of reference (right). The correlations inside this unit cell seem to correspond to the "$J_1 - J_2$ Neel order" described in reference [70].

Looking at figure 3.17 (left), we first observe that the correlations are non-zero around the spin of reference but decrease rapidly with the distance. This is coherent with the finite gap of this ground state and thus the absence of magnetic long-range order. Second, if we pay closer attention to the unit cell containing the site of reference (see a close-up view in figure 3.17 (right)), the correlations follow a distinct pattern that seem to correspond to the "$J_1 - J_2$ Neel order" described in reference [70]. The spin configuration in this state is composed of Néel-ordered square plaquettes on the J_1 bonds, spins aligned in an antiparallel manner on the J_2 bounds as well as spins pointing in the same direction on the J_2' bounds. Our new ground state thus seems to be the spin-liquid version of this alternative Néel order, found to be stable in a very large region of the J_2-J_2' phase diagram in a previous exact diagonalization study [70].

Finally, though the exact boundary of this new spin-liquid phase is out of the scope of the present work, the coupling values defined by the black triangle, located deeper in the phase diagram, show that this gapped spin liquid is also stable in a large region. The associated dynamical structure factor show that the gap is beginning to close at the Γ point. This behavior accentuates as J_2 increases. It is most probable that, for high enough values of J_2, the gap would completely close to yield a long-range order with the "$J_1 - J_2$ Neel" spin configuration.

In summary, it is most interesting that, in the SBMFT framework, the couplings describing the experimental compound also yield a spin-liquid ground state even if it is not the TNSL phase. It seems to correspond to the gapped version of the "$J_1 - J_2$ Neel" long-range order described in reference [70]. Unfortunately, preliminary experimental studies point to a *gapless* spin-liquid ground state [6] which is typically the kind of ground state that is inaccessible through our SBMFT procedure. The question of the nature of our gapped ground state beyond the mean-field approximation remains unanswered. But a more important question may be to characterize precisely the model describing the compound's physics in order to follow with the appropriate theoretical studies.

3.6 Conclusion

To summarize, we have computed the full J_1-J_2 quantum phase diagram on the SKL unveiling five different ground states. Among them, the TNSL phase is certainly the most interesting, presenting a small but finite gap, a rotational symmetry breaking, non-zero fluxes on local Wilson loops and a fourfold topological degeneracy. We have provided dynamical structure factors for the different ground states allowing for the comparison with potential inelastic neutron scattering experiments.

To pursue connecting our work with experiments, we have tested the stability of our TNSL against a more realistic model, thought to describe best the physics of the SKL experimental compound. The TNSL remains stable over an extended region but that unfortunately does not encompass the particular coupling values characterizing the experimental compound. Still, at these coupling values, we found another gapped phase without any rotational symmetry breaking that could correspond to the liquid version of the "$J_1 - J_2$ Neel" long-range order described in reference [70]. This gapped phase also seems stable over an extended region of the J_2-$J_2^{'}$ phase diagram and is expected to become gapless for a strong enough anisotropy.

The first experimental measurements on the SKL compounds are pointing to a gapless spin-liquid ground state. However, experimental measurements and theoretical results obtained via DMRG do not agree on the inelastic neutron scattering results for the moment. A solution may be to take into account further interactions in the Heisenberg Hamiltonian in future theoretical studies.

A few directions are to be explored next on this subject. First, a better understanding of the model describing the compound's physics would be paramount to provide relevant theoretical studies that could be compared precisely to the experimental work. Then, remaining in the SBMFT framework, the question of the stability of the TNSL's gap and the nature of the ground state beyond the mean-field approximation remains

unanswered. Alternative methods such as DMRG, taking into account the possibility of rotational symmetry breaking, would be welcome to confirm our scenario. The J_2-$J_2^{'}$ phase diagram could be studied more completely to determine the region of stability of the new gapped spin-liquid and to verify if there is indeed a transition to the so-called "$J_1 - J_2$ Neel" order.

Last but not least, we can also expect some more insight from the experimental side, for instance if the SKL is realized in optical lattices [74] or if more compounds are synthezised in years to come. With a little bit of luck, one of them could even be characterized by coupling constants coherent with the location of the TNSL phase we have proposed.

Chapter 4

$J_1 - J_2 - J_3$ Heisenberg Model on the Kagome Lattice

4.1 Motivation and context

We have seen in chapter 1 that geometrically frustrated magnets such as the kagome spin$-1/2$ antiferromagnet have fostered a lot of interest in the past decades since they are expected to host a variety of exotic magnetic states. Quantum spin liquids, characterized by fractionalized excitations and topological properties, are a hallmark of such states and have been researched in many experimental compound candidates [5, 52, 54].

An interesting classical counterpart to these exotic quantum states is the classical spin ice state found for instance on the three-dimensional pyrochlore lattice. This state also exhibits fractionalized excitations called magnetic monopoles [12, 110] as well as a distinctive experimental signature in the form of pinch-points in the static structure factor. An example of such pinch points is displayed in figure 4.1 (left), taken from reference [111].

However, pinch-points are not specific to pyrochlore systems [17, 112]. Indeed, recent classical studies on the kagome lattice with $J_1 - J_2 - J_3$ antiferromagnetic couplings for both discretized [113] and continuous [114] spins found mutiple exotic ground states with structure factors exhibiting pinch-points as well as other distinctive features. The model is shown on figure 4.1 (right) where the J_3 coupling connects two sites in neighboring triangles.

On the kagome lattice, another configuration for the J_3 coupling exists. This alternative coupling, coined $J_3^{'}$ on figure 4.1 (right), rather links two sites across an hexagon. The corresponding $J_1 - J_2 - J_3^{'}$ model was actually studied more intensively [115–121] than its J_3 counterpart. As far as we know, the quantum version of the $J_1 - J_2 - J_3$ model

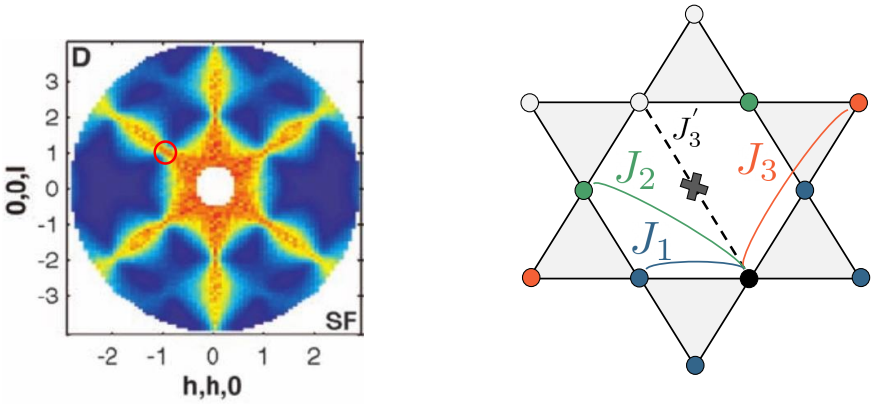

Figure 4.1: Static structure factor exhibiting pinch points computed via Monte Carlo calculations on the pyrochlore lattice, taken from reference [111] (left). The location of one of the pinch points is indicated by a red circle. $J_1 - J_2 - J_3$ model on the kagome lattice (right). The J_3 coupling connects two sites in neighboring triangles while the J_3' coupling connects two sites across an hexagon.

has only been recently studied using pseudofermion functional renormalization group (pf-FRG) [122].

In this paper, Buessen and Trebst discovered a variety of spin liquids and magnetically ordered ground states demonstrating the complex nature of the quantum $J_1 - J_2 - J_3$ Heisenberg model. In this context, it seems particularly interesting to probe this rich quantum model to determine the presence of potential quantum spin-liquid ground states in the Schwinger boson framework. Before doing so, let us briefly review in the next section the results of the previous classical studies on the $J_1 - J_2 - J_3$ model in order to introduce some essential concepts.

4.1.1 Classical study of the $J_1 - J_2 - J_3$ model

Mizoguchi *et al.* focused in reference [113] on the $J_1 - J_2 - J_3$ Ising model on the kagome lattice in the specific case where $J_2 = J_3 = J$, that is:

$$\mathcal{H} = J_1 \sum_{\langle i,j \rangle} \sigma_i^z \sigma_j^z + J \sum_{\langle\langle i,j \rangle\rangle} \sigma_i^z \sigma_j^z + J \sum_{\langle\langle\langle i,j \rangle\rangle\rangle} \sigma_i^z \sigma_j^z \tag{4.1}$$

where $\sigma_i^z = \pm 1$ is the Ising spin at site i.

On each triangle of the lattice, the spins can either all point in the same direction or one of them can point in the opposite direction as the two others. All possible spin configurations on a triangle are represented on figure 4.2 (left). For each of these

configurations, we can define a topological charge Q_p on a triangle p as:

$$Q_p = \eta_p \sum_{i \in p} \sigma_i^z \tag{4.2}$$

with η_p equals to 1 (resp. -1) for triangles pointing upward (resp. downard).

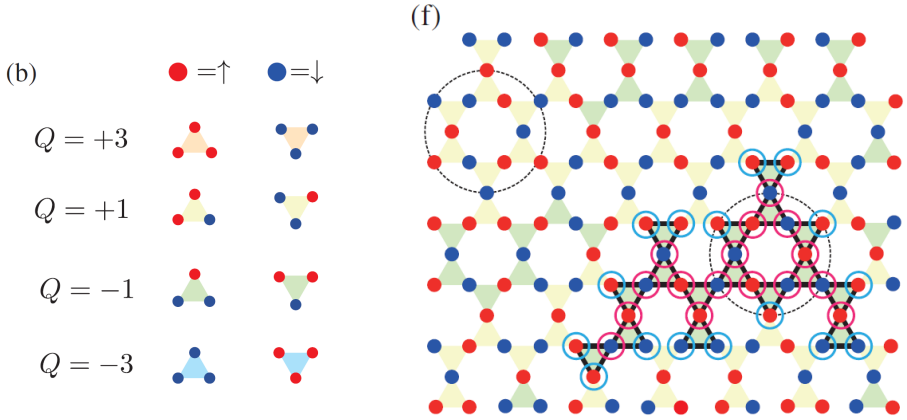

Figure 4.2: Possible Ising spin configurations on a triangle and their associated topological charges Q_p (left). Spin configuration of the hexamer classical spin liquid (right). The charge clusters are of two types with $Q_p = \pm 1$ and hexamers rings are represented by dashed circles. Figures taken from [113].

On the kagome lattice, the charges Q_p can thus take only four possible values: $Q_p = \pm 3$ for fully polarized triangles or $Q_p = \pm 1$ for triangles with one spin opposite to the two others, as indicated in figure 4.2 (left). Since each spin on the kagome lattice belongs to one up triangle and one down triangle, we can easily derive from definition 4.2 the following charge neutrality condition: $\sum_p Q_p = 0$.

Using these topological charges to rewrite the Hamiltonian allows one to easily determine the phase diagram of the Ising model. In terms of Q_p, the Hamiltonian takes the following form:

$$\mathcal{H} = (1/2 - J) \sum_p Q_p^2 - J \sum_{\langle p,q \rangle} Q_p Q_q \tag{4.3}$$

where the energy scale is fixed with $J_1 = 1$.

The term $\big(1/2 - J\big) Q_p^2$ corresponds to the self-energy of a charge on a triangle p while the second term of the Hamiltonian stands for the charge-charge interaction. Interestingly, we see that for an antiferromagnetic $J > 0$, the interaction between two charges of the same sign is attractive.

This charge attraction is in fact responsible for the apparition of a particular classical spin-liquid ground state for $0 < J < 1/3$. The spin configurations associated to this spin-liquid state consists in same-charge clusters accompanied by hexamers rings composed

of six triangles. A spin configuration corresponding to this ground state is depicted in figure 4.2 (right) where the charge clusters are of two types, *i.e.* $Q_p = \pm 1$, and where the hexamer rings are represented by dashed circles. Mizoguchi *et al.* showed that the presence of hexamers leads to a distinctive pattern in the static structure factor in the form of "half moons", that is two semi-circular areas of high intensity facing each other outside the first Brillouin zone. See figure 4.3 (left) for a depiction of the half-moon pattern.

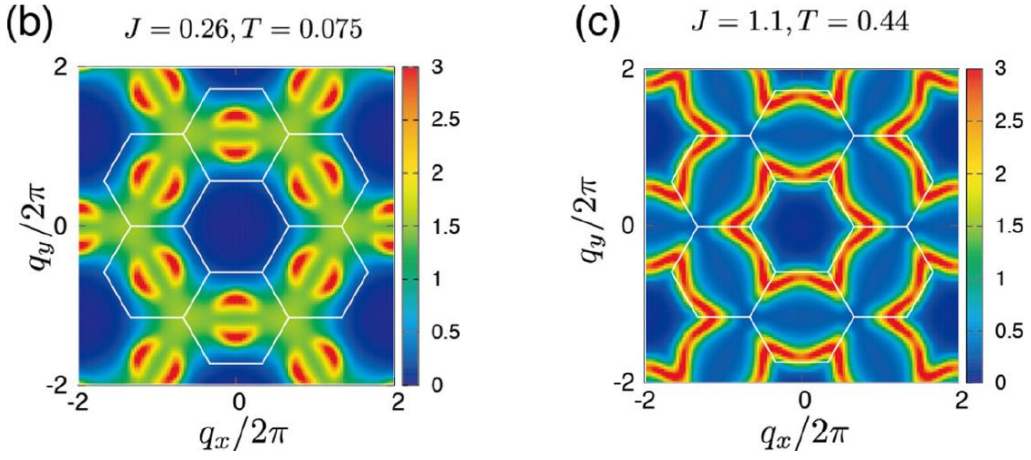

Figure 4.3: Half-moon (left) and star pattern (right) on the kagome $J_1 - J_2 - J_3$ Heisenberg model taken from the analytical large-N approach of reference [114].

The classical $J_1 - J_2 - J_3$ model has also been studied considering classical Heisenberg spins in reference [114]. Combining an analytical large-N approach and Monte Carlo simulations, Mizoguchi *et al.* were able to compute the phase diagram of the model. It is interestingly composed of ground states displaying, pinch points, half moons as well as star patterns in their static structure factors. See figure 4.3 (right) for a depiction of the star pattern.

More precisely, the phase diagram is composed of three different ground states. For $0 < J < 1/5$, the ground state is characterized by a flat band with pinch points in the static structure factor. For $J > 1/5$, a dispersive band becomes the ground state exhibiting half moons in the static structure factor, see figure 4.3 (right). As J increases the half moons continuously evolves into the star pattern of figure 4.3 (left). A final region of the phase diagram is located at $J > 1$ where the energy minima shifts in Fourier space.

The spin to charge mapping can be extended to the $J_1 - J_2 - J_3$ Heisenberg model by defining a local magnetic moment on each triangle p of the lattice:

$$\mathbf{M}_p = \eta_p \sum_{i \in p} \mathbf{S}_i \tag{4.4}$$

where $\mathbf{S}_i$ is the Heisenberg spin at site i and, again, η_p equals to 1 (resp. -1) for triangles pointing upward (resp. downard).

It is then possible to rewrite the Heisenberg Hamiltonian in a similar fashion as in equation 4.3:

$$\mathcal{H} = (1/2 - J) \sum_p |\mathbf{M}_p|^2 - J \sum_{\langle p,q \rangle} \mathbf{M}_p \cdot \mathbf{M}_q \tag{4.5}$$

Using this mapping, Mizoguchi *et al.* showed that the half-moon and star patterns were connected to the formation of magnetic clusters in real space, analoguous to the charge clusters of the Ising model [113]. In this analogy, the half moons are consequently connected to the classical hexamer clusters while the star patterns are connected to the triple-charge clusters [114].

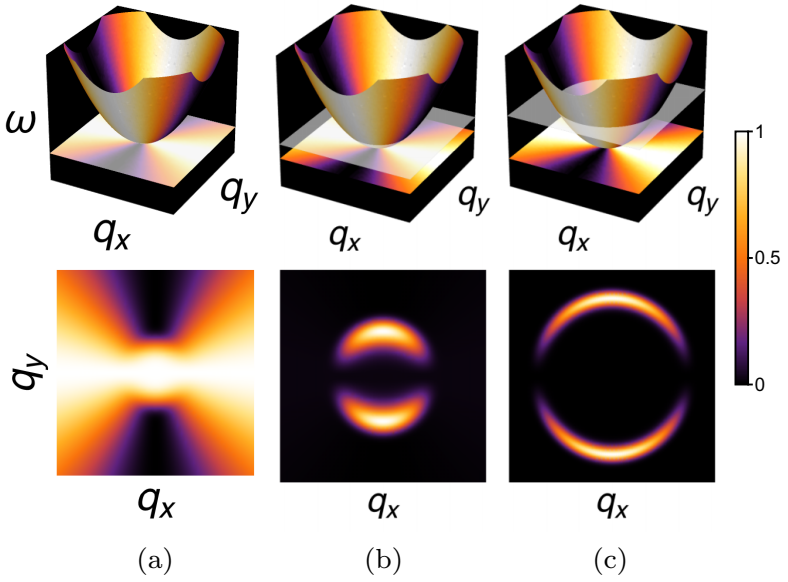

Figure 4.4: Schematization of the origin of half moons and its connection to pinch points, taken from reference [123]. On the upper pannels are displayed the spin excitation bands with cut at finite energy represented by the white planes. On the lower pannels are represented the corresponding dynamical structure factors at finite energy. The rotated pinch-point pattern encoded on the dispersive band yields the half-moon pattern at finite energy.

The scenario of reference [114] where the dispersive band becomes the ground state yielding half moons in the static structure factor is coherent with the explanation proposed by Yan *et al.* [123] for the presence of half-moons at finite energy in the context of a field-saturated state on the nearest-neighbor kagome antiferromagnet. As in [114], they showed that half moons actually originate from a dispersive band above the ground state's flat band associated to pinch points. The dispersive band displays an intensity pattern corresponding to pinch points, albeit rotated of 90 degrees. Taking a cut at

finite energy thus reveals the two crescent form of the half-moon pattern in a dynamical structure factor[1]. This phenomenon is summarized on figure 4.4, taken from reference [123].

Interestingly, the star pattern has also been seen in the structure factor of the spin$-1/2$ $J_1 - J_2 - J_3$ model using pf-FRG [122]. But its origin, connections to classical models and emergence of half moons for smaller values of $J_2 = J_3$, were not discussed at that time, as reference [122] pre-dates the works on the classical models. It is one of the motivations of this work to address these questions and perform the first exploration of this promising phase diagram using a bosonic decomposition of the spin operator.

4.1.2 A Schwinger boson study

Let us now focus on the spin-1/2 $J_1 - J_2 - J_3$ Heisenberg model on the kagome lattice:

$$\mathcal{H} = J_1 \sum_{\langle i,j \rangle} \hat{\mathbf{S}}_i \cdot \hat{\mathbf{S}}_j + J_2 \sum_{\langle\langle i,j \rangle\rangle} \hat{\mathbf{S}}_i \cdot \hat{\mathbf{S}}_j + J_3 \sum_{\langle\langle\langle i,j \rangle\rangle\rangle} \hat{\mathbf{S}}_i \cdot \hat{\mathbf{S}}_j \tag{4.6}$$

We set $J_1 = 1$ and fix $J_2 = J_3 = J$ to stay coherent with previous studies [113, 114, 122]. Much like the work regarding the square-kagome lattice in chapter 3, we apply the self-consistent SBMFT procedure with the Hamiltonian 4.6 and compute its full phase diagram. To do so, we considered a unit cell of $n_u = 6$ sites, as shown in figure 4.5, which is equivalent to the duplication of the traditional unit cell of $n_u = 3$ (*i.e.* one triangle).

Such a unit cell corresponds to *Ansätze* composed of 6 Lagrange multipliers as well as 72 mean-field parameters. On figure 4.5, only the 12 nearest-neighbor bonds are represented. The 24 remaining bonds for the J_2 and J_3 couplings are given in appendix C.1. Aside from random initial *Ansätze*, we focused mainly on five initial *Ansätze* corresponding to potential physical ground states on the kagome lattice. These *Ansätze* are described in detail in the next section.

4.2 Description of the initial *Ansätze*

Before revealing the phase diagram of this model, let us first describe the potential ground state candidates and their associated *Ansätze*. We will focus on the values of the nearest-neighbor A_{ij} parameters to discriminate and describe the different *Ansätze*.

[1] In [114], the half moons are rather revealed at zero-energy because the dispersive band becomes the ground state of the model for $J > 1/5$.

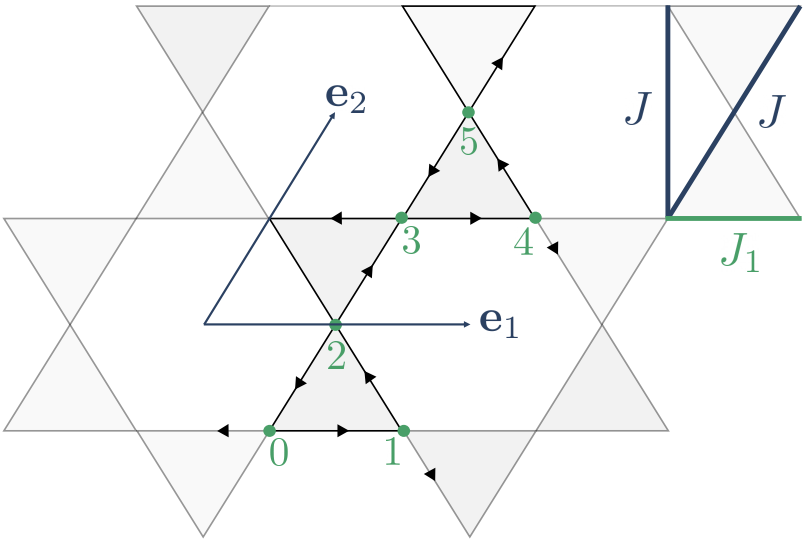

Figure 4.5: $n_u = 6$ unit cell on the kagome lattice equivalent to a doubled traditional unit cell of $n_u = 3$. An *Ansatz* on this unit cell is composed of 6 Lagrange multipliers as well as 72 mean-field parameters. Each oriented bond corresponds to two mean-field parameters A_{ij} and B_{ij}. Only the nearest-neighbor bonds are represented here. $\mathbf{e}_1$ and $\mathbf{e}_2$ are the translation vectors.

4.2.1 The $\mathbf{Q} = 0$ *Ansatz*

The first *Ansatz* is associated to the $\mathbf{Q} = 0$ state on the kagome lattice. It was described in the large-N study of Sachdev [81] on the kagome Heisenberg antiferromagnet. As seen in section 1.2.2, the $\mathbf{Q} = 0$ label comes from the fact that the associated magnetic order is described by the traditional $n_u = 3$ unit cell on the kagome lattice. This long-range order is represented on figure 4.6 (left).

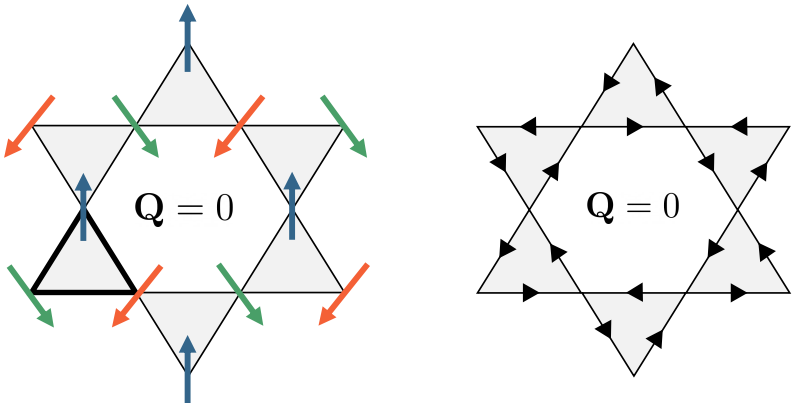

Figure 4.6: Spin configuration of the $\mathbf{Q} = 0$ long-range magnetic order (left). The magnetic unit cell (bold triangle) is composed of 3 sites where the angle between each pair of spin is 120°. Signs of the A_{ij} parameters for the $\mathbf{Q} = 0$ *Ansatz* (right). Each oriented bond corresponds to a positive value of the associated A_{ij}.

In the Schwinger boson formalism, however, the $\mathbf{Q} = 0$ magnetic order can become gapped for low enough values of the spin length. In either case, the *Ansatz* describing such a state corresponds to a set of uniform nearest-neighbor mean-field parameters on all the bonds of the $n_u = 6$ unit cell. That is, all $|A_{ij}| = \mathcal{A}$ and all $|B_{ij}| = \mathcal{B}$. The sign of the A_{ij} parameters are represented in figure 4.6 (right).

4.2.2 The $\sqrt{3} \times \sqrt{3}$ *Ansatz*

The second *Ansatz* corresponds to the $\sqrt{3} \times \sqrt{3}$ phase also described in reference [81]. As seen in section 1.2.2, the associated long-range order is described by a magnetic unit cell of 9 sites which is depicted in figure 4.7 (left).

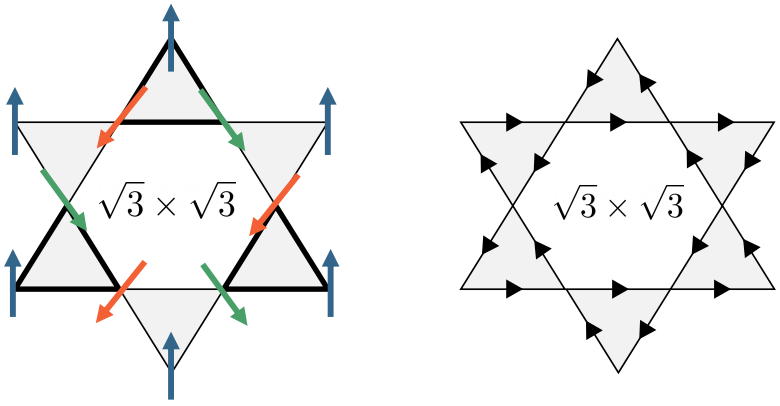

Figure 4.7: Spin configuration of the $\sqrt{3} \times \sqrt{3}$ long-range magnetic order (left). The magnetic unit cell (bold triangles) is composed of 9 sites. The angle between two nearest-neighbor spins is still 120°. Signs of the A_{ij} parameters for the $\sqrt{3} \times \sqrt{3}$ *Ansatz* (right). Each oriented bond corresponds to a positive value of the associated A_{ij}.

Similarly to the $\mathbf{Q} = 0$ state, both the A_{ij} and B_{ij} mean-field parameters are uniform for the $\sqrt{3} \times \sqrt{3}$ *Ansatz* and the signs of the A_{ij} parameters are represented on figure 4.7 (right). This *Ansatz* can of course yield either a long-range magnetic order or a disordered phase depending on the length of the spin. We note that in the Schwinger boson framework, the $\mathbf{Q} = 0$ and $\sqrt{3} \times \sqrt{3}$ *Ansätze* are both compatible with the simple $n_u = 3$ unit cell, which is not the case for the following *Ansätze*.

4.2.3 The *0H1R* and *1H1R Ansätze*

The next two *Ansätze* have been previously introduced in a projective symmetry group approach on the breathing kagome lattice [124]. Once again, they exhibit real and uniform values for both the A_{ij} and B_{ij} mean-field parameters but they need a unit cell of a least $n_u = 6$ to be correctly described. They are further characterized by fluxes associated to two kinds of local Wilson loops, that are represented on figures 4.8 and 4.9 alongside the signs of the A_{ij} parameters. The Wilson loop taken into consideration here are of the form of equation 2.55, that is, composed only of $\hat{A}_{ij}$ operators.

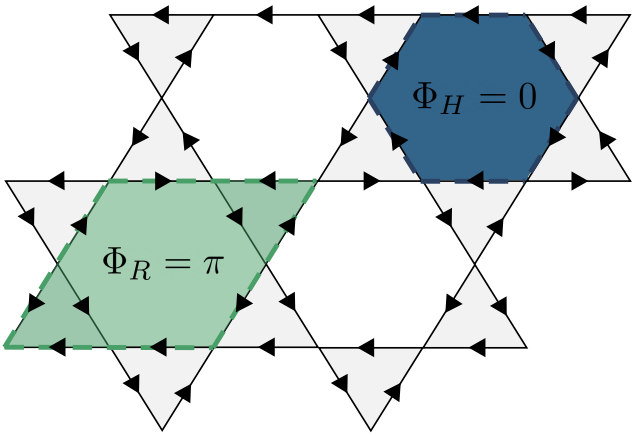

Figure 4.8: Signs of the A_{ij} parameters for the *0H1R Ansatz*. Each oriented bond corresponds to a positive value of the associated A_{ij}. This *Ansatz* is characterized by the local Wilson loop fluxes around its hexagons and rhombi. The flux associated to the hexagonal Wilson loop (in blue) is $\Phi_H = 0$ while the flux associated to the rhombus' Wilson loop (in green) is $\Phi_R = \pi$.

First, we note Φ_H the flux associated to the Wilson loops going around an hexagon of the kagome lattice. Second, we note Φ_R the flux associated to the Wilson loops going around a rhombus. The two states mentioned in [124] correspond to values of (Φ_H, Φ_R) of $(0, \pi)$ (see figure 4.8) and (π, π) (see figure 4.9). These two states were thus labelled [0Hex, πRhom] and [πHex, πRhom] but for simpler notation we will call them *0H1R* and *1H1R* for the rest of this chapter.

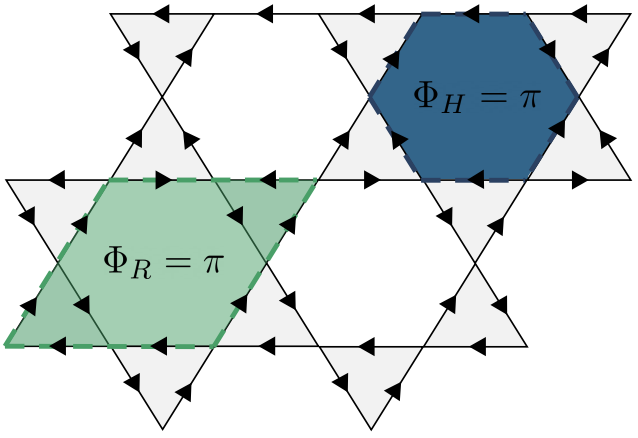

Figure 4.9: Signs of the A_{ij} parameters for the *1H1R Ansatz*. Each oriented bond corresponds to a positive value of the associated A_{ij}. This *Ansatz* is also characterized by the local Wilson loop fluxes with $\Phi_H = \pi$ for the hexagons (in blue) and $\Phi_R = \pi$ for the rhombi (in green).

As for the $\mathbf{Q} = 0$ and $\sqrt{3} \times \sqrt{3}$ *Ansätze*, it is also possible to define the same fluxes Φ_H and Φ_R. For the $\mathbf{Q} = 0$ *Ansatz* we have $(\Phi_H, \Phi_R) = (\pi, 0)$ while for the $\sqrt{3} \times \sqrt{3}$ *Ansatz* we have $(\Phi_H, \Phi_R) = (0, 0)$.

4.2.4 The *cuboc1 Ansatz*

The *cuboc1* state is a chiral spin liquid found to be the SBMFT ground state of the kagome Heisenberg antiferromagnet by Messio *et al.* [32]. Classically, this state corresponds to a long-range order defined on a unit cell composed of 12 sublattices where the 12 different spin orientations form a cuboctahedron.

In SBMFT, the *cuboc1 Ansatz* is described on the $n_u = 6$ unit cell. The chiral nature of this phase implies that some of the mean-field parameters composing the *Ansatz* are complex. This is the case for the nearest-neighbor A_{ij} parameters on one type of triangles (either up or down) while the others are real. This is represented on figure 4.10, where on the up triangles all A_{ij} parameters are complex and uniform up to a minus sign, that is $A_{ij} = \pm\mathcal{A}e^{i\theta_\triangle}$. On the down triangles all A_{ij} are strictly real. They are also uniform up to a minus sign, as represented by the oriented bonds of figure 4.10. Finally, in the *cuboc1 Ansatz* the nearest-neighbor B_{ij} parameters are uniform up to a minus sign and also real. Note that this *Ansatz* cannot be described on the traditional $n_u = 3$ kagome unit cell either.

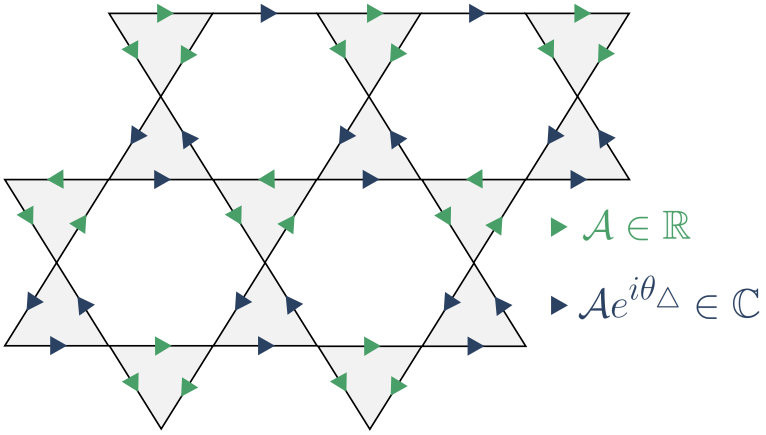

Figure 4.10: Signs of the A_{ij} parameters for the *cuboc1 Ansatz*. Each oriented bond corresponds to a positive value of the associated A_{ij}. Their are two kind of A_{ij} parameters in this *Ansatz*. On the up triangle we have complex values, uniform up to a minus sign, and equal to $\pm\mathcal{A}e^{i\theta_\triangle}$ (in blue). While the A_{ij} parameters on the down triangles are strictly real, also uniform up to a minus sign, and equal to $\pm\mathcal{A}$ (in green).

Computing the fluxes Φ_H and Φ_R for the *cuboc1 Ansatz* yields a value of $\Phi_H = 3\theta_\triangle$ as well as $\Phi_R = \pi$. If all A_{ij} were strictly real, *i.e.* $\theta_\triangle$ equals 0 or π, their fluxes would then be either $(0, \pi)$ or (π, π). This means that the sign structure of the *cuboc1 Ansatz* on the kagome lattice is actually very close from the sign structures of the *0H1R* and *1H1R Ansätze*.

4.2.5 Other *Ansätze*

Finally, we also tested the convergence of two other chiral spin liquids, the *cuboc2* and the *octahedral* states. They were described in a projective symmetry group study adapted to chiral states on the kagome lattice [88] and their dynamical structure factors were also studied in the work of Halimeh *et al.* [95]. However, it is worth noticing that we were not able to achieve convergence for either of the two corresponding *Ansätze* in our $J_1 - J_2 - J_3$ SBMFT study. Out of the 5 remaining *Ansätze*, we will see that three of them will become the ground states of our model for different values of J.

4.3 SBMFT phase diagram

Apart from the last two *Ansätze* presented above, the five others were able to converge in extended regions of the phase diagram. We have represented the energy landscape on a large portion of the $J > 0$ region in figure 4.11 for a system of linear size $l = 18$. Keeping the energy of the $\mathbf{Q} = 0$ *Ansatz* as a reference, we plot all energies in the form $E - E_{\mathbf{Q}=0}$ as a function of J. It is then straightforward to see three different regions emerge in the phase diagram where $E - E_{\mathbf{Q}=0} \leq 0$.

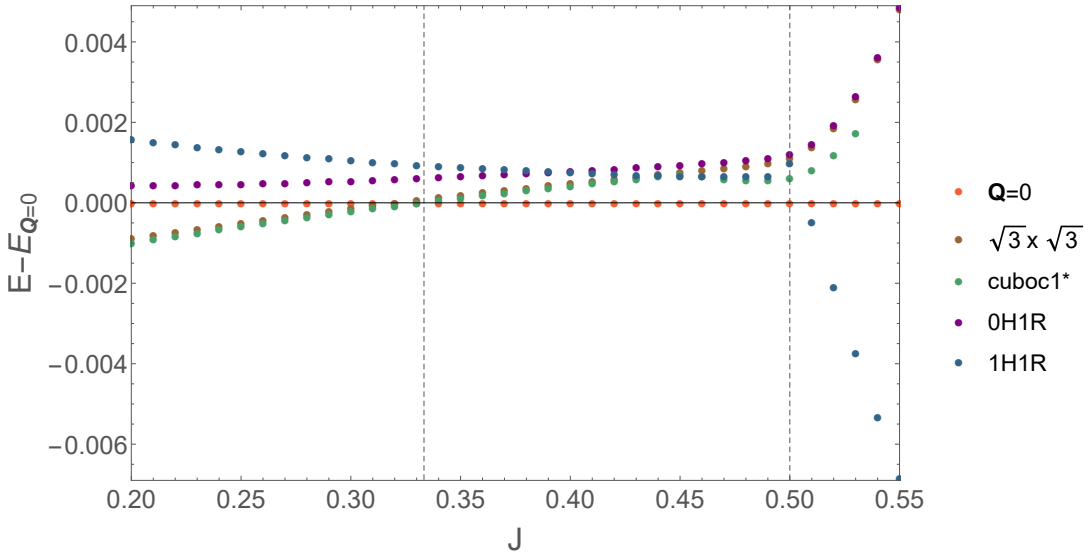

Figure 4.11: SBMFT energy landscape for a kagome system of linear size $l = 18$. The energy $E - E_{\mathbf{Q}=0}$ is plotted as a function of J where E is the energy of each converged state and $E_{\mathbf{Q}=0}$ is taken as a reference. The three regions of the phase diagram are determined by the condition $E - E_{\mathbf{Q}=0} \leq 0$. The first one corresponds to the *cuboc1** chiral spin-liquid state, the second one to the $\mathbf{Q} = 0$ spin liquid and the third one to the chiral *1H1R* order.

Studying the energy landscape of the model for larger system sizes, we were able to find three distinct ground states in the whole $J > 0$ region. The phase diagram is thus composed of a chiral spin liquid stemming from the *cuboc1 Ansatz*, a symmetric spin

liquid stemming from the $\mathbf{Q} = 0$ *Ansatz* and a chiral long-range order stemming from the *1H1R Ansatz*. We will describe in detail each of the three ground states in the next sections.

4.3.1 The *cuboc1** chiral spin liquid

The chiral *cuboc1* ground state of the nearest neighbor Heisenberg kagome model [32] persists over a finite range of parameters $0 < J < 1/3$, albeit slightly deformed. We will thus call it *cuboc1** from now on.

In the converged *Ansatz* of the *cuboc1** ground state, the nearest-neighbor A_{ij} parameters on the up triangles are complex as expected. But surprisingly on the down triangles, the nearest-neighbor A_{ij} parameters are not strictly real anymore, but have a phase $\theta_\triangledown$ close but not equal to 0 or π such that $A_{ij} = \pm\mathcal{A}e^{i\theta_\triangledown}$.

The nearest-neighbor B_{ij} parameters remain strictly real in the $0 < J < 1/3$ region. In turn, the mean-field parameters corresponding to the J_2 and J_3 couplings are complex but are one or two orders of magnitude smaller in amplitude than the nearest-neighbor parameters.

This *cuboc1** ground state exhibits values of (Φ_H, Φ_R) equal to $(3\theta_\triangle - 3\theta_\triangledown, \pi)$. The complex values of the nearest-neighbor A_{ij} parameters as well as the value of the fluxes Φ_H and Φ_R confirms the chirality of the *cuboc1** ground state.

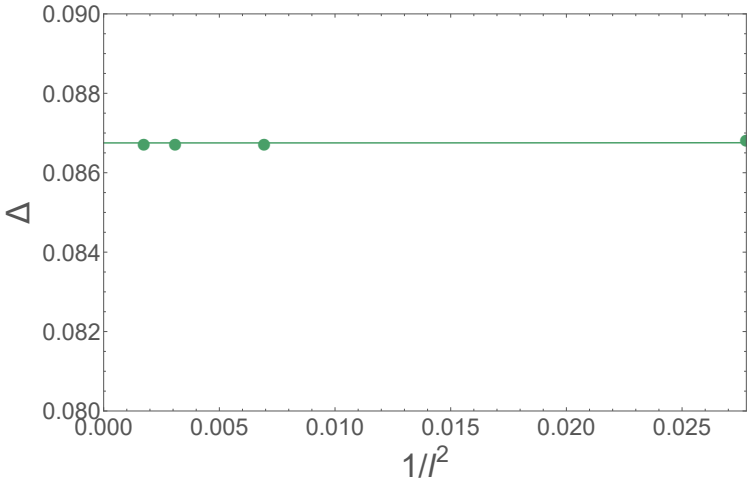

Figure 4.12: Finite size study of the energy gap Δ in the *cuboc1** ground state for $J = 0.2$ and system sizes up to $l = 24$. The gap remains open in the thermodynamic limit with $\Delta = 0.08675$.

Another characteristic of this phase is its gapped nature that we have confirmed through finite size studies. In figure 4.12, we have represented the finite size scaling of the energy gap at the point $J = 0.2$. The energy gap converges rapidly, the difference between the gap values at $l = 18$ and $l = 24$ being of order 10^{-11}. This means that the gap remains

open in the thermodynamic limit with a value of $\Delta = 0.08675$ at $J_2 = 0.2$. We have checked that the *cuboc1** ground state remains gapped in the whole $0 < J < 1/3$ region.

For $J > 1/3$, the *cuboc1** phase is no longer the ground state but can still achieve convergence through the self-consistent procedure to become an excited state of the model. A modification of the associated *Ansatz* occurs for $J > 0.45$, since the nearest-neighbor B_{ij} parameters become complex. In the meantime, the nearest-neighbor A_{ij} parameters remain complex but with the condition $\theta_{\triangle} = \theta_{\triangledown}$ on all bonds. This also has for effect to change (Φ_H, Φ_R) to (π, π).

4.3.2 The $\mathbf{Q} = 0$ spin liquid

For $1/3 < J < 1/2$, the ground state of the model was obtained starting from the $\mathbf{Q} = 0$ *Ansatz* described in section 4.2.1. It exhibits the same characteristics for the nearest-neighbor A_{ij} and B_{ij} parameters. The sign structure is the same as in figure 4.6 (right) and we also have $(\Phi_H, \Phi_R) = (\pi, 0)$. The nearest-neighbor parameters are the strongest in amplitude with the A_{ij} and B_{ij} parameters associated to the J_2 and J_3 couplings being at least one order of magnitude smaller and strictly real. More precisely, the A_{ij} parameters on the J_3 bonds are strictly zero for this ground state.

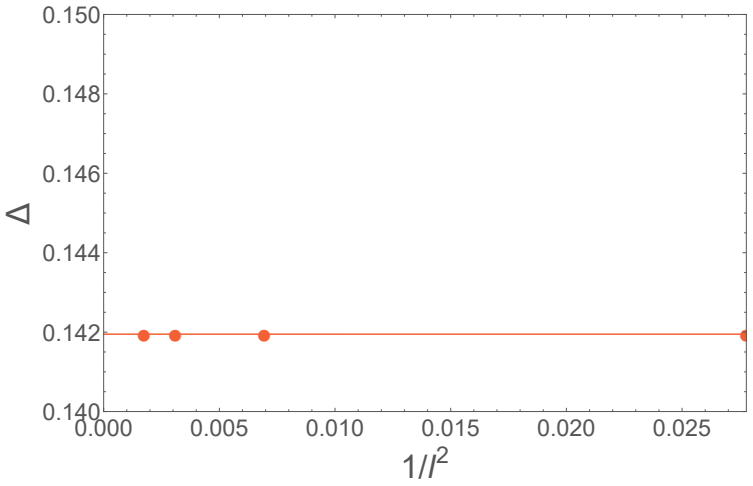

Figure 4.13: Finite size study of the energy gap Δ in the $\mathbf{Q} = 0$ ground state for $J = 0.45$ and system sizes up to $l = 24$. The gap remains open in the thermodynamic limit with $\Delta = 0.14195$.

As for the previous ground state, we have performed several finite size studies to determine the energy gap in the thermodynamic limit. In this $\mathbf{Q} = 0$ phase we found that the gap also remains open on the whole $1/3 < J < 1/2$ region. We provide such a finite size study at the $J = 0.45$ point in figure 4.13. Once again, convergence was reached rapidly yielding a non-zero value of $\Delta = 0.14195$ for system sizes of $l = 18$ and larger. In other words, the ground state in this region corresponds to the disordered version of

the $\mathbf{Q} = 0$ state with a small perturbative contribution from the J_2 and J_3 mean-field parameters.

Finite size studies were also performed to determine the precise location of the boundary between the *cuboc1** and the $\mathbf{Q} = 0$ ground states. Both the energies of the *cuboc1** and $\mathbf{Q} = 0$ states are represented as a function of J in figure 4.14 for a system size of $l = 18$. The boundary is located around $J = 0.33$ where the difference of energy is only of $\approx 10^{-6}$. We have checked the location of the boundary for larger system sizes, up to $l = 36$. The same behavior occurs for all larger system sizes so that the boundary is always located at $J = 0.33$. Using thinner J steps, our results were consistent with a boundary at $J = 1/3$.

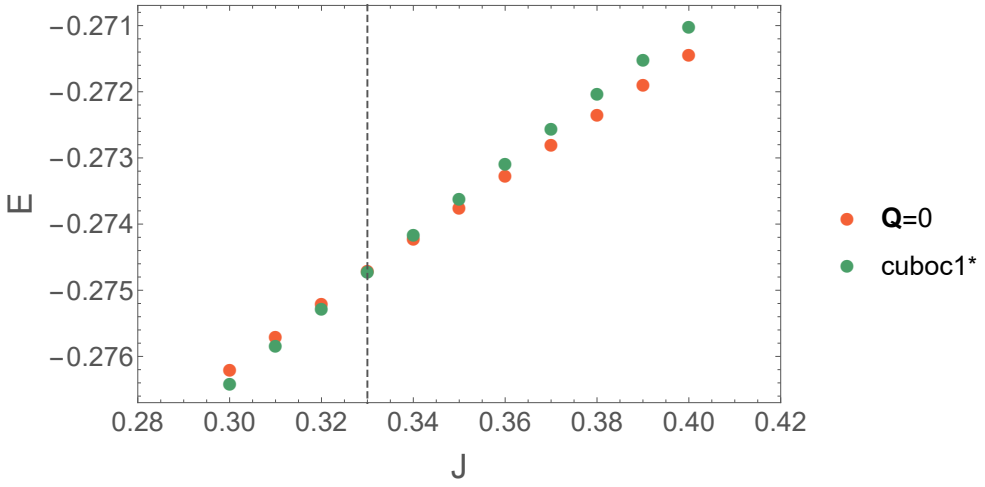

Figure 4.14: Location of the boundary between the *cuboc1** and $\mathbf{Q} = 0$ ground states for a system of linear size $l = 18$. The same behavior occurs for larger system sizes so that the the boundary is always located at the $J = 0.33$ point.

For $J > 1/2$, our SBMFT self-consistent procedure shows a conspicuous hysteresis for the $Q = 0$ phase that stabilizes two different states depending on whether we increase or decrease J. These two states correspond to the regular $\mathbf{Q} = 0$ spin liquid presented above and to a new chiral and $\mathbf{Q} = 0$ disordered state that we describe in this section. In figure 4.15, we have displayed the energies of both the regular (in orange) and chiral (in green) $\mathbf{Q} = 0$ states as a function of J.

Starting from low values of J and from an initial $\mathbf{Q} = 0$ *Ansatz*, we apply the self-consistent procedure by incrementing J by steps of 0.01. Plugging at each step the previous converged *Ansatz* as initial condition our algorithm yields the regular $\mathbf{Q} = 0$ spin liquid up to $J = 0.58$. For $J > 0.58$, the result of our self-consistent procedure changes and corresponds to the chiral $\mathbf{Q} = 0$ state. The *Ansatz* corresponding to this new state is rather similar to the regular $\mathbf{Q} = 0$ *Ansatz*. It shows the same structure for the nearest-neighbor A_{ij} parameters but complex nearest-neighbor B_{ij} parameters.

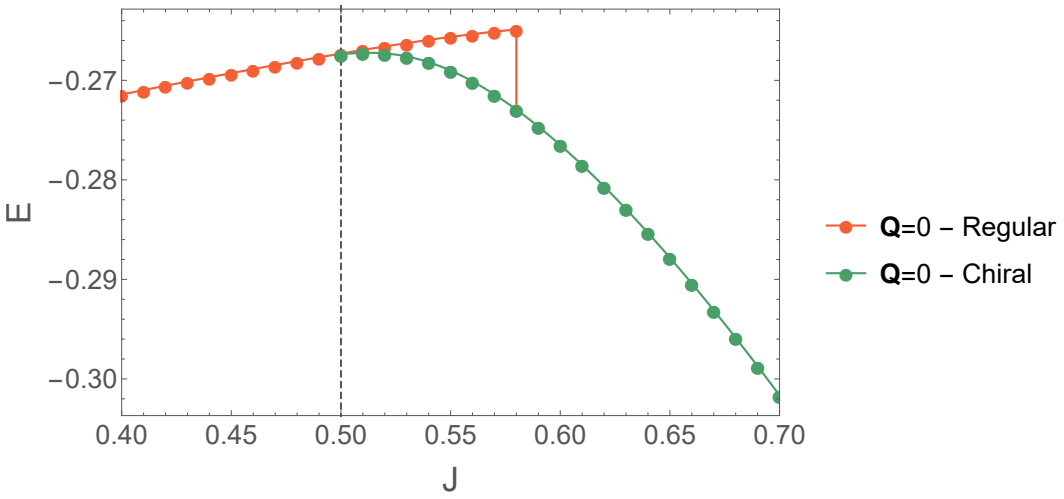

Figure 4.15: Energy of the regular (in orange) and chiral (in green) $\mathbf{Q} = 0$ states. Starting from low values of J, the self-consistent procedure yields the regular $\mathbf{Q} = 0$ state up to $J = 0.58$. After this point, our algorithm yields the chiral $\mathbf{Q} = 0$ state. Starting from high values of J, the chiral $\mathbf{Q} = 0$ state is stabilized by the self-consistent procedure up to $J = 0.5$ where its energy connects to the energy of the regular $\mathbf{Q} = 0$ state.

The A_{ij} (resp. B_{ij}) parameters associated with J_2 are complex (resp. strictly real) and all parameters associated with the J_3 bonds are complex and non-zero.

Then, starting from an initial $\mathbf{Q} = 0$ *Ansatz* at larger values of J and progressively decrementing J by steps of 0.01, the self-consistent procedure converges to the chiral $\mathbf{Q} = 0$ state up to $J = 0.5$. For $J < 0.5$, the self-consistent procedure yields a converged *Ansatz* corresponding to the regular $\mathbf{Q} = 0$ spin-liquid ground state. We note that the evolution of the energy of the chiral $\mathbf{Q} = 0$ state in figure 4.15 is smooth and connects continuously to the energy of the $\mathbf{Q} = 0$ ground state at $J = 1/2$.

The hysteresis analysis of the $\mathbf{Q} = 0$ phase is a key step to pinpoint the location of the boundary with the ground state presented in the next section.

4.3.3 The chiral *1H1R* order

The third ground state of this phase diagram is stable in the region $J > 1/2$. It is a long-range order stemming from the initial *1H1R Ansatz* described earlier in section 4.2.3.

As in section 4.3.2, we have to make the distinction betweeen two possible states stemming from the initial *1H1R Ansatz*. We first have a disordered version of the *1H1R* state with a finite gap and the same sign structure for the nearest-neighbor A_{ij} parameters as in figure 4.9. The mean-field parameters associated to the J_2 and J_3 bonds are at least one order of magnitude smaller in amplitude and are all strictly real. We will thus

refer to this phase as the disordered *1H1R* state.

Second, we have the possibility to stabilize a modified version of this *Ansatz*, once again for $J \geq 1/2$. The modified *Ansatz* has a similar sign structure as in figure 4.9 but with complex nearest-neighbor A_{ij} parameters. However, the relation $(\Phi_H, \Phi_R) = (\pi, \pi)$ is still verified and we have on nearest-neighbor bonds $A_{ij} = \pm\mathcal{A}e^{i\theta}$ with θ being very close from 0 or π. Additionally, every other mean-field parameters, including the nearest-neighbor B_{ij}, become complex. Finally, this phase is gapless, as can be seen on figure 4.16 where we performed a finite-size study of the energy gap at $J = 0.6$. Due to convergence issues for system sizes over $l = 24$, we performed a non-linear extrapolation which is consistent with a gapless phase within error bars of the order of 5.10^{-5} on the energy gap. We will thus refer to this phase as the chiral *1H1R* order.

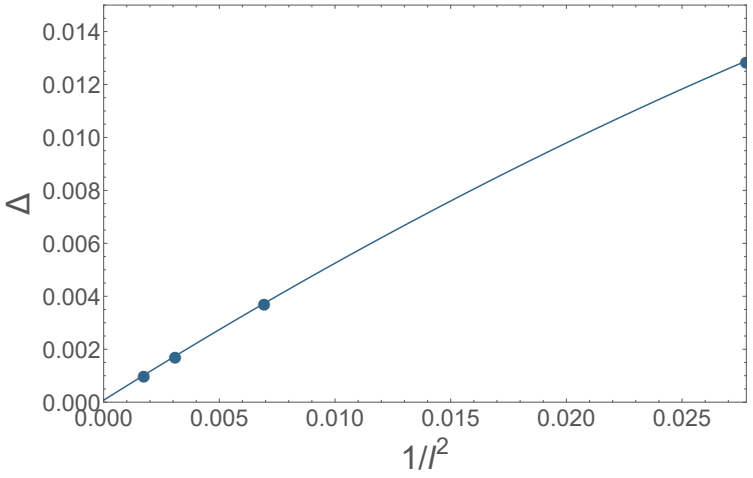

Figure 4.16: Finite size study of the energy gap Δ in the *1H1R* ground state for $J = 0.6$ and system sizes up to $l = 24$. Convergence issues arise for $l > 24$ but a non-linear extrapolation confirms the gapless nature of this phase within error bars of the order of 5.10^{-5}.

We have represented the energy of both the disordered *1H1R* phase (in blue) and the chiral *1H1R* order (in green) around the $J = 1/2$ point on figure 4.17. Starting from low values of J, the initial *1H1R Ansatz* converges to yield the disordered version of the *1H1R* state up to $J = 0.56$. For $J \geq 0.57$, however, the state obtained after the self-consistent procedure changes into the chiral *1H1R* order. Then, going from higher to lower values of J, we reach convergence for the chiral *1H1R* order up to $J = 1/2$. For $J < 1/2$, the self-consistent procedure yields once again the disordered version of the *1H1R* state. In conclusion, we have a similar hysteresis process as for the $\mathbf{Q} = 0$ states, in the same region $J \geq 1/2$.

Now that we have made the distinction between these two *1H1R* states, we want to locate the boundary with the $\mathbf{Q} = 0$ ground state. To do so, we have plotted on figure

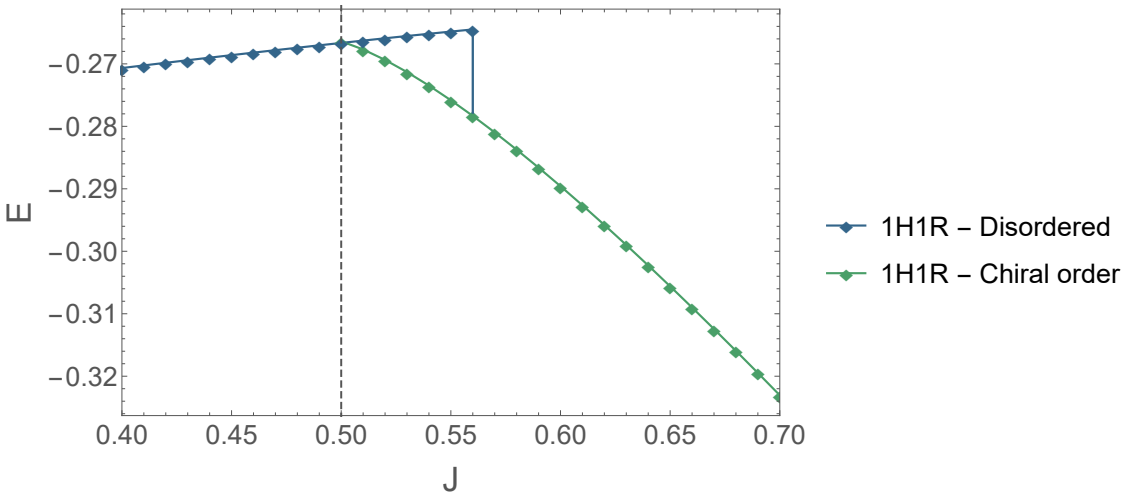

Figure 4.17: Energy of the disordered (in blue) and chiral ordered (in green) *1H1R* states. Starting from low values of J, the self-consistent procedure yields the disordered *1H1R* state up to $J = 0.58$. After this point, our algorithm yields the chiral *1H1R* order. Starting from high values of J, the chiral *1H1R* order is stabilized by the self-consistent procedure up to $J = 0.5$.

4.18 the energy of the regular $\mathbf{Q} = 0$ state (orange circles), the chiral $\mathbf{Q} = 0$ state (green circles) as well as the disordered *1H1R* state (blue diamonds) and the chiral *1H1R* order (green diamonds) for a system of linear size $l = 18$. For this system size, the boundary is located between the $J = 0.5$ and $J = 0.51$ points and the ground state for $J > 1/2$ corresponds to the chiral *1H1R* order. For system sizes over $l = 24$ convergence issues arise for the *1H1R* order. Further studies would be required to check if the boundary shifts exactly to $J = 1/2$ in the thermodynamic limit. Still, the ground state of our model in the region $J > 1/2$ is a chiral long-range order reminiscent of the *1H1R* state, with $(\Phi_H, \Phi_R) = (\pi, \pi)$.

In conclusion, we have described the region of stability and the associated *Ansätze* of the three ground states composing the phase diagram of our $J_1 - J_2 - J_3$ model on the kagome lattice. In the next section, we will provide further characterization of these ground states by computing their experimental signatures in the form of dynamical and static structure factors.

4.4 Experimental signatures of the ground states

4.4.1 Dynamical structure factors

As further characterization of our ground states and keeping in mind a potential connection with experiments, we provide examples of dynamical structure factors for each of the three ground states.

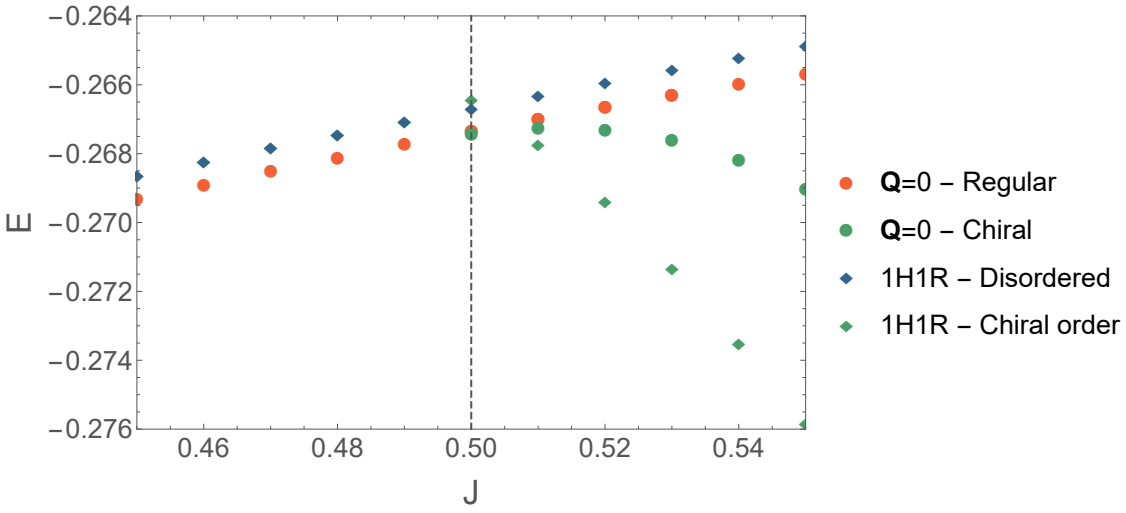

Figure 4.18: Location of the boundary between the $\mathbf{Q} = 0$ states and the *1H1R* states for a system of linear size $l = 18$. The energy of the regular $\mathbf{Q} = 0$ state is represented by the orange circles, the energy of the chiral $\mathbf{Q} = 0$ state by green circles while the energies of the disordered and chiral ordered *1H1R* states are represented by blue and green diamonds respectively. Convergence issues for the *1H1R* phase for $l \geq 24$ prevent a precise size study of the location of the boundary. However, for all size below $l = 24$ the boundary is located between $J = 0.5$ and $J = 0.51$.

To represent these dynamical structure factors, we used a path connecting high-symmetry points of the first Brillouin zone of the kagome lattice. Two such paths, connected by a $\pi/2$ rotation are depicted in figure 4.19. Since we have not found any nematic ground state in our $J_1 - J_2 - J_3$ model, the dynamical structure factors represented on either of these two paths will be equivalent. For all dynamical structure factors below, we will use the green $\Gamma \to Y \to M \to \Gamma$ path of figure 4.19. Since we work with unit cells of $n_u = 6$ sites, the corresponding first Brillouin zone will be rectangular unlike the hexagonal Brillouin zone associated with the traditional $n_u = 3$ unit cells.

We provide dynamical structure factors for each of the three ground states. At the point $J = 0.2$ for the *cuboc1** ground state in figure 4.20, at $J = 0.4$ for the $\mathbf{Q} = 0$ ground state in figure 4.21 and at $J = 0.8$ for the *1H1R* ground state in figure 4.22.

The dynamical structure factors of the *cuboc1** and $\mathbf{Q} = 0$ ground states are clearly gapped and can be distinguished quite easily. In figure 4.20, spectral weight is going down at the M and Γ points, while in figure 4.21, spectral weight is only going down at the Γ point as expected for the $\mathbf{Q} = 0$ state. The dynamical structure factor of the *1H1R* state at $J = 0.8$ is clearly gapless and only shows spectral weight near the M and Γ points for $\omega \simeq 0$.

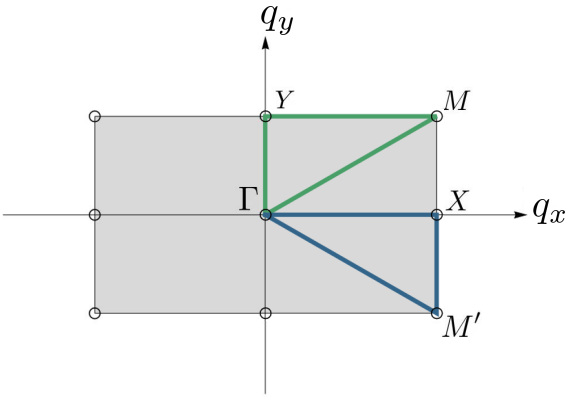

Figure 4.19: Two paths connecting high-symmetry points in the first Brillouin zone of the kagome lattice with $n_u = 6$ unit cells. The green and blue paths will lead to equivalent dynamical structure factors since we have not found any nematic ground states. We will use the green $\Gamma \to Y \to M \to \Gamma$ path to represent all following dynamical structure factors.

4.4.2 Static structure factors

We described static structure factors and their expression in the SBMFT formalism in section 2.4.3. The computation using the coefficient of the transformation matrix $T_{\mathbf{k}}$ only gives us information about the spin correlations in the first Brillouin zone. To gain information about these correlations outside the first Brillouin zone, we need to account for correlations between spins belonging to different sublattices of the same unit cell. A way to do so, is to first compute the spin correlations in real space, where the position of each spin inside its unit cell is already taken into account. Starting from a spin of reference, we compute all values of $\langle \hat{\mathbf{S}}^{\alpha}_{\text{ref}} \cdot \hat{\mathbf{S}}^{\beta}_{j} \rangle$ for all unit cells j of the system and all sublattices α and β. Once they are computed, it is possible to get back the static structure factor simply by taking the Fourier transform of these correlations in real space:

$$S^{\alpha,\beta}(\mathbf{q}) = \sum_{j=1}^{n_c} e^{i\mathbf{q}\cdot(\mathbf{r}_\alpha - \mathbf{R}_j - \mathbf{r}_\beta)} \langle \hat{\mathbf{S}}^{\alpha}_{\text{ref}} \cdot \hat{\mathbf{S}}^{\beta}_{j} \rangle \tag{4.7}$$

where $\mathbf{r}_\alpha$ (resp. $\mathbf{r}_\beta$) is the position of the sublattice α (resp. β) inside a unit cell and n_c the number of unit cells in the system.

We then have acces to information on the correlations beyond the first Brillouin zone by plotting the static structure factor 4.7 for any wave-vector $\mathbf{q}$. Static structure factors are represented for each one of the three ground states of our model in figures 4.23, 4.24 and 4.25. In each one of these static structure factors, we have represented several Brillouin zones corresponding to different unit cells in real space. The rectangular Brillouin zone in yellow corresponds to the $n_u = 6$ unit cell of the kagome lattice while the smaller green hexagonal Brillouin zone corresponds to the $n_u = 3$ unit cell of the kagome lattice.

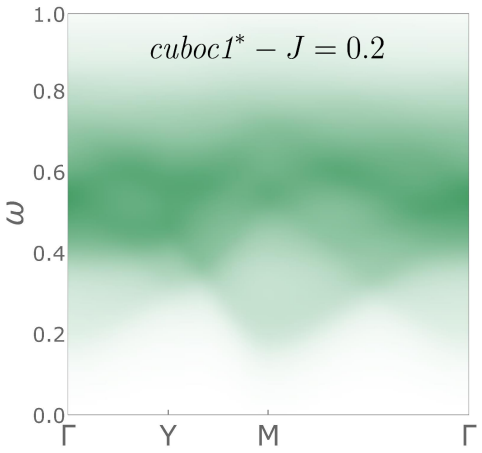

Figure 4.20: Dynamical structure factor of the *cuboc1** ground state at $J = 0.2$. The maximum of $S(\mathbf{q}, \omega)$ is set to unity.

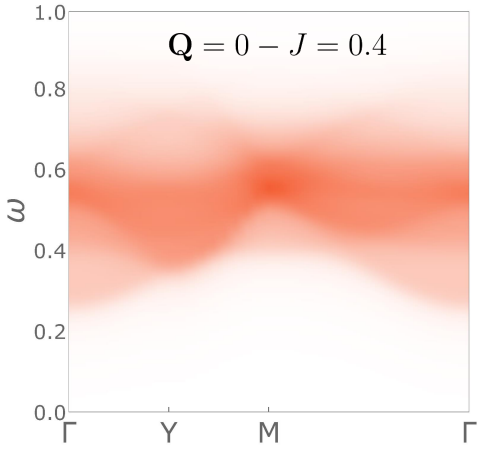

Figure 4.21: Dynamical structure factor of the the $\mathbf{Q} = 0$ ground state at $J = 0.4$. The maximum of $S(\mathbf{q}, \omega)$ is set to unity.

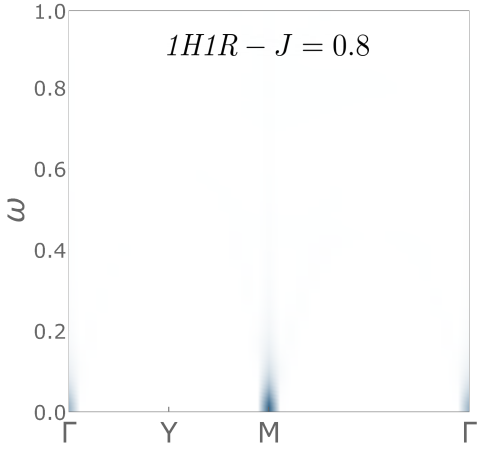

Figure 4.22: Dynamical structure factor of the the *1H1R* ground state at $J = 0.8$. The maximum of $S(\mathbf{q}, \omega)$ is set to unity.

Finally, the larger red hexagon corresponds to the Brillouin zone of the triangular lattice, indicated here as a reference. The maximum of each static structure factor has been set to unity.

The static structure factors of figures 4.23 and 4.24 are both representative of disordered phases indicated by the absence of Bragg peaks. For the *cuboc1** ground state the maximum of intensity is located on a broad region around the corners of the Brillouin zone of the triangular lattice (in red), while for the $\mathbf{Q} = 0$ ground state, the maximum of intensity is located around the middle of the edges of the same Brillouin zone.

However, the static structure factor of the *1H1R* ground state exhibits different features. The maxima of intensity are located on single ordering wave-vectors corresponding to Bragg peaks, which are expected for such a long-range order. These maxima are much larger in intensity than for the *cuboc1** and $\mathbf{Q} = 0$ disordered phases, even if it cannot be verified on figures 4.23 through 4.25 because all maxima are set to unity.

As an additional result, we provide a brief study of the stability of our ground states against quantum fluctuations by varying the spin length S in appendix C.2. The final result section of this chapter will focus on connecting with previous studies, both classical and quantum.

4.5 Connection to previous work

Looking back at the previous classical studies, we see that the point $J = 1/2$ plays a particular role in the Heisenberg Hamiltonian of equation 4.5. Indeed, having a non-zero $\mathbf{M}_p$ on each triangle p becomes energetically favorable for $J > 1/2$ because of the $(1/2 - J)$ factor before the first term. Interestingly, the $J = 1/2$ point also plays a particular role in our quantum model. First, it is for $J > 1/2$ that hysteresis appears. The regular $\mathbf{Q} = 0$ and 1H1R phases split into two *Ansätze* each, giving rise to the additional chiral disordered $\mathbf{Q} = 0$ phase and to the chiral 1H1R long-range order. Second, the boundary separating the $\mathbf{Q} = 0$ spin-liquid ground state from the chiral *1H1R* order is located at $J = 1/2$. In the end, the spin to charge mapping of equation 4.5 may give us a classical intuition for the location of the boundary in the SBMFT phase diagram.

We will now focus on a very interesting phenomenon taking place in our SBMFT model beyond the $J = 1/2$ point. We have already seen that, for $J > 1/2$, the chiral version of the $\mathbf{Q} = 0$ state is stabilized with, for instance, complex nearest-neighbor B_{ij} parameters. This chiral version of the $\mathbf{Q} = 0$ state is an excited state of the model in the $J > 1/2$ region with the chiral *1H1R* order becoming the ground state for $J > 1/2$.

Looking at the static structure factor of the excited chiral $\mathbf{Q} = 0$ state, we surprinsingly

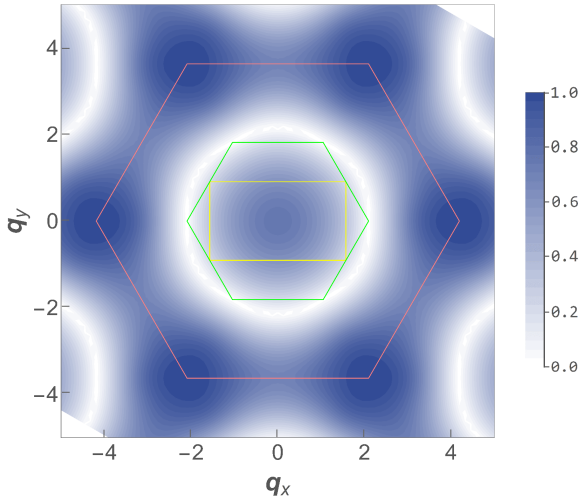

Figure 4.23: Static structure factor of the *cuboc1** ground state at $J = 0.2$.

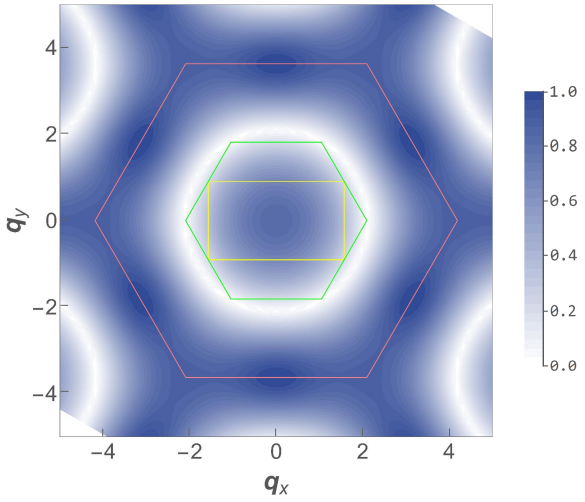

Figure 4.24: Static structure factor of the $\mathbf{Q} = \mathbf{0}$ ground state at $J = 0.4$.

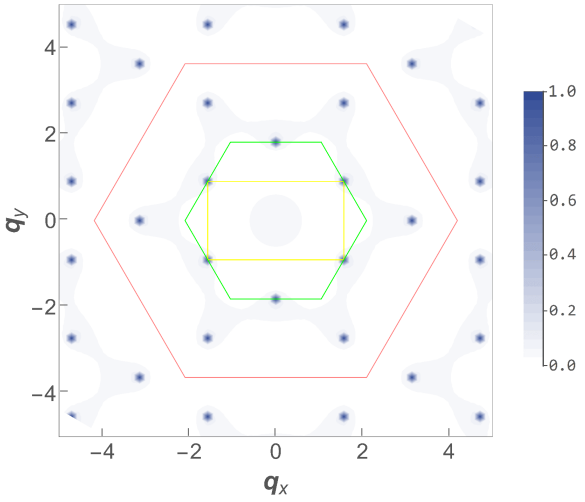

Figure 4.25: Static structure factor of the *1H1R* ground state at $J = 0.8$.

see half-moon patterns appear. The static structure factors of the chiral $\mathbf{Q} = 0$ state is represented on figure 4.26 for $J = 0.6$ where half moons have the highest amplitude and are correctly located outside the first Brillouin zone in reciprocal space.

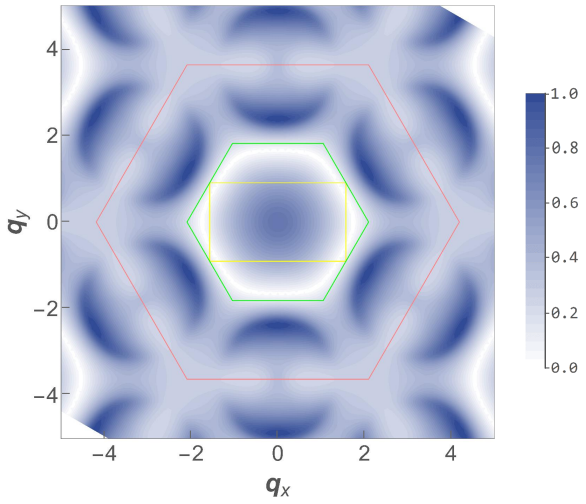

Figure 4.26: Static structure factor of the excited chiral $\mathbf{Q} = \mathbf{0}$ state at $J = 0.6$. Half moons appear outside the first Brillouin zone.

These half-moon patterns actually appear from $J \approx 0.53$ up to $J \approx 0.8$ in our SBMFT study. After that, the chiral $\mathbf{Q} = 0$ state is unable to reach convergence. The presence of these patterns in both the previous fermionic approach of Buessen *et al.* [122] and now our mean-field bosonic study suggests that half moons are an intrisic feature of the quantum $J_1 - J_2 - J_3$ model on the kagome lattice.

We emphasize that while half moons were present as the ground state in the fermionic model, we have only encountered them as an excited state for $J > 1/2$. However, we are still limited, first by the mean-field decoupling of the Schwinger boson Hamiltonian and second, because of the bosonic constraints being only respected on average. Beyond mean-field, the situation could very well change and yield the chiral $\mathbf{Q} = 0$ spin liquid and the associated half moons as the ground state of the system.

Finally, a question remains: what become of the pinch-point and star patterns in the quantum case? We first note that pinch points are present in the fermionic study of reference [122] at low J, albeit broadened. In our SBMFT study, we searched for pinch points in the structure factors of all converged states at low values of J, but could not find any. This might be understood as a preference in SBMFT for the chiral *cuboc1* state at low J.

Still, the structure factor of the *cuboc1** ground state does not show pinch points but its maximum of intensity is at the same place as for the classical systems, on the corner of the larger red Brillouin zone. On the other hand, the maximum of intensity of the

$\mathbf{Q} = 0$ ground state is at the middle of the red Brillouin zone edges. This is where pinch points are supposed to be in classical systems, and where half moons start to emerge. The shifted position of the maximum of intensity between the *cuboc1** and $\mathbf{Q} = 0$ phases is consistent with the classical picture of a dispersive band becoming flat at the centre of the red Brillouin zone edges.

Moreover, it is remarkable that the hysteresis and multiple self-consistent solutions of the convergence algorithm take place right where the half moons appear, around $J \approx 1/2$. If we apply the classical picture to the quantum problem, the fact that the dispersive band becomes the ground state below the flat band seems to completely turn the physics of the kagome antiferromagnet upside down. This qualitative change is consistent with equation 4.5 since the flat band is stabilised by the self-energy cost of magnetic fluctuations within triangles, which is not the case anymore for $J > 1/2$.

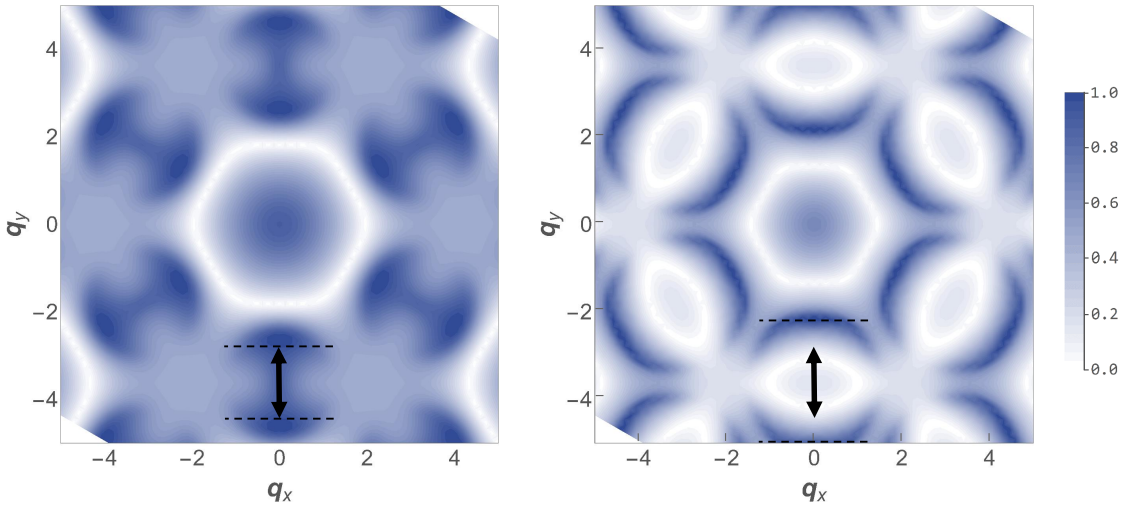

Figure 4.27: Comparison of half moon diameters for $J = 0.55$ (left) and $J = 0.75$ (right). The dashed lines represent the spatial extension of the bottom half-moon pattern. The black arrow represents the diameter of the half moons at $J = 0.55$. The diameter clearly increases going from $J = 0.55$ to $J = 0.75$.

As for the star patterns, we also did not find any such feature in our static structure factors above $J = 1/2$. However, it is interesting to monitor a simple characteristic of the half moons, connected to the formation of the star pattern. This characteristic is the diameter of the half-moon patterns. Indeed, the formation of the star pattern, classically, comes from the continuous enlargement of the half moons as J increases until their coalescence [114]. Such a behavior begins to occur in our SBMFT model since the diameter of the half moons are increasing with the values of J up to $J = 0.8$, after which convergence is lost. This is demonstrated on figure 4.27 where we have represented the static structure factors of the excited chiral $\mathbf{Q} = 0$ state at $J = 0.55$ (left) and $J = 0.75$ (right). The dashed line are a measurement of the diameter of each half moon while

the black arrow represents the diameter of the half moons at $J = 0.55$. It is then straightforward to see that, going from $J = 0.55$ to $J = 0.75$, the diameter of the half-moon pattern increases. We have verified that this increase is indeed continuous. In conclusion, the mechanism forming star patterns is present in our system, however, due to convergence issues for $J > 0.8$ we could not observe these patterns in any static structure factor.

4.6 Conclusion

In this chapter, a comprehensive study on the $J_1 - J_2 - J_3$ phase diagram of the kagome lattice was carried out in the SBMFT framework for the particular case where $J_2 = J_3$. We found three distinct ground states, a chiral spin liquid for $0 < J < 1/3$, another spin-liquid stemming from the $\mathbf{Q} = 0$ *Ansatz* for $1/3 < J < 1/2$ and finally a chiral long-range order for $J > 1/2$. The $\mathbf{Q} = 0$ state is particularly interesting on this model, since it is, firstly, a disordered ground state in an extended region of the phase diagram and, secondly, since it can become a chiral and disordered excited phase for $J > 1/2$ yielding half moons in its static structure factor. The presence of half moons in both excitations of our bosonic study and in a ground state of the fermionic approach [122] indicates that we should consider them as an intrisic feature of the quantum model. Finally, we shed light on the special $J = 1/2$ point and provided a potential connection between the classical and quantum Hamiltonians.

This theoretical study confirms the richness of the model which hosts multiple chiral states as well as many disordered states either in the form of excited states or ground states. However, we can wonder about the potential connection with experimental works, especially regarding the distinctive experimental signatures of the theoretical models that are the pinch points, half moons and star patterns. Experimentally, pinch points have notably been observed in various pyrochlore magnets [111, 125, 126]. Half moons have also been observed via inelastic neutron scattering experiments in the pyrochlore materials $Tb_2Ti_2O_7$ [127], $NaCaNi_2F_7$ [128] and in the pyrochlore oxyde $Nd_2Zr_2O_7$ in presence of a magnetic field parallel to the [111] axis [129]. They were also observed in a molecular dynamics simulation of transverse spin excitations at finite energy [130] for parameters corresponding to the kagome bilayer compound $Ca_{10}Cr_7O_{28}$ [131].

It should then be possible to observe such features on a $J_1 - J_2 - J_3$ kagome compound as well. Unfortunately, we have not yet heard of any experimental kagome compound exhibiting such couplings. However, the possibilty of having these further neighbor couplings is not out of the question. Indeed, the presence of J_2 and J_3 could easily arise via a superexchange interaction mediated by a magnetically neutral atom at the center

of the triangles of the kagome lattice. In this scenario, the case $J_2 = J_3$ would also be physically justified.

Remaining in the SBMFT formalism, a few results of this chapter could be studied in a more detailed way. First, we remind that the half-moon patterns are present in our model only as an excited state. Probing the phase diagram with $J_2 \neq J_3$ around the $J = 1/2$ point may reveal a region where the half moons actually correspond to the ground state of the system. Moreover, lifting the condition $J_2 = J_3$ may also favor the presence of the star pattern, bypassing the convergence issues of the chiral $\mathbf{Q} = 0$ state for $J > 0.8$. Second, looking back at the static structure factor of the chiral *1H1R* order at $J = 0.8$ of figure 4.25, we see a pattern of intermediate intensity right outside the first hexagonal Brillouin zone of the kagome which is oddly similar to the star pattern of the classical study [114]. The maximum of intensity remains at the Bragg peaks but a finite size study could tell us if this intermediate intensity is still present in the thermodynamic limit. The connection of this static structure factor to the star pattern has yet to be explored.

Chapter 5

Conclusion

In this manuscript, we have studied the phase diagrams of two frustrated systems via the Schwinger boson mean-field theory (SBMFT). Probing these systems, we searched for exotic magnetic states such as quantum spin liquids, exhibiting unconventional correlations, hidden orders as well as topological properties.

In chapter 1, we introduced the core concepts behind frustration and its effects on magnetic systems. First in the classical case, where frustration can lead to an extensive ground-state degeneracy, for instance on the kagome lattice. Then, we described a variety of magnetic phases frustration can give rise to. In the quantum case, we focused on valence bond crystals and different kinds of quantum spin liquids in the framework of the resonating valence bond theory. Finally, to illustrate these concepts, we described recent progress on two concrete systems: the kagome and square-kagome lattices.

In chapter 2, we described in detail the theoretical and numerical tools behind SBMFT. We first started by decomposing the Heisenberg Hamiltonian in terms of bosonic spinon operators before performing a mean-field decoupling on the bond operators $\hat{A}_{ij}$ and $\hat{B}_{ij}$. Then, we explained how to diagonalize the mean-field Hamiltonian via a Bogoliubov transformation allowing one to compute the free energy of the system. We proceeded with a description of the SBMFT algorithm by providing two ways to solve the self-consitent equations on the mean-field parameters. We also computed in the SBMFT formalism several important physical quantities needed for the characterization of the different ground states. Finally, we defined local Wilson loop operators as well as their associated gauge fluxes and showed in a simple example on the triangular lattice how they discriminate different spin-liquid states.

In chapter 3, we studied the Heisenberg J_1-J_2 model on the square-kagome lattice using SBMFT. We have computed the complete phase diagram as a function of $x = J_2/J_1$ and described the five ground states composing it. First, we described the plaquette phase as

well as the ferrimagnetic order, already studied in reference [75]. These two states are the ground states of our model for low and high values of x respectively. We then described the two incommensurate magnetic orders adjacent to the most intriguing ground state of this phase diagram: a topological nematic spin liquid exhibiting non-zero local fluxes. We deepened the description of this ground state by explicitly revealing its topological degeneracy before discussing the modification of the phase diagram beyond the mean-field approximation. Finally, we proposed connections to experimental studies on the newly synthezied square-kagome compound [6] by computing dynamic structure factors for each of the ground states and by taking into account the possibility of anisotropy between the J_2 bonds of the lattice.

In chapter 4, we carried out a study of the $J_1 - J_2 - J_3$ Heisenberg model on the kagome lattice with $J_2 = J_3 = J$, again via our Schwinger boson self-consistent procedure. We also provided a full phase diagram composed of three distinct ground states. The first one, is a chiral spin liquid stemming from the *cuboc1 Ansatz* [32] stable on the region $0 < J < 1/3$. The second, a symmetric spin-liquid state stemming from the $\mathbf{Q} = 0$ *Ansatz* stable in the region $1/3 < J < 1/2$. Finally, the third ground state of the model is a chiral long-range order stemming from the *1H1R Ansatz*. Again, we provided experimental signatures of theses three ground states in the form of static and dynamical structure factors. We showed that the $J = 1/2$ point possesses many features. First because we can have a classical intuition on the location of the boundary at this particular point. Second, because for $J > 1/2$, chiral states are stabilized, as the ground state starting from the *1H1R Ansatz* and as an excited state starting from the $\mathbf{Q} = 0$ *Ansatz*. Finally, we computed the static structure factor of this excited state chiral $\mathbf{Q} = 0$ state yielding half-moon patterns, a feature also present in previous quantum and classical studies [113, 114, 122].

In the end, we revealed rich and complex phase diagrams comporting various magnetically ordered states and exotic quantum spin liquids for the two frustrated systems we studied. Of course, a few directions could be explored next. First, fitting the theory to experimental data on the square-kagome material would be an important next step, in order to find the Hamiltonian describing this material, and the nature of the phase that has been observed in experiments [6]. In order to do so, our self-consistent SBMFT algorithm could be extended to other magnetic models and interaction types such as the XXZ model [84] or the Dzyaloshinskii-Moriya interaction [85]. Second, another interesting direction would be to be able to describe the two frustrated systems we studied not only with bosonic excitations, but also with fermionic excitations. A way to do so would be to develop, as a fermionic counterpart to our SBMFT algorithm, a self-consistent procedure based on the Abrikosov fermion mean-field theory, giving acces

to new potential fermionic ground states. Having the ability to compare fermionic and bosonic results, backed by projective symmetry group classifications, would be of great interest to further explore these frustrated systems.

Appendix A

Theoretical and Numerical Tools

A.1 Generic SBMFT Hamiltonian in Fourier space

After Fourier transformation of the boson operators in the mean-field Hamiltonian 2.19, we get the following generic form with only quadratic terms in boson operators:

$$\begin{aligned}\mathcal{H}_{MF} = &\sum_{l}\sum_{(i\to j)_l}\frac{J_l}{2}\sum_{\mathbf{k}}\big[B^*_{ij}\phi_{ij}\ \hat{b}^{i\dagger}_{\mathbf{k}\uparrow}\hat{b}^{j}_{\mathbf{k}\uparrow} + B^*_{ij}\phi^*_{ij}\ \hat{b}^{i\dagger}_{-\mathbf{k}\downarrow}\hat{b}^{j}_{-\mathbf{k}\downarrow} + B_{ij}\phi^*_{ij}\ \hat{b}^{j\dagger}_{\mathbf{k}\uparrow}\hat{b}^{i}_{\mathbf{k}\uparrow} + B_{ij}\phi_{ij}\ \hat{b}^{j\dagger}_{-\mathbf{k}\downarrow}\hat{b}^{i}_{-\mathbf{k}\downarrow}\\ &- A^*_{ij}\phi^*_{ij}\ \hat{b}^{i}_{\mathbf{k}\uparrow}\hat{b}^{j}_{-\mathbf{k}\downarrow} + A^*_{ij}\phi_{ij}\ \hat{b}^{i}_{-\mathbf{k}\downarrow}\hat{b}^{j}_{\mathbf{k}\uparrow} - A_{ij}\phi_{ij}\ \hat{b}^{j\dagger}_{-\mathbf{k}\downarrow}\hat{b}^{i\dagger}_{\mathbf{k}\uparrow} + A_{ij}\phi^*_{ij}\ \hat{b}^{j\dagger}_{\mathbf{k}\uparrow}\hat{b}^{i\dagger}_{-\mathbf{k}\downarrow}\big]\\ &+\sum_{\mathbf{k}}\sum_{\alpha}\mu_\alpha(\hat{b}^{\alpha\dagger}_{\mathbf{k}\uparrow}\hat{b}^{\alpha}_{\mathbf{k}\uparrow} + \hat{b}^{\alpha}_{-\mathbf{k}\downarrow}\hat{b}^{\alpha\dagger}_{\mathbf{k}\uparrow})\\ &+\sum_{l}\sum_{\langle i,j\rangle_l}J_l(|A_{ij}|^2 - |B_{ij}|^2) - \sum_{\alpha}\mu_\alpha(\kappa+1)n_c\end{aligned} \tag{A.1}$$

Here, the terms $\phi_{ij} = e^{i\mathbf{k}\cdot\boldsymbol{\delta}_{ij}}$ are phase factors where $\boldsymbol{\delta}_{ij}$ is the difference of position between sites i and j. The sum indexed by $(i\to j)_l$ is a summation over all the bonds in the unit cell of reference, for a given coupling J_l. The sum indexed by α runs over the n_u sublattices of the lattice.

A.2 Computation of the new $\{A_{ij}, B_{ij}\}$

We will first derive the expression of A_{ij} evaluated in the Bogoliubov bosons ground state $|\Phi_0\rangle$, noted $\langle\dots\rangle_0$ from now on. Let us start with the expression of the $\hat{A}_{ij}$ operator after an inverse Fourier transform of the Schwinger boson operators:

$$\hat{A}_{ij} = \frac{1}{2n_c}\sum_{\mathbf{k}}(\phi^*_{ij}\hat{b}^{\alpha}_{\mathbf{k}\uparrow}\hat{b}^{\beta}_{-\mathbf{k}\downarrow} - \phi_{ij}\hat{b}^{\alpha}_{-\mathbf{k}\downarrow}\hat{b}^{\beta}_{\mathbf{k}\uparrow}) \tag{A.2}$$

again with $\phi_{ij} = e^{i\mathbf{k}\cdot\boldsymbol{\delta}_{ij}}$ and with the index α (resp. β) corresponding to the sublattice of the site i (resp. j).

Using the transformation matrix and the two relations $\Psi_{\mathbf{k}} = T_{\mathbf{k}}\Gamma_{\mathbf{k}}$ and $\Psi^{\dagger}_{\mathbf{k}} = \Gamma^{\dagger}_{\mathbf{k}}T^{\dagger}_{\mathbf{k}}$ it is possible to express the $\hat{A}_{ij}$ operator in term of Bogoliubov boson operators. Starting with the first term of equation A.2:

$$\begin{aligned}\langle \hat{b}^{\alpha}_{\mathbf{k}\uparrow}\hat{b}^{\beta}_{-\mathbf{k}\downarrow}\rangle_0 &= \Big\langle \Big(\sum_d U_{\alpha,d,\mathbf{k}}\hat{\gamma}^{d}_{\mathbf{k}\uparrow} + X_{\alpha,d,\mathbf{k}}\hat{\gamma}^{d\dagger}_{-\mathbf{k}\downarrow}\Big)\Big(\sum_{d'} V^{*}_{\beta,d',\mathbf{k}}\hat{\gamma}^{d'\dagger}_{\mathbf{k}\uparrow} + Y^{*}_{\beta,d',\mathbf{k}}\hat{\gamma}^{d'}_{-\mathbf{k}\downarrow}\Big)\Big\rangle_0 \\ &= \sum_{d,d'}\Big(U_{\alpha,d,\mathbf{k}}V^{*}_{\beta,d',\mathbf{k}}\langle\hat{\gamma}^{d}_{\mathbf{k}\uparrow}\hat{\gamma}^{d'\dagger}_{\mathbf{k}\uparrow}\rangle_0 + U_{\alpha,d,\mathbf{k}}Y^{*}_{\beta,d',\mathbf{k}}\langle\hat{\gamma}^{d}_{\mathbf{k}\uparrow}\hat{\gamma}^{d'}_{-\mathbf{k}\downarrow}\rangle_0 \\ &+ X_{\alpha,d,\mathbf{k}}V^{*}_{\beta,d',\mathbf{k}}\langle\hat{\gamma}^{d\dagger}_{-\mathbf{k}\downarrow}\hat{\gamma}^{d'\dagger}_{\mathbf{k}\uparrow}\rangle_0 + X_{\alpha,d,\mathbf{k}}Y^{*}_{\beta,d',\mathbf{k}}\langle\hat{\gamma}^{d\dagger}_{-\mathbf{k}\downarrow}\hat{\gamma}^{d'}_{-\mathbf{k}\downarrow}\rangle_0\Big)\end{aligned} \tag{A.3}$$

where the summations over d and d' are from 1 to n_u.

In order to evaluate this expression, we make the assumption that the Bogoliubov boson vacuum $|\Phi\rangle_0$ is gapped. This means that there is no boson condensate in this ground state and consequently we have:

$$\begin{cases}\langle\hat{\gamma}^{d\dagger}_{\mathbf{k}\sigma}\hat{\gamma}^{d'}_{\mathbf{k}\sigma}\rangle_0 = \delta_{d,d'}\langle\hat{n}^{d}_{\mathbf{k},\sigma}\rangle_0 = 0 \\ \langle\hat{\gamma}^{d}_{\mathbf{k}\sigma}\hat{\gamma}^{d'\dagger}_{\mathbf{k}\sigma}\rangle_0 = \delta_{d,d'}\langle 1-\hat{n}^{d}_{\mathbf{k},\sigma}\rangle_0 = \delta_{d,d'}\end{cases} \tag{A.4}$$

Going back to equation A.3, we can now evaluate bilinears such as:

$$\begin{aligned}\langle \hat{b}^{\alpha}_{\mathbf{k}\uparrow}\hat{b}^{\beta}_{-\mathbf{k}\downarrow}\rangle_0 &= \sum_{d,d'} U_{\alpha,d,\mathbf{k}}V^{*}_{\beta,d',\mathbf{k}}\langle\hat{\gamma}^{d}_{\mathbf{k}\uparrow}\hat{\gamma}^{d'\dagger}_{\mathbf{k}\uparrow}\rangle_0 \\ &= \sum_{d} U_{\alpha,d,\mathbf{k}}V^{*}_{\beta,d,\mathbf{k}}\end{aligned} \tag{A.5}$$

Similarly for the second term, we get:

$$\begin{aligned}\langle \hat{b}^{\alpha}_{-\mathbf{k}\downarrow}\hat{b}^{\beta}_{\mathbf{k}\uparrow}\rangle_0 &= \Big\langle \Big(\sum_d V^{*}_{\alpha,d,\mathbf{k}}\hat{\gamma}^{d\dagger}_{\mathbf{k}\uparrow} + Y^{*}_{\alpha,d,\mathbf{k}}\hat{\gamma}^{d}_{-\mathbf{k}\downarrow}\Big)\Big(\sum_{d'} U_{\beta,d',\mathbf{k}}\hat{\gamma}^{d'}_{\mathbf{k}\uparrow} + X_{\beta,d',\mathbf{k}}\hat{\gamma}^{d'\dagger}_{-\mathbf{k}\downarrow}\Big)\Big\rangle_0 \\ &= \sum_{d} Y^{*}_{\alpha,d,\mathbf{k}}X_{\beta,d,\mathbf{k}}\end{aligned} \tag{A.6}$$

Using equation A.2 and the expression of the two previous terms, we get the result displayed in equation 2.37.

We proceed in the same way for the B_{ij} parameter to get equation 2.38.

A.3 Derivation of the static structure factor

Starting with the expression of the static structure factor of equation 2.47, we decompose the spin operators into their three components along x, y and z:

$$S^{\alpha\beta}(\mathbf{k}) = \frac{1}{n_c}\sum_{i,j} e^{i\mathbf{k}\cdot(\mathbf{R_i}-\mathbf{R_j})}\langle \hat{S}^{\alpha}_{x,i}\hat{S}^{\beta}_{x,j} + \hat{S}^{\alpha}_{y,i}\hat{S}^{\beta}_{y,j} + \hat{S}^{\alpha}_{z,i}\hat{S}^{\beta}_{z,j}\rangle_0 \tag{A.7}$$

We can now transform the spin operators using the Schwinger boson operators. Let us start with the x component:

$$S^{\alpha\beta}_{x}(\mathbf{k}) = \frac{1}{4n_c}\sum_{i,j} e^{i\mathbf{k}\cdot(\mathbf{R_i}-\mathbf{R_j})}\langle\ (\hat{b}^{\alpha\dagger}_{i\uparrow}\hat{b}^{\alpha}_{i\downarrow} + \hat{b}^{\alpha\dagger}_{i\downarrow}\hat{b}^{\alpha}_{i\uparrow})(\hat{b}^{\beta\dagger}_{j\uparrow}\hat{b}^{\beta}_{j\downarrow} + \hat{b}^{\beta\dagger}_{j\downarrow}\hat{b}^{\beta}_{j\uparrow})\ \rangle_0 \tag{A.8}$$

Using the Fourier transform of the boson operators:

$$\begin{aligned} S^{\alpha\beta}_{x}(\mathbf{k}) = \frac{1}{4n_c^2}\sum_{i,j}\sum_{\mathbf{q_{1,2,3,4}}} & e^{i\mathbf{k}\cdot(\mathbf{R_i}-\mathbf{R_j})}e^{-i\mathbf{q_1}\cdot\mathbf{R_i}}e^{i\mathbf{q_2}\cdot\mathbf{R_i}}e^{-i\mathbf{q_3}\cdot\mathbf{R_j}}e^{i\mathbf{q_4}\cdot\mathbf{R_j}}\times \\ & \langle\ (\hat{b}^{\alpha\dagger}_{\mathbf{q_1}\uparrow}\hat{b}^{\alpha}_{\mathbf{q_2}\downarrow} + \hat{b}^{\alpha\dagger}_{\mathbf{q_1}\downarrow}\hat{b}^{\alpha}_{\mathbf{q_2}\uparrow})(\hat{b}^{\beta\dagger}_{\mathbf{q_3}\uparrow}\hat{b}^{\beta}_{\mathbf{q_4}\downarrow} + \hat{b}^{\beta\dagger}_{\mathbf{q_3}\downarrow}\hat{b}^{\beta}_{\mathbf{q_4}\uparrow})\ \rangle_0 \end{aligned} \tag{A.9}$$

Or in a simplified form:

$$S^{\alpha\beta}_{x}(\mathbf{k}) = \frac{1}{4n_c}\sum_{\mathbf{q},\mathbf{q'}}\langle\ (\hat{b}^{\alpha\dagger}_{\mathbf{q}\uparrow}\hat{b}^{\alpha}_{\mathbf{q}-\mathbf{k}\downarrow} + \hat{b}^{\alpha\dagger}_{\mathbf{q}\downarrow}\hat{b}^{\alpha}_{\mathbf{q}-\mathbf{k}\uparrow})(\hat{b}^{\beta\dagger}_{\mathbf{q'}-\mathbf{k}\uparrow}\hat{b}^{\beta}_{\mathbf{q'}\downarrow} + \hat{b}^{\beta\dagger}_{\mathbf{q'}-\mathbf{k}\downarrow}\hat{b}^{\beta}_{\mathbf{q'}\uparrow})\ \rangle_0 \tag{A.10}$$

Using the $T_{\mathbf{k}}$ transformation matrices from the Cholesky decomposition, we can write:

$$\begin{aligned} \hat{b}^{\alpha\dagger}_{\mathbf{q}\uparrow}\hat{b}^{\alpha}_{\mathbf{q}-\mathbf{k}\downarrow} + \hat{b}^{\alpha\dagger}_{\mathbf{q}\downarrow}\hat{b}^{\alpha}_{\mathbf{q}-\mathbf{k}\uparrow} &= (U^{*}_{\alpha,d,\mathbf{q}}\hat{\gamma}^{d\dagger}_{\mathbf{q}\uparrow} + X^{*}_{\alpha,d,\mathbf{q}}\hat{\gamma}^{d}_{-\mathbf{q}\downarrow})(V^{*}_{\alpha,d',\mathbf{k}-\mathbf{q}}\hat{\gamma}^{d'\dagger}_{\mathbf{k}-\mathbf{q}\uparrow} + Y^{*}_{\alpha,d',\mathbf{k}-\mathbf{q}}\hat{\gamma}^{d}_{\mathbf{q}-\mathbf{k}\downarrow}) \\ &+ (V_{\alpha,d,-\mathbf{q}}\hat{\gamma}^{d}_{-\mathbf{q}\uparrow} + Y_{\alpha,d,-\mathbf{q}}\hat{\gamma}^{d\dagger}_{\mathbf{q}\downarrow})(U_{\alpha,d',\mathbf{q}-\mathbf{k}}\hat{\gamma}^{d'}_{\mathbf{q}-\mathbf{k}\uparrow} + X_{\alpha,d',\mathbf{q}-\mathbf{k}}\hat{\gamma}^{d'\dagger}_{\mathbf{k}-\mathbf{q}\downarrow}) \\ &\equiv X^{*}_{\alpha,d,\mathbf{q}}Y^{*}_{\alpha,d',\mathbf{k}-\mathbf{q}}\hat{\gamma}^{d}_{-\mathbf{q}\downarrow}\hat{\gamma}^{d'}_{\mathbf{q}-\mathbf{k}\downarrow} + V_{\alpha,d,-\mathbf{q}}U_{\alpha,d',\mathbf{q}-\mathbf{k}}\hat{\gamma}^{d}_{-\mathbf{q}\uparrow}\hat{\gamma}^{d'}_{\mathbf{q}-\mathbf{k}\uparrow} \end{aligned} \tag{A.11}$$

where the summation over d and d' indexes is implied. We also have:

$$\begin{aligned} \hat{b}^{\beta\dagger}_{\mathbf{q'}-\mathbf{k}\uparrow}\hat{b}^{\beta}_{\mathbf{q'}\downarrow} + \hat{b}^{\beta\dagger}_{\mathbf{q'}-\mathbf{k}\downarrow}\hat{b}^{\beta}_{\mathbf{q'}\uparrow} &= (U^{*}_{\beta,d,\mathbf{q'}-\mathbf{k}}\hat{\gamma}^{d\dagger}_{\mathbf{q'}-\mathbf{k}\uparrow} + X^{*}_{\beta,d,\mathbf{q'}-\mathbf{k}}\hat{\gamma}^{d}_{\mathbf{k}-\mathbf{q'}\downarrow})(V^{*}_{\beta,d',-\mathbf{q'}}\hat{\gamma}^{d'\dagger}_{-\mathbf{q'}\uparrow} + Y^{*}_{\beta,d',-\mathbf{q'}}\hat{\gamma}^{d'}_{\mathbf{q'}\downarrow}) \\ &+ (V_{\beta,d,\mathbf{k}-\mathbf{q'}}\hat{\gamma}^{d}_{\mathbf{k}-\mathbf{q'}\uparrow} + Y_{\beta,d,\mathbf{k}-\mathbf{q'}}\hat{\gamma}^{d\dagger}_{\mathbf{q'}-\mathbf{k}\downarrow})(U_{\beta,d',\mathbf{q'}}\hat{\gamma}^{d'}_{\mathbf{q'}\uparrow} + X_{\beta,d',\mathbf{q'}}\hat{\gamma}^{d'\dagger}_{-\mathbf{q'}\downarrow}) \\ &\equiv U^{*}_{\beta,d,\mathbf{q'}-\mathbf{k}}V^{*}_{\beta,d',-\mathbf{q'}}\hat{\gamma}^{d\dagger}_{\mathbf{q'}-\mathbf{k}\uparrow}\hat{\gamma}^{d'\dagger}_{-\mathbf{q'}\uparrow} + Y_{\beta,d,\mathbf{k}-\mathbf{q'}}X_{\beta,d',\mathbf{q'}}\hat{\gamma}^{d\dagger}_{\mathbf{q'}-\mathbf{k}\downarrow}\hat{\gamma}^{d'\dagger}_{-\mathbf{q'}\downarrow} \end{aligned} \tag{A.12}$$

where the only terms left are the ones that will have a non zero expectation value in the vacuum $|\Phi_0\rangle$.

To verify this, we compute the two non-zero expectation values of the quartic Bogoliubov operators terms. Firstly:

$$\begin{aligned}
&\langle \hat{\gamma}^{d_1}_{-\mathbf{q}\downarrow}\hat{\gamma}^{d_2}_{\mathbf{q}-\mathbf{k}\downarrow}\hat{\gamma}^{d_3\dagger}_{\mathbf{q}'-\mathbf{k}\downarrow}\hat{\gamma}^{d_4\dagger}_{-\mathbf{q}'\downarrow}\rangle_0 = \delta_{\mathbf{q}-\mathbf{k},-\mathbf{q}'}\delta_{d_2,d_4}\langle \hat{\gamma}^{d_1}_{-\mathbf{q}\downarrow}\hat{\gamma}^{d_3\dagger}_{\mathbf{q}'-\mathbf{k}\downarrow}\rangle_0 + \langle \hat{\gamma}^{d_1}_{-\mathbf{q}\downarrow}\hat{\gamma}^{d_4\dagger}_{-\mathbf{q}'\downarrow}\hat{\gamma}^{d_2}_{\mathbf{q}-\mathbf{k}\downarrow}\hat{\gamma}^{d_3\dagger}_{\mathbf{q}'-\mathbf{k}\downarrow}\rangle_0 \\
&= \delta_{\mathbf{q}',\mathbf{k}-\mathbf{q}}\delta_{d_2,d_4}(\delta_{d_1,d_3} + \langle \hat{\gamma}^{d_3\dagger}_{\mathbf{q}'-\mathbf{k}\downarrow}\hat{\gamma}^{d_1}_{-\mathbf{q}\downarrow}\rangle_0) + \delta_{\mathbf{q}-\mathbf{k},\mathbf{q}'-\mathbf{k}}\delta_{d_2,d_3}\langle \hat{\gamma}^{d_1}_{-\mathbf{q}\downarrow}\hat{\gamma}^{d_4\dagger}_{-\mathbf{q}'\downarrow}\rangle_0 \\
&+ \langle \hat{\gamma}^{d_1}_{-\mathbf{q}\downarrow}\hat{\gamma}^{d_4\dagger}_{-\mathbf{q}'\downarrow}\hat{\gamma}^{d_3\dagger}_{\mathbf{q}'-\mathbf{k}\downarrow}\hat{\gamma}^{d_2}_{\mathbf{q}-\mathbf{k}\downarrow}\rangle_0 \\
&= \delta_{\mathbf{q}',\mathbf{k}-\mathbf{q}}\delta_{d_2,d_4}\delta_{d_1,d_3} + \delta_{\mathbf{q},\mathbf{q}'}\delta_{d_2,d_3}(\delta_{d_1,d_4} + \langle \hat{\gamma}^{d_4\dagger}_{-\mathbf{q}'\downarrow}\hat{\gamma}^{d_1}_{-\mathbf{q}\downarrow}\rangle_0) \\
&(+\delta_{\mathbf{q},\mathbf{q}'}\delta_{d_1,d_4}\langle \hat{\gamma}^{d_3\dagger}_{\mathbf{q}'-\mathbf{k}\downarrow}\hat{\gamma}^{d_2}_{\mathbf{q}-\mathbf{k}\downarrow}\rangle_0 + \langle \hat{\gamma}^{d_4\dagger}_{-\mathbf{q}'\downarrow}\hat{\gamma}^{d_1}_{-\mathbf{q}\downarrow}\hat{\gamma}^{d_3\dagger}_{\mathbf{q}'-\mathbf{k}\downarrow}\hat{\gamma}^{d_2}_{\mathbf{q}-\mathbf{k}\downarrow}\rangle_0) \\
&= \delta_{\mathbf{q}',\mathbf{k}-\mathbf{q}}\delta_{d_2,d_4}\delta_{d_1,d_3} + \delta_{\mathbf{q},\mathbf{q}'}\delta_{d_1,d_4}\delta_{d_2,d_3}
\end{aligned} \tag{A.13}$$

where we have used the fact that in the absence of Bose-Einstein condensation in this ground state the following expectation values are equal to zero:

$$\langle \hat{n}^d_{\mathbf{q}\sigma}\rangle = \langle \hat{\gamma}^{d\dagger}_{\mathbf{q}\sigma}\hat{\gamma}^{d}_{\mathbf{q}\sigma}\rangle_0 = 0 = \langle \hat{\gamma}^{d\dagger}_{\mathbf{q}\sigma}\hat{\gamma}^{d}_{\mathbf{q}\sigma}\hat{\gamma}^{d\dagger}_{\mathbf{q}\sigma}\hat{\gamma}^{d}_{\mathbf{q}\sigma}\rangle_0 \tag{A.14}$$

Similarly:

$$\langle \hat{\gamma}^{d_1}_{-\mathbf{q}\uparrow}\hat{\gamma}^{d_2}_{\mathbf{q}-\mathbf{k}\uparrow}\hat{\gamma}^{d_3\dagger}_{\mathbf{q}'-\mathbf{k}\uparrow}\hat{\gamma}^{d_4\dagger}_{-\mathbf{q}'\uparrow}\rangle_0 = \delta_{\mathbf{q},\mathbf{q}'}\delta_{d_1,d_4}\delta_{d_2,d_3} + \delta_{\mathbf{q}',\mathbf{q}-\mathbf{k}}\delta_{d_1,d_3}\delta_{d_2,d_4} \tag{A.15}$$

Those two terms are now reflected in the x-term of the static structure factor:

$$\begin{aligned}
S^{\alpha\beta}_x(\mathbf{k}) = \frac{1}{4n_c}\sum_{\mathbf{q}}\sum_{d,d'}[\ & X^*_{\alpha,d,\mathbf{q}}Y^*_{\alpha,d',\mathbf{k}-\mathbf{q}}(Y_{\beta,d',\mathbf{k}-\mathbf{q}}X_{\beta,d,\mathbf{q}} + Y_{\beta,d,\mathbf{q}}X_{\beta,d',\mathbf{k}-\mathbf{q}}) \\
&+ V_{\alpha,d,-\mathbf{q}}U_{\alpha,d',\mathbf{q}-\mathbf{k}}(U^*_{\beta,d',\mathbf{q}-\mathbf{k}}V^*_{\beta,d,-\mathbf{q}} + U^*_{\beta,d,-\mathbf{q}}V^*_{\beta,d',\mathbf{q}-\mathbf{k}})\ ]
\end{aligned} \tag{A.16}$$

The computation of the y-term is very similar since the change of signs does not affect the final terms:

$$\begin{aligned}
S^{\alpha\beta}_y(\mathbf{k}) &= -\frac{1}{4n_c}\sum_{\mathbf{q},\mathbf{q}'}\langle\ (\hat{b}^{\alpha\dagger}_{\mathbf{q}\uparrow}\hat{b}^{\alpha}_{\mathbf{q}-\mathbf{k}\downarrow} - \hat{b}^{\alpha\dagger}_{\mathbf{q}\downarrow}\hat{b}^{\alpha}_{\mathbf{q}-\mathbf{k}\uparrow})(\hat{b}^{\beta\dagger}_{\mathbf{q}'-\mathbf{k}\uparrow}\hat{b}^{\beta}_{\mathbf{q}'\downarrow} - \hat{b}^{\beta\dagger}_{\mathbf{q}'-\mathbf{k}\downarrow}\hat{b}^{\beta}_{\mathbf{q}'\uparrow})\ \rangle_0 \\
&= \frac{1}{4n_c}\sum_{\mathbf{q}}\sum_{d,d'}[\ X^*_{\alpha,d,\mathbf{q}}Y^*_{\alpha,d',\mathbf{k}-\mathbf{q}}(Y_{\beta,d',\mathbf{k}-\mathbf{q}}X_{\beta,d,\mathbf{q}} + Y_{\beta,d,\mathbf{q}}X_{\beta,d',\mathbf{k}-\mathbf{q}}) \\
&+ V_{\alpha,d,-\mathbf{q}}U_{\alpha,d',\mathbf{q}-\mathbf{k}}(U^*_{\beta,d',\mathbf{q}-\mathbf{k}}V^*_{\beta,d,-\mathbf{q}} + U^*_{\beta,d,-\mathbf{q}}V^*_{\beta,d',\mathbf{q}-\mathbf{k}})\ ]
\end{aligned} \tag{A.17}$$

Finally, for the z-term we have:

$$S_z^{\alpha\beta}(\mathbf{k}) = \frac{1}{4n_c}\sum_{\mathbf{q},\mathbf{q}'}\langle\ (\hat{b}^{\alpha\dagger}_{\mathbf{q}\uparrow}\hat{b}^{\alpha}_{\mathbf{q}-\mathbf{k}\uparrow} - \hat{b}^{\alpha\dagger}_{\mathbf{q}\downarrow}\hat{b}^{\alpha}_{\mathbf{q}-\mathbf{k}\downarrow})(\hat{b}^{\beta\dagger}_{\mathbf{q}'-\mathbf{k}\uparrow}\hat{b}^{\beta}_{\mathbf{q}'\uparrow} - \hat{b}^{\beta\dagger}_{\mathbf{q}'-\mathbf{k}\downarrow}\hat{b}^{\beta}_{\mathbf{q}'\downarrow})\ \rangle_0 \tag{A.18}$$

Again, using the $T_{\mathbf{k}}$ transformation matrices:

$$\begin{aligned}\hat{b}^{\alpha\dagger}_{\mathbf{q}\uparrow}\hat{b}^{\alpha}_{\mathbf{q}-\mathbf{k}\uparrow} - \hat{b}^{\alpha\dagger}_{\mathbf{q}\downarrow}\hat{b}^{\alpha}_{\mathbf{q}-\mathbf{k}\downarrow} &= (U^*_{\alpha,d,\mathbf{q}}\hat{\gamma}^{d\dagger}_{\mathbf{q}\uparrow} + X^*_{\alpha,d,\mathbf{q}}\hat{\gamma}^{d}_{-\mathbf{q}\downarrow})(U_{\alpha,d',\mathbf{q}-\mathbf{k}}\hat{\gamma}^{d'}_{\mathbf{q}-\mathbf{k}\uparrow} + X_{\alpha,d',\mathbf{q}-\mathbf{k}}\hat{\gamma}^{d'\dagger}_{\mathbf{k}-\mathbf{q}\downarrow})\\ &\quad - (V_{\alpha,d,-\mathbf{q}}\hat{\gamma}^{d}_{-\mathbf{q}\uparrow} + Y_{\alpha,d,-\mathbf{q}}\hat{\gamma}^{d\dagger}_{\mathbf{q}\downarrow})(V^*_{\alpha,d',\mathbf{k}-\mathbf{q}}\hat{\gamma}^{d'\dagger}_{\mathbf{k}-\mathbf{q}\uparrow} + Y^*_{\alpha,d',\mathbf{k}-\mathbf{q}}\hat{\gamma}^{d'}_{\mathbf{q}-\mathbf{k}\downarrow})\\ &\equiv X^*_{\alpha,d,\mathbf{q}}U_{\alpha,d',\mathbf{q}-\mathbf{k}}\hat{\gamma}^{d}_{-\mathbf{q}\downarrow}\hat{\gamma}^{d'}_{\mathbf{q}-\mathbf{k}\uparrow} - V_{\alpha,d,-\mathbf{q}}Y^*_{\alpha,d',\mathbf{k}-\mathbf{q}}\hat{\gamma}^{d}_{-\mathbf{q}\uparrow}\hat{\gamma}^{d'}_{\mathbf{q}-\mathbf{k}\downarrow}\end{aligned} \tag{A.19}$$

and:

$$\begin{aligned}\hat{b}^{\beta\dagger}_{\mathbf{q}'-\mathbf{k}\uparrow}\hat{b}^{\beta}_{\mathbf{q}'\uparrow} - \hat{b}^{\beta\dagger}_{\mathbf{q}'-\mathbf{k}\downarrow}\hat{b}^{\beta}_{\mathbf{q}'\downarrow} &= (U^*_{\beta,d,\mathbf{q}'-\mathbf{k}}\hat{\gamma}^{d\dagger}_{\mathbf{q}'-\mathbf{k}\uparrow} + X^*_{\beta,d,\mathbf{q}'-\mathbf{k}}\hat{\gamma}^{d}_{\mathbf{k}-\mathbf{q}'\downarrow})(U_{\beta,d',\mathbf{q}'}\hat{\gamma}^{d'}_{\mathbf{q}'\uparrow} + X_{\beta,d',\mathbf{q}'}\hat{\gamma}^{d'\dagger}_{-\mathbf{q}'\downarrow})\\ &\quad - (V_{\beta,d,\mathbf{k}-\mathbf{q}'}\hat{\gamma}^{d}_{\mathbf{k}-\mathbf{q}'\uparrow} + Y_{\beta,d,\mathbf{k}-\mathbf{q}'}\hat{\gamma}^{d\dagger}_{\mathbf{q}'-\mathbf{k}\downarrow})(V^*_{\beta,d',-\mathbf{q}'}\hat{\gamma}^{d'\dagger}_{\mathbf{q}'\uparrow} + Y^*_{\beta,d',-\mathbf{q}'}\hat{\gamma}^{d'}_{\mathbf{q}'\downarrow})\\ &\equiv U^*_{\beta,d,\mathbf{q}'-\mathbf{k}}X_{\beta,d',\mathbf{q}'}\hat{\gamma}^{d\dagger}_{\mathbf{q}'-\mathbf{k}\uparrow}\hat{\gamma}^{d'\dagger}_{-\mathbf{q}'\downarrow} - Y_{\beta,d,\mathbf{k}-\mathbf{q}'}V^*_{\beta,d',-\mathbf{q}'}\hat{\gamma}^{d\dagger}_{\mathbf{q}'-\mathbf{k}\downarrow}\hat{\gamma}^{d\dagger}_{-\mathbf{q}'\uparrow}\end{aligned} \tag{A.20}$$

We now have four different non-zero contributions of quartic Bogoliubov operator terms:

$$\begin{aligned}\langle\hat{\gamma}^{d_1}_{-\mathbf{q}\downarrow}\hat{\gamma}^{d_2}_{\mathbf{q}-\mathbf{k}\uparrow}\hat{\gamma}^{d_3\dagger}_{\mathbf{q}'-\mathbf{k}\downarrow}\hat{\gamma}^{d_4\dagger}_{-\mathbf{q}'\uparrow}\rangle_0 &= \delta_{\mathbf{q}',\mathbf{k}-\mathbf{q}}\delta_{d_1,d_3}\delta_{d_2,d_4}\\ \langle\hat{\gamma}^{d_1}_{-\mathbf{q}\downarrow}\hat{\gamma}^{d_2}_{\mathbf{q}-\mathbf{k}\uparrow}\hat{\gamma}^{d_3\dagger}_{\mathbf{q}'-\mathbf{k}\uparrow}\hat{\gamma}^{d_4\dagger}_{-\mathbf{q}'\downarrow}\rangle_0 &= \delta_{\mathbf{q},\mathbf{q}'}\delta_{d_1,d_4}\delta_{d_2,d_3}\\ \langle\hat{\gamma}^{d_1}_{-\mathbf{q}\uparrow}\hat{\gamma}^{d_2}_{\mathbf{q}-\mathbf{k}\downarrow}\hat{\gamma}^{d_3\dagger}_{\mathbf{q}'-\mathbf{k}\downarrow}\hat{\gamma}^{d_4\dagger}_{-\mathbf{q}'\uparrow}\rangle_0 &= \delta_{\mathbf{q},\mathbf{q}'}\delta_{d_1,d_4}\delta_{d_2,d_3}\\ \langle\hat{\gamma}^{d_1}_{-\mathbf{q}\uparrow}\hat{\gamma}^{d_2}_{\mathbf{q}-\mathbf{k}\downarrow}\hat{\gamma}^{d_3\dagger}_{\mathbf{q}'-\mathbf{k}\uparrow}\hat{\gamma}^{d_4\dagger}_{-\mathbf{q}'\downarrow}\rangle_0 &= \delta_{\mathbf{q}',\mathbf{k}-\mathbf{q}}\delta_{d_1,d_3}\delta_{d_2,d_4}\end{aligned} \tag{A.21}$$

This yields:

$$\begin{aligned}S_z^{\alpha\beta}(\mathbf{k}) = \frac{1}{4n_c}\sum_{\mathbf{q}}\sum_{d,d'}[\ &X^*_{\alpha,d,\mathbf{q}}U_{\alpha,d',\mathbf{q}-\mathbf{k}}(U^*_{\beta,d',\mathbf{q}-\mathbf{k}}X_{\beta,d,\mathbf{q}} - Y_{\beta,d,\mathbf{q}}V^*_{\beta,d',\mathbf{q}-\mathbf{k}})\\ &+ V_{\alpha,d,-\mathbf{q}}Y^*_{\alpha,d',\mathbf{k}-\mathbf{q}}(-U^*_{\beta,d,-\mathbf{q}}X_{\beta,d',\mathbf{k}-\mathbf{q}} + Y_{\beta,d',\mathbf{k}-\mathbf{q}}V^*_{\beta,d,-\mathbf{q}})\ ]\end{aligned} \tag{A.22}$$

In the end, we get the same expression as equation 2.48 in the main text:

$$\begin{aligned}S^{\alpha\beta}(\mathbf{k}) = \frac{1}{4n_c}\sum_{\mathbf{q}}\sum_{d,d'}[\ &2X^*_{\alpha,d,\mathbf{q}}Y^*_{\alpha,d',\mathbf{k}-\mathbf{q}}(Y_{\beta,d',\mathbf{k}-\mathbf{q}}X_{\beta,d,\mathbf{q}} + Y_{\beta,d,\mathbf{q}}X_{\beta,d',\mathbf{k}-\mathbf{q}})\\ &+ 2V_{\alpha,d,-\mathbf{q}}U_{\alpha,d',\mathbf{q}-\mathbf{k}}(U^*_{\beta,d',\mathbf{q}-\mathbf{k}}V^*_{\beta,d,-\mathbf{q}} + U^*_{\beta,d,-\mathbf{q}}V^*_{\beta,d',\mathbf{q}-\mathbf{k}})\\ &+ X^*_{\alpha,d,\mathbf{q}}U_{\alpha,d',\mathbf{q}-\mathbf{k}}(U^*_{\beta,d',\mathbf{q}-\mathbf{k}}X_{\beta,d,\mathbf{q}} - Y_{\beta,d,\mathbf{q}}V^*_{\beta,d',\mathbf{q}-\mathbf{k}})\\ &+ V_{\alpha,d,-\mathbf{q}}Y^*_{\alpha,d',\mathbf{k}-\mathbf{q}}(-U^*_{\beta,d,-\mathbf{q}}X_{\beta,d',\mathbf{k}-\mathbf{q}} + Y_{\beta,d',\mathbf{k}-\mathbf{q}}V^*_{\beta,d,-\mathbf{q}})\ ]\end{aligned} \tag{A.23}$$

Appendix B

Topological Nematic Spin Liquid on the Square Kagome Lattice

B.1 Analytical SBMFT Hamiltonian on the SKL

The following will provide the analytical expression of the Schwinger boson mean-field Hamiltonian for the J_1-J_2 Heisenberg model on the $n_u = 6$ SKL.

We use the following spinor to represent the Hamiltonian:

$$\Psi_{\mathbf{k}} = (\hat{b}^1_{\mathbf{k}\uparrow}, ..., \hat{b}^{n_u}_{\mathbf{k}\uparrow}, \hat{b}^{1\dagger}_{-\mathbf{k}\downarrow}, ..., \hat{b}^{n_u\dagger}_{-\mathbf{k}\downarrow})^T \tag{B.1}$$

where n_u is the number of site per unit cell.

The unit cell and the numerotation of the site are indicated on figure 3.1.

The mean-field Hamiltonian takes the form:

$$\mathcal{H} = \sum_{\mathbf{k}} \Psi^\dagger_{\mathbf{k}} M_{\mathbf{k}} \Psi_{\mathbf{k}} + constant \tag{B.2}$$

The matrix $M_{\mathbf{k}}$ can be expressed under the bloc form:

$$M_{\mathbf{k}} = \begin{pmatrix} R_{\mathbf{k}}(\mathcal{B}) & Q_{\mathbf{k}}(\mathcal{A}) \\ \\ Q_{\mathbf{k}}(-\mathcal{A}^*) & R_{\mathbf{k}}(\mathcal{B}^*) \end{pmatrix} \tag{B.3}$$

where $\mathcal{A}$ (resp. $\mathcal{B}$) is the set of the 12 mean-field parameters A_{ij} (resp. B_{ij}) and:

$$R_{\mathbf{k}}(\mathcal{B}) = \begin{pmatrix} \mu_0 & B^*_{01}\Phi_{01} & 0 & B_{30}\Phi^*_{30} & B^*_{04}\Phi_{04} & B_{50}\Phi^*_{50} \\ B_{01}\Phi^*_{04} & \mu_1 & B^*_{12}\Phi_{12} & 0 & B_{41}\Phi_1\Phi^*_{41} & B^*_{15}\Phi_{15} \\ 0 & B_{12}\Phi_{12}* & \mu_2 & B^*_{23}\Phi_{23} & B^*_{24}\Phi_1\Phi_{24} & B_{52}\Phi_2\Phi^*_{52} \\ B^*_{30}\Phi_{30} & 0 & B_{23}\Phi^*_{23} & \mu_3 & B_{43}\Phi^*_{43} & B^*_{35}\Phi_2\Phi_{35} \\ B_{04}\Phi^*_{04} & B^*_{41}\Phi^*_1\Phi_{41} & B_{24}\Phi^*_1\Phi^*_{24} & B^*_{43}\Phi_{43} & \mu_4 & 0 \\ B^*_{50}\Phi_{50} & B_{15}\Phi^*_{15} & B^*_{52}\Phi^*_2\Phi_{52} & B_{35}\Phi^*_2\Phi^*_{35} & 0 & \mu_5 \end{pmatrix} \tag{B.4}$$

$$Q_{\mathbf{k}}(\mathcal{A}) = \begin{pmatrix} 0 & -A_{01}\Phi_{01} & 0 & A_{30}\Phi^*_{30} & -A_{04}\Phi_{04} & A_{50}\Phi^*_{50} \\ A_{01}\Phi^*_{01} & 0 & -A_{12}\Phi_{12} & 0 & A_{41}\Phi_1\Phi^*_{41} & -A_{15}\Phi_{15} \\ 0 & A_{12}\Phi^*_{12} & 0 & -A_{23}\Phi_{23} & -A_{24}\Phi_1\Phi_{24} & A_{52}\Phi_2\Phi^*_{52} \\ -A_{30} & 0 & A_{23}\Phi^*_{23} & 0 & A_{43}\Phi^*_{43} & -A_{35}\Phi_2\Phi_{35} \\ A_{04}\Phi^*_{04} & -A_{41}\Phi^*_1\Phi_{41} & A_{24}\Phi^*_1\Phi^*_{24} & -A_{43}\Phi_{43} & 0 & 0 \\ -A_{50}\Phi_{50} & A_{15}\Phi^*_{15} & -A_{52}\Phi^*_2\Phi_{52} & A_{35}\Phi^*_2\Phi^*_{35} & 0 & 0 \end{pmatrix} \tag{B.5}$$

with:

$$\Phi_1 = e^{i\mathbf{k}\cdot\mathbf{e_1}} \quad \text{and} \quad \Phi_2 = e^{i\mathbf{k}\cdot\mathbf{e_2}} \tag{B.6}$$

The $\Phi_{\alpha\beta}$ are defined as $e^{i\mathbf{k}\cdot(\mathbf{r}_\alpha - \mathbf{r}_\beta)}$ where $\mathbf{r}_\alpha$ and $\mathbf{r}_\beta$ are the position of two sublattices in the same unitcell.

B.2 Reaching the thermodynamic limit

Working on finite size systems within our SBMFT approach, it is paramount to characterize the potential finite size effect. The next step is to provide a way that allows the computation of various physical quantities in the thermodynamical limit, such as the energy gap Δ and the order wave-vector $\mathbf{Q}$ minimizing the dispersion relation.

The incommensurate orders and the TNSL phases of chapter 3 presented strong size effects principally in the values of Δ and $\mathbf{Q}$. To dispose of such undesired effects, let us look at the behavior of the mean-field parameters as a function of the system size. Fortunately, the mean-field parameters are computed in reciprocal space by summing over the whole Brillouin zone. This makes them much less sensible to finite size effects than quantites defined by a single wave-vector such as the energy gap .

The idea here is to perform a finite size study of the mean-field parameters for a given ground state and determine the size of the system l_{min} above which the parameters

become constant. Such a finite size study is represented in figure B.1, for the mean-field parameters on the J_1 bonds of the TNSL phase at $x = 1$. We see that these mean-field parameters become constant for system sizes $l > l_{min} = 60$. The same behavior holds for the mean-field parameters on the J_2 bonds (both A_{ij} and B_{ij}) and for the n_u Lagrange multipliers.

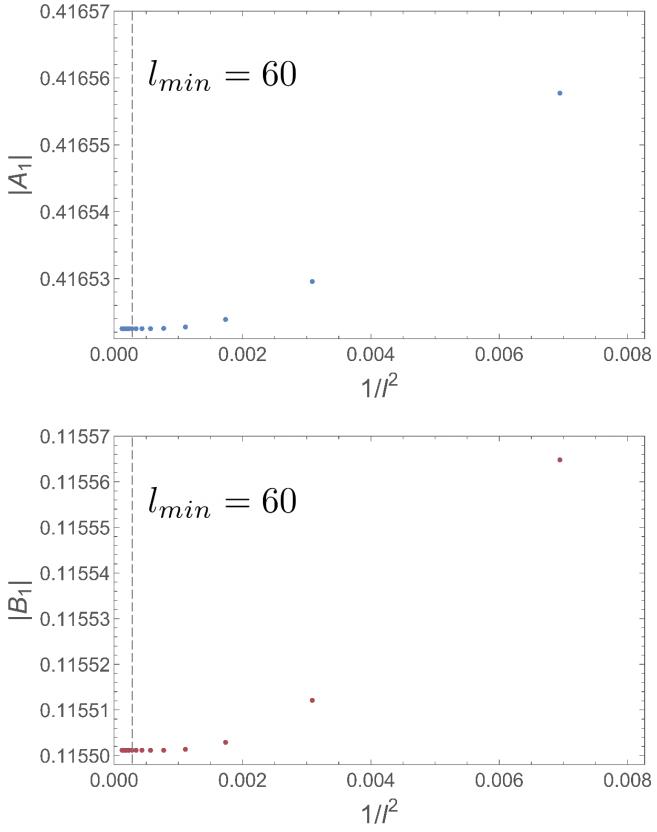

Figure B.1: Finite size study of the mean-field parameters of the TNSL for $x = 1$. A_1 on the upper pannel (resp. B_1 on the lower pannel) corresponds to the uniform amplitude of the A_{ij} (resp. B_{ij}) parameters on the J_1 bonds. They both become constant for system sizes $l > l_{min} = 60$. The same is true for the mean-field parameters on the J_2 bonds and the n_u Lagrange multipliers (not represented here).

Taking advantage of this fact, it is now possible to construct an asymptotic *Ansatz*, composed of these constant values of the mean-field parameters, allowing one to completely bypass the self-consistent procedure and to directly compute the dispersion relation for larger system sizes. It is also possible to compute the dispersion relation in the continuum (limit of an infinite system size) and then minimize it to obtain the values of Δ and $\mathbf{Q}$ in the thermodynamic limit.

To illustrate the strenght of this method, we have displayed in figure B.2 the values of the energy gap in the TNSL at $x = 1$ as a function of $1/l^2$ as well as its value in the thermodynamic limit (gray line). This thermodynamic limit value was computed in the

continuum as explained above and the blue points obtained by going to very large sizes up to 4860000 sites using the asymptotic *Ansatz* of the TNSL.

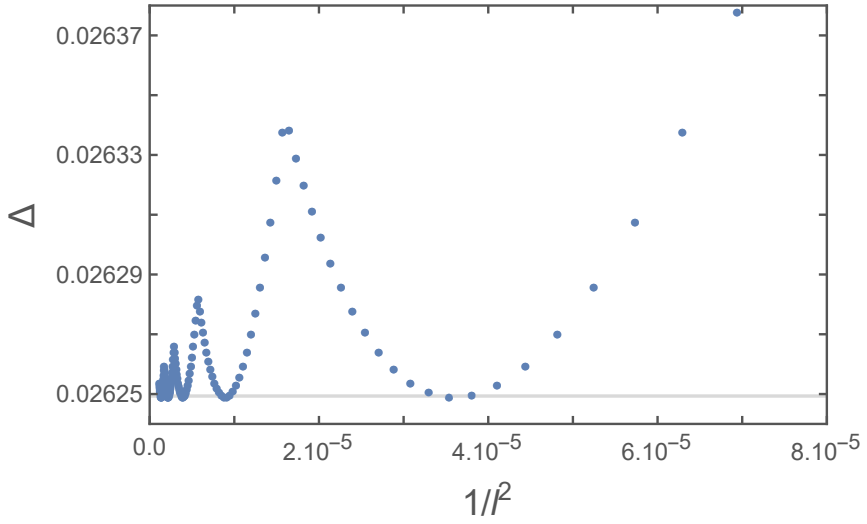

Figure B.2: Energy gap Δ as a function of $1/l^2$ (blue dots). The gray line represent the value of Δ in the thermodynamic limit, computed by minimizing the dispersion relation in the continuum with an asymptotic *Ansatz*. The oscillations are caused by the incommensurability of the wave-vector minimizing the relation dispersion in the finite systems. Interestingly, the minimum of the oscillations correspond to the asymptotic value on the gray line.

The size effects are clearly visible in figure B.2 and lead to oscillations in the value of the gap for finite size systems caused by the incommensurability of $\mathbf{Q}$. Interestingly the minimum of the oscillations correspond to the value of Δ in the thermodynamic limit. Moreover, these oscillations diminish in intensity as the system size increases which indicates that the energy gap for finite systems should tend towards the asymptotic gray line as l grows larger.

This method has proven very useful to determine the values of Δ for a broad range of x allowing a precise localization of the boundaries of the TNSL defined by the closing of the gap. However, in the case of the incommensurate orders convergence difficulties for large sizes appear beyond $l = 102$ that can prevent the access to the thermodynamical limit of the mean-field parameters and thus to the associated asymptotic *Ansatz*.

Appendix C

$J_1 - J_2 - J_3$ Heisenberg Model on the Kagome Lattice

C.1 $n_u = 6$ unit cell

We further describe the $n_u = 6$ unit cell of reference that was used in our Schwinger boson study on the kagome lattice by representing both the J_2 and J_3 oriented bonds on figures C.1 and C.2. Along with the 6 Lagrange multipliers, one for each site, an *Ansatz* on this $n_u = 6$ unit cell is thus composed of 72 mean-field parameters, two for each of the 36 oriented bonds.

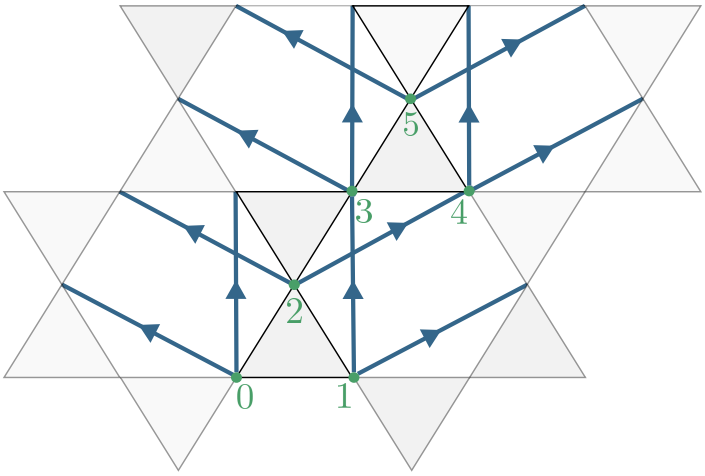

Figure C.1: Representation of the 12 oriented J_2 bonds (in blue) on the $n_u = 6$ unit cell of the kagome lattice. Each oriented bond corresponds to two mean-field paramters A_{ij} and B_{ij}.

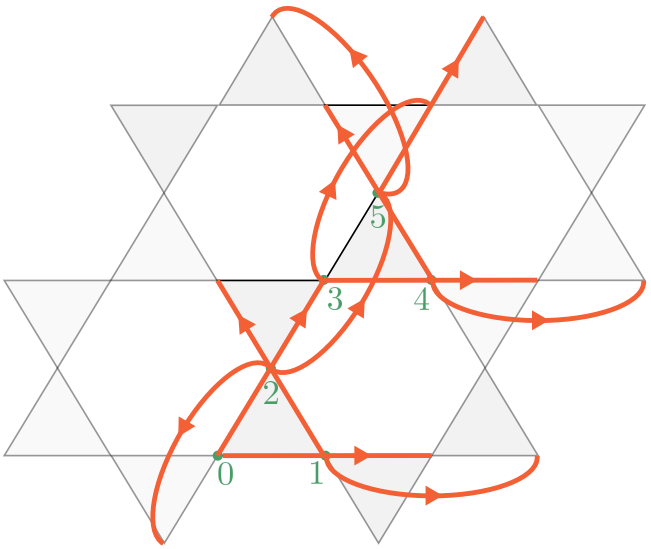

Figure C.2: Representation of the 12 oriented J_3 bonds (in orange) on the $n_u = 6$ unit cell of the kagome lattice. Each oriented bond corresponds to two mean-field paramters A_{ij} and B_{ij}.

C.2 Stability against quantum fluctuations

In this appendix, we will carry out a brief study of the stability against quantum fluctuations of the three ground states of the $J_1 - J_2 - J_3$ Heisenberg model on the kagome lattice. In the SBMFT framework, the spin length S can be thought of as a continuous parameter. It is determined by the average number of bosons per site through the constraint 2.14 seen in chapter 2. The modification of S will allow one to mimic stronger or weaker quantum fluctuations in the system. For instance, taking $S \to +\infty$ will correspond to the classical limit where the ground state of the system is long-range ordered with a Bose-Einstein condensation of the Schwinger bosons. On the contrary, reducing the spin length S will mimic an increase in quantum fluctuations favorising gapped and disordered ground states.

To describe best the effect of the increasing or decreasing quantum fluctuations, we provide dynamical structure factors as well as finite size studies of the energy gap[1]. These physical quantities will allow one to easily check wether or not the ground state is gapped and thus determine what increase (resp. decrease) in quantum fluctuations is necessary to destabilize the associated ordered (resp. disordered) ground state. For all following dynamical structure factors, we have set the maximum of $S(\mathbf{k}, \omega)$ to unity and represented them using the green path of figure 4.19.

[1]These finite size studies are coupled to a non-linear extrapolation for cases where the spin length is too large and leads to convergence issues due to Bose-Einstein condensation.

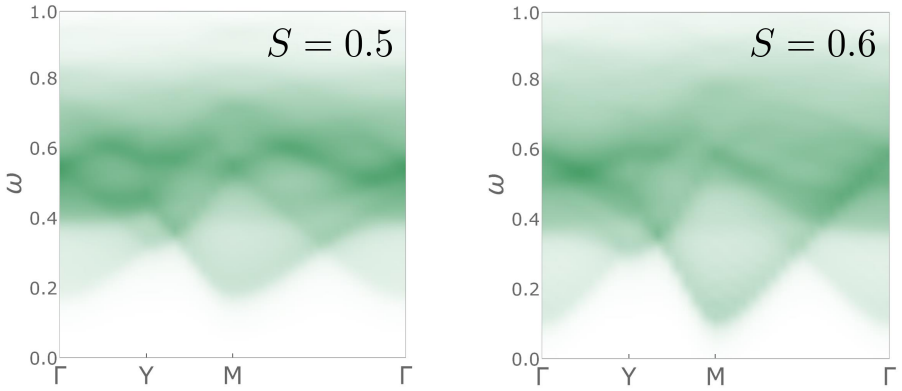

Figure C.3: Dynamical structure factors of the *cuboc1** ground state at $J = 0.2$ for a spin length of $S = 0.5$ (left) and $S = 0.6$ (right). The ground state remains gapped with $\Delta = 0.08675$ for $S = 0.5$ and $\Delta = 0.0486536$ for $S = 0.6$.

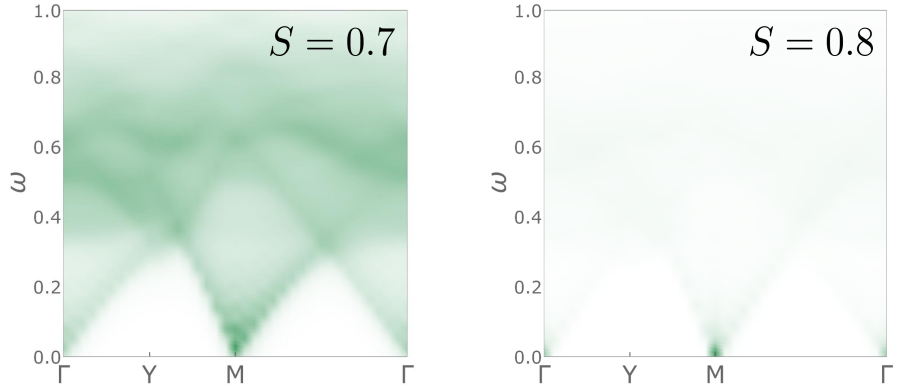

Figure C.4: Dynamical structure factors of the *cuboc1** ground state at $J = 0.2$ for $S = 0.7$ (left) and $S = 0.8$ (right). The ground state progressively becomes gapless with $\Delta = 0.00943$ for $S = 0.7$ and $\Delta = 0.00108$ for $S = 0.8$. The spectral weight at $\omega > 0$ starts to vanish for $S = 0.8$.

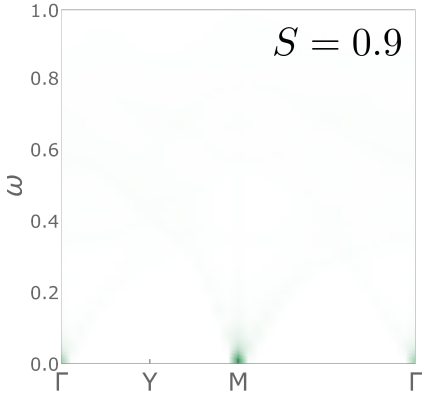

Figure C.5: Dynamical structure factors of the *cuboc1** ground state at $J = 0.2$ for $S = 0.9$. The ground state is gapless with $\Delta = 0.00038$ for $S = 0.9$ and no significant spectral weight above $\omega \simeq 0$ in the dynamical structure factor.

Let us start by monitoring the effects of an increased spin length on the disordered *cuboc1** ground state. We set $J = 0.2$ to ensure that we are in the region of stability of this ground state. We provide dynamical structure factors in figure C.3 for $S = 0.5$ and $S = 0.6$, in figure C.4 for $S = 0.7$ and $S = 0.8$ and in figure C.5 for $S = 0.9$.

First, for $S = 0.5$ and $S = 0.6$ (figure C.3), the gap of the *cuboc1** ground state remains open with $\Delta = 0.08675$ ($S = 0.5$) and $\Delta = 0.0486536$ ($S = 0.6$) after a finite size study. The structure factors remain quite similar.

Then, for $S = 0.7$ to $S = 0.9$ (figures C.4 and C.5), the ground state progressively becomes gapless with $\Delta = 0.00943$ ($S = 0.7$), $\Delta = 0.00108$ ($S = 0.8$) and $\Delta = 0.00038$ ($S = 0.9$). These values were difficult to obtain because of convergence issues due to Bose-Einstein condensation. For $S = 0.8$, most of the spectral weight for $\omega > 0$ has dissappeared, while it is still present for $S = 0.7$.

In conclusion, this preliminary study points to a destabilization of the *cuboc1** disordered ground state yielding a long-range order for $S > 0.7$.

Second, we take a look at the $\mathbf{Q} = 0$ spin-liquid ground state at $J = 0.4$ and try to determine the spin length needed to destabilize it. We start with $S = 0.5$ and progressively increase the spin length, yielding the dynamical structure factors of figures C.6 and C.7.

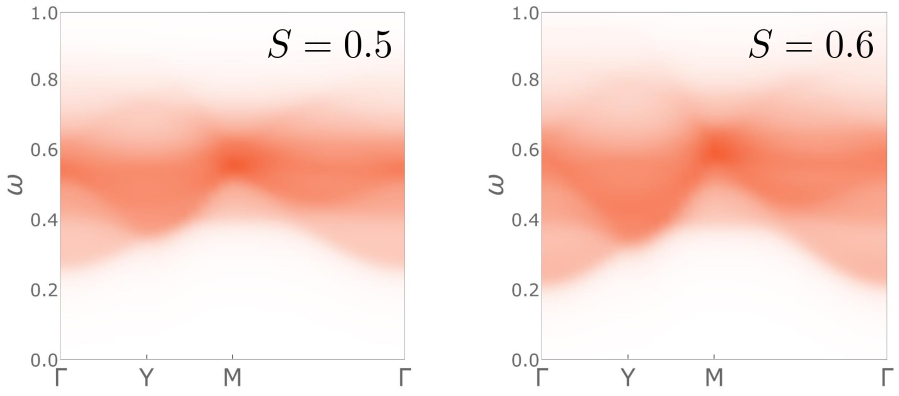

Figure C.6: Dynamical structure factors of the $\mathbf{Q} = 0$ ground state at $J = 0.4$ for a spin length of $S = 0.5$ (left) and $S = 0.6$ (right). The ground state remains gapped with $\Delta = 0.12946$ for $S = 0.5$ and $\Delta = 0.10597$ for $S = 0.6$.

From $S = 0.5$ to $S = 0.8$, the dynamical structure factor remain quite similar and the phase remains clearly gapped. Finite size studies indicate $\Delta = 0.12946$ for $S = 0.5$, $\Delta = 0.10597$ for $S = 0.6$, $\Delta = 0.08664$ for $S = 0.7$ and $\Delta = 0.07254$ for $S = 0.8$.

For $S = 0.9$, starting with the $\mathbf{Q} = 0$ *Ansatz* as inital condition, convergence is not reached during the SBMFT self-consistent procedure. This problem is very likely to be linked to the ordered nature of the $\mathbf{Q} = 0$ ground state at $S = 0.9$. A more thorough

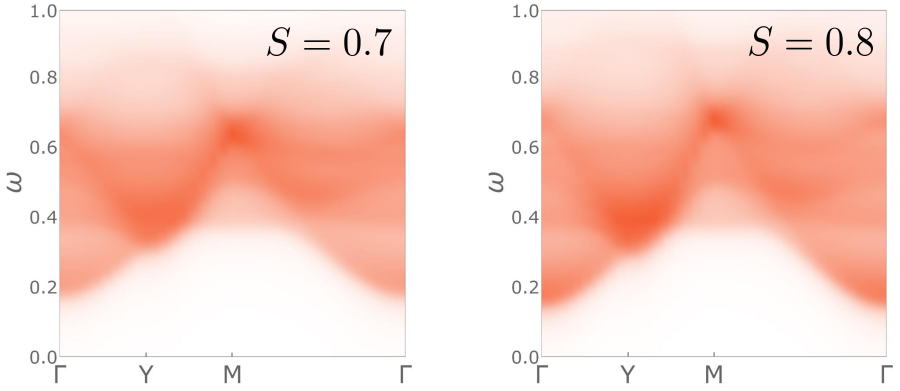

Figure C.7: Dynamical structure factors of the $\mathbf{Q} = 0$ ground state at $J = 0.4$ for a spin length of $S = 0.7$ (left) and $S = 0.8$ (right). The ground state remains gapped with $\Delta = 0.08664$ for $S = 0.7$ and $\Delta = 0.07254$ for $S = 0.8$.

study with thinner S steps could determine the exact value of S at which the gap closes to yield a long-range order. For now, we can assume that for $S > 0.8$ the $\mathbf{Q} = 0$ spin liquid is destabilized in favor of a long-range order.

Finally, starting from the *1H1R* ordered ground state at $S = 0.5$ and $J = 0.8$, we will this time decrease the spin length in order to destabilize the magnetic order and monitor the opening of the energy gap. Once again, dynamical structure factors are provided in figures C.8 for $S = 0.5$ and $S = 0.4$, in figure C.9 for $S = 0.3$ and $S = 0.2$ and in figure C.10 for $S = 0.1$.

From $S = 0.5$ to $S = 0.3$, there is no notable change on the dynamical structure factors. Moreover, these ground states are all gapless with finite size study pointing at a gapless phase within error bars of order 10^{-5} to 10^{-4}.

At $S = 0.2$, however, significant spectral weight for $\omega > 0$ appears and the finite size study of the gap seems to indicate a small gap opening with $\Delta = 0.00941$. This gap opening is further confirmed since for $S = 0.1$ we have $\Delta = 0.24696$. For this value of the spin length, the dynamical structure factor exhibits only one flat band at $\omega \approx 2\Delta$. In the end, it seems that the *1H1R* order is destabilized for $S > 0.2$.

In conclusion, we have found approximate spin length values that destabilize each of the three ground states at particular values of J. In the near future, this qualitative study could of course be carried out more precisely. First, by assessing the nature of each ground state for many more values of S and not just by steps of 0.1. Second, by taking into account that changing the spin length could lead to some modifications in the energy landscape. The right thing to do would then be to make sure to find the true ground state for each values of S and verifying if it corresponds to an ordered or disordered ground state.

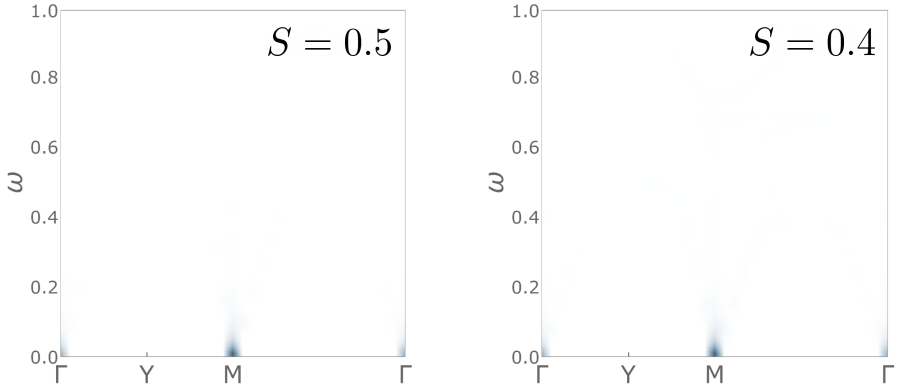

Figure C.8: Dynamical structure factors of the *1H1R* ground state at $J = 0.8$ for $S = 0.5$ (left) and $S = 0.4$ (right). Both ground states are gapless within error bars of 10^{-5} and the dynamical structure factors show no significant spectral weight above $\omega \simeq 0$.

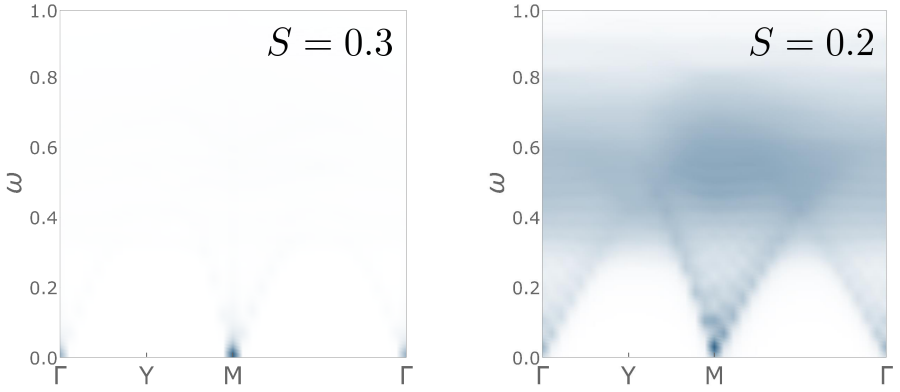

Figure C.9: Dynamical structure factors of the *1H1R* ground state at $J = 0.8$ for $S = 0.3$ (left) and $S = 0.2$ (right). For $S = 0.3$, the ground state is gapless within error bars of 10^{-4} and the dynamical structure factor shows no significant spectral weight above $\omega \simeq 0$. For $S = 0.2$, however, there is a small gap opening with $\Delta = 0.00941$ and spectral weight at $\omega > 0$ appears in the structure factor.

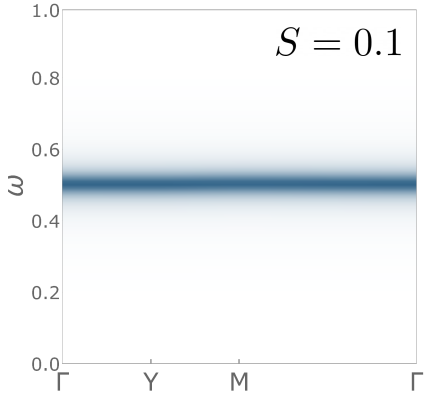

Figure C.10: Dynamical structure factor of the *1H1R* ground state at $J = 0.8$ for $S = 0.1$. The ground state is clearly gapped with $\Delta = 0.24696$ and the dynamical structure factor exhibits only one flat band at $\omega \approx 2\Delta$.

Appendix D

Résumé en français

Dans ce manuscrit, nous avons étudié les diagrammes de phase et les états fondamentaux de deux systèmes frustrés via la théorie des bosons de Schwinger en champ moyen (SBMFT). En sondant ces systèmes, nous avons recherché des états magnétiques exotiques tels que les liquides de spin quantiques, connu pour présenter des corrélations non conventionelles, des ordres cachés ainsi que des propriétés topologiques.

Dans le chapitre 1, nous avons d'abord présenté les concepts fondamentaux permettant de comprendre les effets de la frustration sur les systèmes magnétiques. Tout d'abord dans le cas classique, où nous avons décrit comment la frustration peut conduire à des dégénérescences extensives de l'état fondamental, par exemple sur le réseau kagomé. Nous avons ensuite décrit plusieurs phases magnétiques induites par la frustration en nous concentrant, pour le cas quantique, sur les cristaux de lien de valence et sur différents types de liquides de spin quantiques dans le cadre de la théorie RVB. Enfin, pour illustrer ces concepts, nous avons présenté des résultats récents sur deux systèmes concrets : les réseaux kagomé et square-kagomé.

Dans le chapitre 2, nous avons décrit en détail les outils théoriques et numériques nécessaires à la théorie des bosons de Schwinger en champ moyen. Nous avons d'abord commencé par décomposer l'hamiltonien de Heisenberg en termes d'opérateurs de spinon bosoniques avant d'effectuer un découplage champ moyen sur les opérateurs de liens $\hat{A}_{ij}$ et $\hat{B}_{ij}$. Ensuite, nous avons décrit comment diagonaliser le hamiltonien champ moyen via une transformation de Bogoliubov permettant de calculer l'énergie libre du système. Nous avons poursuivi avec une description de l'algorithme SBMFT en fournissant deux façons de résoudre les équations auto-cohérentes sur les paramètres champ moyen. Cet algorithme est décrit schématiquement sur la figure D.1. Nous avons également calculé dans le formalisme SBMFT plusieurs quantités physiques nécessaires à la caractérisation des différents états fondamentaux. Enfin, nous avons défini les opérateurs de boucle de

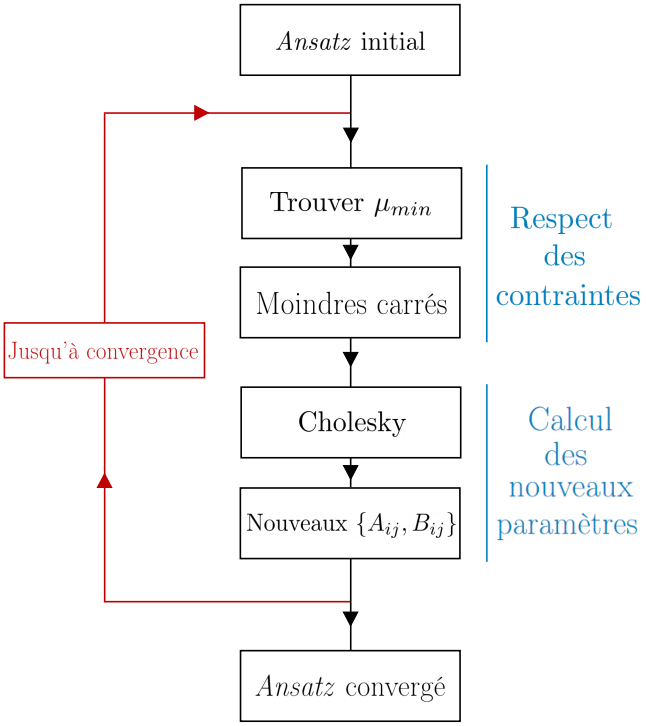

Figure D.1: Représentation schématique de l'algorithme auto-cohérent SBMFT. À partir d'un *Ansatz* initial, les multiplicateurs de Lagrange sont optimisés pour remplir les contraintes bosoniques. Ensuite, au moyen d'une décomposition de Cholesky, un nouvel ensemble de paramètres champ moyen est calculé dans le vide des bosons de Bogoliubov. Ce nouvel ensemble est comparé à l'ancien et la procédure se termine si la convergence est atteinte.

Wilson locales et les flux de jauge associés en montrant dans un exemple simple sur le réseau triangulaire comment ils peuvent être utilisés pour différencier des états liquide de spin.

Dans le chapitre 3, nous avons étudié le modèle de Heisenberg $J_1 - J_2$ sur le réseau square-kagomé en utilisant notre algorithme SBMFT. Nous avons calculé le diagramme de phase complet en fonction de $x = J_2/J_1$ et décrit les cinq états fondamentaux qui le composent. Tout d'abord, nous avons décrit la phase plaquette ainsi que l'ordre ferrimagnétique, déjà étudiés en [75]. Ces deux états sont les états fondamentaux de notre modèle pour les valeurs faibles et élevées de x respectivement. Nous avons ensuite décrit les deux ordres magnétiques incommensurables qui jouxtent l'état fondamental le plus intriguant de ce diagramme de phase : un liquide de spin nématique et topologique présentant des flux locaux non nuls. Nous avons approfondi la description de cet état fondamental en révélant explicitement sa dégénérescence topologique avant de discuter de la modification du diagramme de phase au-delà de l'approximation de champ moyen. Enfin, nous avons établi des liens avec l'études expérimentale sur le composé à la géométrie square-kagomé qui fut synthétisé en 2020 [6]. Pour ce faire, nous

avons tout d'abord calculé les facteurs de structure dynamiques pour chacun des états fondamentaux. Ces facteurs de structure dynamiques sont représentés en figure D.2. Nous avons enfin tenu compte d'une possible anisotropie entre les liens J_2 du réseau

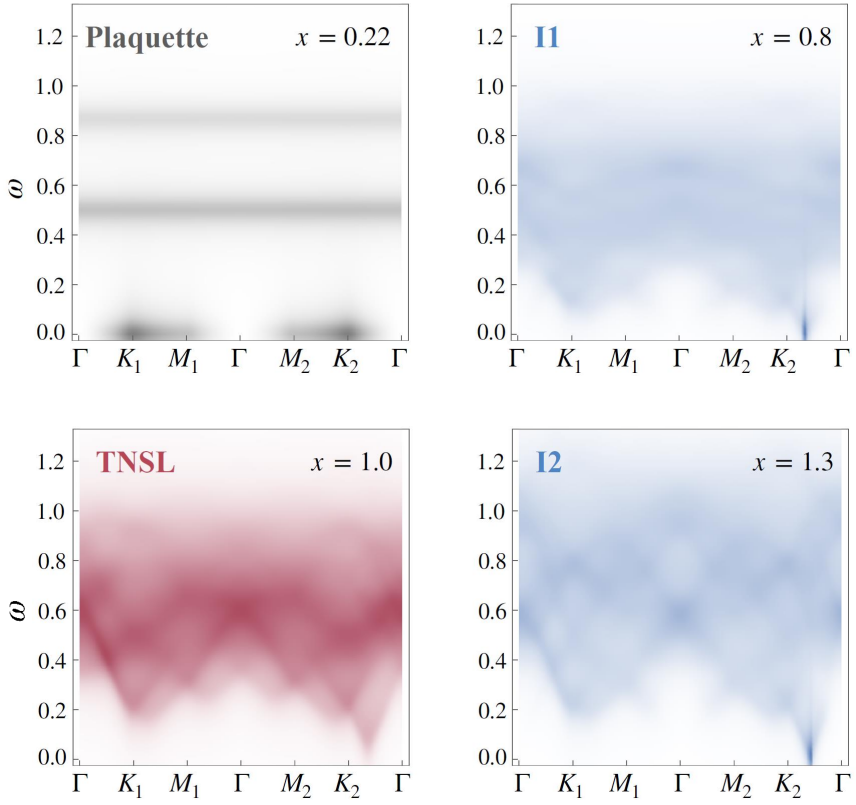

Figure D.2: Facteurs de structure dynamiques des états fondamentaux sur le réseau square-kagomé J_1-J_2. Le maximum de $S(\mathbf{k}, \omega)$ est fixé à l'unité pour chaque état fondamental. Les parties droite et gauche de chaque tracé correspondent à des chemins similaires dans la première zone de Brillouin, seulement différenciés par une rotation de $\pi/2$, ce qui permet d'observer une potentielle nématicité des états fondamentaux.

pour se rapprocher du modèle décrivant la physique du composé.

Dans le chapitre 4, nous avons étudié le modèle de Heisenberg $J_1 - J_2 - J_3$ sur le réseau kagomé, avec $J_2 = J_3 = J$, toujours via notre procédure auto-cohérente en bosons de Schwinger. Nous avons également fourni un diagramme de phase complet composé de trois états fondamentaux distincts. Le premier est un liquide de spin chiral issu de l'*Ansatz cuboc1* stable dans la région $0 < J < 1/3$. Le second est un état liquide de spin non-chiral issu de l'*Ansatz* $\mathbf{Q} = 0$ stable dans la région $1/3 < J < 1/2$. Enfin, le troisième état fondamental du modèle est un ordre chiral à longue portée issu de l'Ansatz *1H1R*. Là encore, nous avons fourni des signatures expérimentales de ces trois états fondamentaux en calculant leurs facteurs de structure statiques et dynamiques. Nous avons également montré que le point $J = 1/2$ possède des caractéristiques intéressantes. D'abord parce que nous pouvons avoir une intuition classique sur l'emplacement de la

frontière à ce point particulier. Ensuite, parce que pour $J > 1/2$, des états chiraux sont stabilisés: un état fondamental en partant de l'Ansatz *1H1R* et un état excité en partant de l'*Ansatz* $\mathbf{Q} = 0$. Enfin, nous avons calculé le facteur de structure statique de cet état excité chiral révèlant des motifs en demi-lune, une caractéristique également présente dans les études quantiques et classiques précédentes [113, 114, 122]. L'un des facteurs de structure statique présentant des demi-lunes est donné en figure D.3 pour $J = 0.6$.

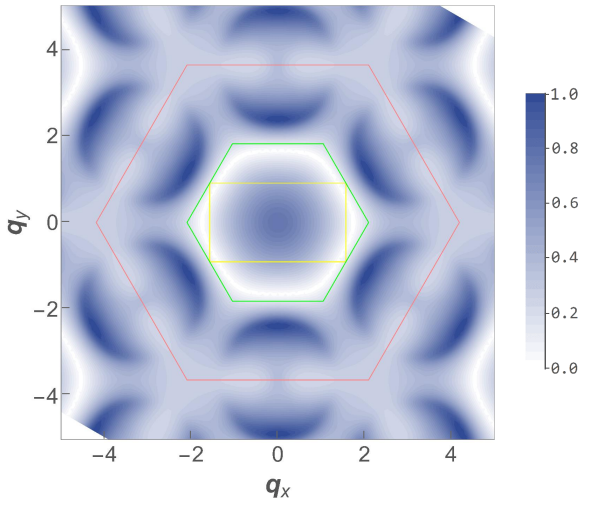

Figure D.3: Facteur de structure statique de l'état excité $\mathbf{Q} = \mathbf{0}$ chiral pour $J = 0.6$. Des demi-lunes de haute intensité apparaissent en dehors de la première zone de Brillouin du réseau kagomé.

Au final, nous avons révélé des diagrammes de phase riches et complexes comportant plusieurs états magnétiquement ordonnés ainsi que des liquides de spin quantiques pour les deux systèmes frustrés que nous avons étudiés. Bien sûr, plusieurs directions pourraient être explorées par la suite. Tout d'abord, l'ajustement de la théorie aux données expérimentales sur le matériau square-kagomé est primordial pour trouver l'hamiltonien décrivant ce matériau et la nature de la phase qui a été observée expérimentalement [6]. Pour ce faire, notre algorithme SBMFT auto-cohérent pourrait être étendu à d'autres modèles magnétiques et à d'autres types d'interactions tels que le modèle XXZ [84] ou l'interaction de Dzyaloshinskii-Moriya [85]. Deuxièmement, une autre direction intéressante serait de pouvoir décrire les deux systèmes frustrés que nous avons étudiés non plus seulement avec des excitations bosoniques, mais également avec des excitations fermioniques. Une façon de le faire serait de développer, en tant que contrepartie fermionique de notre algorithme SBMFT, une procédure auto-cohérente basée sur la théorie des fermions d'Abrikosov en champ moyen, permettant l'accès à de potentiels nouveaux états fondamentaux fermioniques. Avoir la possibilité de comparer les résultats fermioniques et bosoniques, en s'aidant également de classifications par

la méthode du groupe de symétrie projective [30, 86], serait d'un grand intérêt pour explorer davantage ces systèmes frustrés.

References

[1] G. Toulouse. Theory of the frustration effect in spin glasses. *Commun. Phys.*, 2:115, 1977.

[2] Linus Pauling. The structure and entropy of ice and of other crystals with some randomness of atomic arrangement. *Journal of the American Chemical Society*, 57(12):2680–2684, 1935.

[3] Steven T. Bramwell and Michel J.P. Gingras. Spin ice state in frustrated magnetic pyrochlore materials. *Science*, 294(5546):1495–1501, 2001.

[4] Steven T. Bramwell and Mark J. Harris. The history of spin ice. *Journal of Physics: Condensed Matter*, 32(37):374010, 2020.

[5] Matthew P. Shores, Emily A. Nytko, Bart M. Bartlett, and Daniel G. Nocera. A structurally perfect S=1/2 kagomé antiferromagnet. *Journal of the American Chemical Society*, 127(39):13462–13463, 2005.

[6] Masayoshi Fujihala, Katsuhiro Morita, Richard Mole, Setsuo Mitsuda, Takami Tohyama, Shinichiro Yano, Dehong Yu, Shigetoshi Sota, Tomohiko Kuwai, Akihiro Koda, et al. Gapless spin liquid in a square-kagome lattice antiferromagnet. *Nature communications*, 11(1):1–7, 2020.

[7] Nevill F. Mott. Metal-insulator transition. *Reviews of Modern Physics*, 40(4):677, 1968.

[8] G. H. Wannier. Antiferromagnetism. The triangular Ising net. *Physical Review*, 79(2):357–364, 1950.

[9] A.S. Wills, R. Ballou, and C. Lacroix. Model of localized highly frustrated ferromagnetism: The kagomé spin ice. *Physical Review B*, 66(14):144407, 2002.

[10] Christopher L. Henley. The "Coulomb phase" in frustrated systems. *Annu. Rev. Condens. Matter Phys.*, 1(1):179–210, 2010.

[11] Claudio Castelnovo, Roderich Moessner, and Shivaji L. Sondhi. Magnetic monopoles in spin ice. *Nature*, 451(7174):42–45, 2008.

[12] L.D.C. Jaubert and P.C.W. Holdsworth. Signature of magnetic monopole and Dirac string dynamics in spin ice. *Nature Physics*, 5(4):258–261, 2009.

[13] David A. Huse and Andrew D. Rutenberg. Classical antiferromagnets on the kagomé lattice. *Physical Review B*, 45(13):7536, 1992.

[14] I. Ritchey, P. Chandra, and P. Coleman. Spin folding in the two-dimensional Heisenberg kagomé antiferromagnet. *Physical Review B*, 47(22):15342, 1993.

[15] John T. Chalker, Peter C.W. Holdsworth, and E.F. Shender. Hidden order in a frustrated system: Properties of the Heisenberg kagomé antiferromagnet. *Physical Review Letters*, 68(6):855, 1992.

[16] Jan N. Reimers and A.J. Berlinsky. Order by disorder in the classical Heisenberg kagomé antiferromagnet. *Physical Review B*, 48(13):9539, 1993.

[17] Michael E. Zhitomirsky. Octupolar ordering of classical kagome antiferromagnets in two and three dimensions. *Physical Review B*, 78(9):094423, 2008.

[18] Amit Keren. Dynamical simulation of spins on kagomé and square lattices. *Physical Review Letters*, 72(20):3254, 1994.

[19] Julien Robert, Benjamin Canals, Virginie Simonet, and Rafik Ballou. Propagation and ghosts in the classical kagome antiferromagnet. *Physical Review Letters*, 101(11):117207, 2008.

[20] Mathieu Taillefumier, Julien Robert, Christopher L. Henley, Roderich Moessner, and Benjamin Canals. Semiclassical spin dynamics of the antiferromagnetic Heisenberg model on the kagome lattice. *Physical Review B*, 90(6):064419, 2014.

[21] Anders W. Sandvik. Finite-size scaling of the ground-state parameters of the two-dimensional Heisenberg model. *Physical Review B*, 56(18):11678, 1997.

[22] Matteo Calandra Buonaura and Sandro Sorella. Numerical study of the two-dimensional Heisenberg model using a green function Monte Carlo technique with a fixed number of walkers. *Physical Review B*, 57(18):11446, 1998.

[23] Alain Gellé, Andreas M. Läuchli, Brijesh Kumar, and Frédéric Mila. Two-dimensional quantum antiferromagnet with a fourfold degenerate dimer ground state. *Physical Review B*, 77(1):014419, 2008.

[24] Daniel S. Rokhsar and Steven A. Kivelson. Superconductivity and the quantum hard-core dimer gas. *Physical Review Letters*, 61(20):2376, 1988.

[25] Arnaud Ralko, Michel Ferrero, Federico Becca, Dmitri Ivanov, and Frédéric Mila. Zero-temperature properties of the quantum dimer model on the triangular lattice. *Physical Review B*, 71(22):224109, 2005.

[26] Philip W. Anderson. The resonating valence bond state in La_2CuO_4 and superconductivity. *Science*, 235(4793):1196–1198, 1987.

[27] Ganapathy Baskaran, Z. Zou, and Philip W. Anderson. The resonating valence bond state and high-T_c superconductivity—a mean field theory. *Solid state communications*, 63(11):973–976, 1987.

[28] Claire Lhuillier and Grégoire Misguich. Introduction to quantum spin liquids. In *Introduction to Frustrated Magnetism*, pages 23–41. Springer, 2011.

[29] Leon Balents. Spin liquids in frustrated magnets. *Nature*, 464(7286):199–208, 2010.

[30] Xiao-Gang Wen. Quantum orders and symmetric spin liquids. *Physical Review B*, 65(16):165113, 2002.

[31] Tarun Grover, N. Trivedi, T. Senthil, and Patrick A. Lee. Weak mott insulators on the triangular lattice: Possibility of a gapless nematic quantum spin liquid. *Physical Review B*, 81:245121, 2010.

[32] Laura Messio, Bernard Bernu, and Claire Lhuillier. Kagome antiferromagnet: a chiral topological spin liquid? *Physical Review Letters*, 108(20):207204, 2012.

[33] Ying Ran, Michael Hermele, Patrick A. Lee, and Xiao-Gang Wen. Projected-wave-function study of the spin-1/2 Heisenberg model on the kagomé lattice. *Physical Review Letters*, 98(11):117205, 2007.

[34] Michael Hermele, Ying Ran, Patrick A. Lee, and Xiao-Gang Wen. Properties of an algebraic spin liquid on the kagome lattice. *Physical Review B*, 77:224413, 2008.

[35] Y. Iqbal, F. Becca, and D. Poilblanc. Projected wave function study of Z_2 spin liquids on the kagome lattice for the spin-1/2 quantum Heisenberg antiferromagnet. *Physical Review B*, 84(2):020407(R), 2011.

[36] H. J. Liao, Z. Y. Xie, J. Chen, Z. Y. Liu, H. D. Xie, R. Z. Huang, B. Normand, and T. Xiang. Gapless spin-liquid ground state in the S=1/2 kagome antiferromagnet. *Physical Review Letters*, 118:137202, 2017.

[37] Yin-Chen He, Michael P. Zaletel, Masaki Oshikawa, and Frank Pollmann. Signatures of Dirac cones in a DMRG study of the kagome Heisenberg model. *Physical Review X*, 7:031020, 2017.

[38] Arnaud Ralko, Frédéric Mila, and Ioannis Rousochatzakis. Microscopic theory of the nearest-neighbor valence bond sector of the spin-1/2 kagome antiferromagnet. *Physical Review B*, 97(10):104401, 2018.

[39] Andreas M. Läuchli, Julien Sudan, and Roderich Moessner. S=1/2 kagome Heisenberg antiferromagnet revisited. *Physical Review B*, 100(15):155142, 2019.

[40] Simeng Yan, David A. Huse, and Steven R. White. Spin-liquid ground state of the $S = 1/2$ kagome Heisenberg antiferromagnet. *Science*, 332(6034):1173–1176, 2011.

[41] H.-C. Jiang, Z. Wang, and L. Balents. Identifying topological order by entanglement entropy. *Nature Physics*, 8:902–905, 2012.

[42] Stefan Depenbrock, Ian P. McCulloch, and Ulrich Schollwöck. Nature of the spin-liquid ground state of the $S = 1/2$ Heisenberg model on the kagome lattice. *Physical Review Letters*, 109:067201, 2012.

[43] Rajiv R.P. Singh and David A. Huse. Ground state of the spin-1/2 kagome-lattice Heisenberg antiferromagnet. *Physical Review B*, 76(18):180407, 2007.

[44] Glen Evenbly and Guifr Vidal. Frustrated antiferromagnets with entanglement renormalization: Ground state of the spin-1/2 Heisenberg model on a kagome lattice. *Physical Review Letters*, 104(18):187203, 2010.

[45] Didier Poilblanc and Grégoire Misguich. Competing valence bond crystals in the kagome quantum dimer model. *Physical Review B*, 84(21):214401, 2011.

[46] Mingxuan Fu, Takashi Imai, Tian-Heng Han, and Young S. Lee. Evidence for a gapped spin-liquid ground state in a kagome Heisenberg antiferromagnet. *Science*, 350(6261):655–658, 2015.

[47] P. Khuntia, M. Velázquez, Q. Barthélemy, F. Bert, E. Kermarrec, A. Legros, B. Bernu, L. Messio, A. Zorko, and P. Mendels. Gapless ground state in the archetypal quantum kagome antiferromagnet $ZnCu_3(OH)_6Cl_2$. *Nature Physics*, 16(4):469–474, 2020.

[48] A. Zorko, S. Nellutla, J. Van Tol, L.C. Brunel, F. Bert, F. Duc, J.-C. Trombe, M.A. De Vries, A. Harrison, and P. Mendels. Dzyaloshinsky-Moriya anisotropy in the spin$-1/2$ kagome compound $ZnCu_3(OH)_6Cl_2$. *Physical Review Letters*, 101(2):026405, 2008.

[49] S. El Shawish, O. Cepas, and S. Miyashita. Electron spin resonance in $S = 1/2$ antiferromagnets at high temperature. *Physical Review B*, 81(22):224421, 2010.

[50] M.A. de Vries, K.V. Kamenev, W.A. Kockelmann, J. Sanchez-Benitez, and A. Harrison. Magnetic ground state of an experimental $S = 1/2$ kagome antiferromagnet. *Physical Review Letters*, 100(15):157205, 2008.

[51] Yoshihiko Okamoto, Hiroyuki Yoshida, and Zenji Hiroi. Vesignieite $BaCu_3V_2O_8OH_2$ as a candidate spin-1/2 kagome antiferromagnet. *Journal of the Physical Society of Japan*, 78(3):033701–033701, 2009.

[52] Makoto Yoshida, Yoshihiko Okamoto, Masashi Takigawa, and Zenji Hiroi. Magnetic order in the spin-1/2 kagome antiferromagnet vesignieite. *Journal of the Physical Society of Japan*, 82(1):013702, 2012.

[53] R.H. Colman, F. Bert, D. Boldrin, A.D. Hillier, P. Manuel, P. Mendels, and A.S. Wills. Spin dynamics in the S=1/2 quantum kagome compound vesignieite, $BaCu_3V_2O_8OH_2$. *Physical Review B*, 83(18):180416, 2011.

[54] B. Fåk, E. Kermarrec, L. Messio, B. Bernu, C. Lhuillier, F. Bert, P. Mendels, B. Koteswararao, F. Bouquet, J. Ollivier, et al. Kapellasite: A kagome quantum spin liquid with competing interactions. *Physical Review Letters*, 109(3):037208, 2012.

[55] Hiroyuki Yoshida, Jun-ichi Yamaura, Masaaki Isobe, Yoshihiko Okamoto, Gøran J. Nilsen, and Zenji Hiroi. Orbital switching in a frustrated magnet. *Nature communications*, 3(1):1–5, 2012.

[56] K. Matan, T. Ono, Y. Fukumoto, T.J. Sato, J. Yamaura, M. Yano, K. Morita, and H. Tanaka. Pinwheel valence-bond solid and triplet excitations in the two-dimensional deformed kagome lattice. *Nature Physics*, 6(11):865–869, 2010.

[57] P. Lecheminant, B. Bernu, C. Lhuillier, L. Pierre, and P. Sindzingre. Order versus disorder in the quantum Heisenberg antiferromagnet on the kagomé lattice using exact spectra analysis. *Physical Review B*, 56(5):2521, 1997.

[58] C. Waldtmann, H.-U. Everts, B. Bernu, C. Lhuillier, P. Sindzingre, P. Lecheminant, and L. Pierre. First excitations of the spin-1/2 Heisenberg antiferromagnet on the kagomé lattice. *The European Physical Journal B-Condensed Matter and Complex Systems*, 2(4):501–507, 1998.

[59] P. Sindzingre, G. Misguich, C. Lhuillier, B. Bernu, L. Pierre, C. Waldtmann, and H.-U. Everts. Magnetothermodynamics of the spin-1/2 kagomé antiferromagnet. *Physical Review Letters*, 84(13):2953, 2000.

[60] Rahul Siddharthan and Antoine Georges. Square kagome quantum antiferromagnet and the eight-vertex model. *Physical Review B*, 65(1):014417, 2001.

[61] Johannes Richter, Oleg Derzhko, and Jörg Schulenburg. Magnetic-field induced spin-Peierls instability in strongly frustrated quantum spin lattices. *Physical Review Letters*, 93(10):107206, 2004.

[62] Oleg Derzhko, Johannes Richter, and Jörg Schulenburg. Structural distortions of frustrated quantum spin lattices in high magnetic fields. *physica status solidi (b)*, 242(15):3189–3194, 2005.

[63] O. Derzhko and J. Richter. Universal low-temperature behavior of frustrated quantum antiferromagnets in the vicinity of the saturation field. *The European Physical Journal B*, 52(1):23–36, 2006.

[64] J. Richter, J. Schulenburg, P. Tomczak, and D. Schmalfuss. The Heisenberg antiferromagnet on the square-kagomé lattice. *Condensed Matter Physics*, 12(3):507–517, 2009.

[65] Oleg Derzhko, Johannes Richter, Olesia Krupnitska, and Taras Krokhmalskii. Frustrated quantum Heisenberg antiferromagnets at high magnetic fields: Beyond the flat-band scenario. *Physical Review B*, 88:094426, 2013.

[66] Oleg Derzhko, Johannes Richter, Olesia Krupnitska, and Taras Krokhmalskii. The square-kagome quantum Heisenberg antiferromagnet at high magnetic fields: The localized-magnon paradigm and beyond. *Low Temperature Physics*, 40(6):513–520, 2014.

[67] Hiroki Nakano, Toru Sakai, and Yasumasa Hasegawa. Spin-flop phenomenon of two-dimensional frustrated antiferromagnets without anisotropy in spin space. *Journal of the Physical Society of Japan*, 83(8):084709, 2014.

[68] Arnaud Ralko and Ioannis Rousochatzakis. Resonating-valence-bond physics is not always governed by the shortest tunneling loops. *Physical Review Letters*, 115(16):167202, 2015.

[69] Yasumasa Hasegawa, Hiroki Nakano, and Tôru Sakai. Metamagnetic jump in the spin-$\frac{1}{2}$ antiferromagnetic Heisenberg model on the square kagome lattice. *Physical Review B*, 98:014404, 2018.

[70] Katsuhiro Morita and Takami Tohyama. Magnetic phase diagrams and magnetization plateaus of the spin-1/2 antiferromagnetic Heisenberg model on a square-kagome lattice with three nonequivalent exchange interactions. *Journal of the Physical Society of Japan*, 87(4):043704, 2018.

[71] Hiroki Nakano and Tôru Sakai. The two-dimensional $S = 1/2$ Heisenberg antiferromagnet on the shuriken lattice –A lattice composed of vertex-sharing triangles–. *Journal of the Physical Society of Japan*, 82(8):083709, 2013.

[72] Rico Pohle, Owen Benton, and L.D.C. Jaubert. Reentrance of disorder in the anisotropic shuriken Ising model. *Physical Review B*, 94(1):014429, 2016.

[73] Piotr Tomczak and Johannes Richter. Specific heat of the spin-$\frac{1}{2}$ Heisenberg antiferromagnet on squagome lattice. *Journal of Physics A*, 36(20):5399, 2003.

[74] A. W. Glaetzle, M. Dalmonte, R. Nath, I. Rousochatzakis, R. Moessner, and P. Zoller. Quantum spin-ice and dimer models with Rydberg atoms. *Physical Review X*, 4:041037, 2014.

[75] Ioannis Rousochatzakis, Roderich Moessner, and Jeroen van den Brink. Frustrated magnetism and resonating valence bond physics in two-dimensional kagome-like magnets. *Physical Review B*, 88(19):195109, 2013.

[76] Elliott H. Lieb. Two theorems on the Hubbard model. *Physical Review Letters*, 62(10):1201–1204, 1989.

[77] A.N. Berker and James S. Walker. Frustrated spin-gas model for doubly reentrant liquid crystals. *Physical Review Letters*, 47(20):1469, 1981.

[78] G. Aeppli, S.M. Shapiro, R.J. Birgeneau, and H.S. Chen. Spin correlations and reentrant spin-glass behavior in amorphous Fe-Mn alloys: Statics. *Physical Review B*, 28(9):5160, 1983.

[79] Erhai Zhao and Arun Paramekanti. Self-consistent slave rotor mean-field theory for strongly correlated systems. *Physical Review B*, 76(19):195101, 2007.

[80] Assa Auerbach. *Interacting Electrons and Quantum Magnetism*. Springer-Verlag, Berlin, 1994.

[81] Subir Sachdev. Kagomé- and triangular-lattice Heisenberg antiferromagnets: Ordering from quantum fluctuations and quantum-disordered ground states with unconfined bosonic spinons. *Physical Review B*, 45(21):12377–12396, 1992.

[82] D.C. Cabra, C.A. Lamas, and H.D. Rosales. Quantum disordered phase on the frustrated honeycomb lattice. *Physical Review B*, 83(9):094506, 2011.

[83] H. Zhang and C.A. Lamas. Exotic disordered phases in the quantum $J_1 - J_2$ model on the honeycomb lattice. *Physical Review B*, 87(2):024415, 2013.

[84] E.A. Ghioldi, A. Mezio, L.O. Manuel, R.R.P. Singh, J. Oitmaa, and A.E. Trumper. Magnons and excitation continuum in XXZ triangular antiferromagnetic model: application to $Ba_3CoSb_2O_9$. *Physical Review B*, 91(13):134423, 2015.

[85] Laura Messio, Olivier Cepas, and Claire Lhuillier. Schwinger-boson approach to the kagome antiferromagnet with Dzyaloshinskii-Moriya interactions: Phase diagram and dynamical structure factors. *Physical Review B*, 81(6):064428, 2010.

[86] Fa Wang and Ashvin Vishwanath. Spin-liquid states on the triangular and kagomé lattices: A projective-symmetry-group analysis of Schwinger boson states. *Physical Review B*, 74(17):174423, 2006.

[87] Fa Wang. Schwinger boson mean field theories of spin liquid states on a honeycomb lattice: Projective symmetry group analysis and critical field theory. *Physical Review B*, 82(2):024419, 2010.

[88] Laura Messio, Claire Lhuillier, and Grégoire Misguich. Time reversal symmetry breaking chiral spin liquids: Projective symmetry group approach of bosonic mean-field theories. *Physical Review B*, 87(12):125127, 2013.

[89] Grégoire Misguich. Quantum spin liquids and fractionalization. In *Introduction to Frustrated Magnetism*, pages 407–435. Springer, 2011.

[90] R. Flint and P. Coleman. Symplectic N and time reversal in frustrated magnetism. *Physical Review B*, 79(1):014424, 2009.

[91] A. Mezio, C.N. Sposetti, L.O. Manuel, and A.E. Trumper. A test of the bosonic spinon theory for the triangular antiferromagnet spectrum. *EPL (Europhysics Letters)*, 94(4):47001, 2011.

[92] N. Bogoliubov. On the theory of superfluidity. *J. Phys*, 11(1):23, 1947.

[93] D.V. Bauer and J.O. Fjærestad. Schwinger-boson mean-field study of the $J_1 - J_2$ Heisenberg quantum antiferromagnet on the triangular lattice. *Physical Review B*, 96(16):165141, 2017.

[94] Laura Messio, Samuel Bieri, Claire Lhuillier, and Bernard Bernu. Chiral spin liquid on a kagome antiferromagnet induced by the Dzyaloshinskii-Moriya interaction. *Physical Review Letters*, 118(26):267201, 2017.

[95] Jad C. Halimeh and Matthias Punk. Spin structure factors of chiral quantum spin liquids on the kagome lattice. *Physical Review B*, 94(10):104413, 2016.

[96] J.H.P. Colpa. Diagonalization of the quadratic boson hamiltonian. *Physica A*, 93(3-4):327–353, 1978.

[97] S. Toth and B. Lake. Linear spin wave theory for single-Q incommensurate magnetic structures. *Journal of Physics: Condensed Matter*, 27(16):166002, 2015.

[98] Xu Yang and Fa Wang. Schwinger boson spin-liquid states on square lattice. *Physical Review B*, 94(3):035160, 2016.

[99] Chunxiao Liu, Gábor B. Halász, and Leon Balents. Competing orders in pyrochlore magnets from a Z_2 spin liquid perspective. *Physical Review B*, 100(7):075125, 2019.

[100] Hui-Ke Jin and Yi Zhou. Classical and quantum order in hyperkagome antiferromagnets. *Physical Review B*, 101(5):054408, 2020.

[101] Yuan-Ming Lu. Symmetric Z_2 spin liquids and their neighboring phases on triangular lattice. *Physical Review B*, 93(16):165113, 2016.

[102] Tristan Lugan, L.D.C. Jaubert, and Arnaud Ralko. Topological nematic spin liquid on the square kagome lattice. *Physical Review Research*, 1(3):033147, 2019.

[103] P. Chandra, P. Coleman, and I. Ritchey. The anisotropic kagome antiferromagnet: a topological spin glass? *Journal de Physique I*, 3(2):591–610, 1993.

[104] H. Feldner, D.C. Cabra, and G.L. Rossini. Ferromagnetic frustrated spin systems on the square lattice: Schwinger boson study. *Physical Review B*, 84(21):214406, 2011.

[105] Philippe Sindzingre, Nic Shannon, and Tsutomu Momoi. Phase diagram of the spin-1/2 $J_1 - J_2 - J_3$ Heisenberg model on the square lattice. *Journal of Physics: Conference Series*, 200(2):022058, 2010.

[106] Samuel Bieri, Claire Lhuillier, and Laura Messio. Projective symmetry group classification of chiral spin liquids. *Physical Review B*, 93(9):094437, 2016.

[107] R. Moessner and Shivaji Lal Sondhi. Ising models of quantum frustration. *Physical Review B*, 63(22):224401, 2001.

[108] G. Misguich, D. Serban, and V. Pasquier. Quantum dimer model on the kagome lattice: Solvable dimer-liquid and Ising gauge theory. *Physical Review Letters*, 89(13):137202, 2002.

[109] Arnaud Ralko, Michel Ferrero, Federico Becca, Dmitri Ivanov, and Frédéric Mila. Dynamics of the quantum dimer model on the triangular lattice: Soft modes and local resonating valence-bond correlations. *Physical Review B*, 74(13):134301, 2006.

[110] C. Castelnovo, R. Moessner, and S. L. Sondhi. Spin ice, fractionalization, and topological order. *Annual Review of Condensed Matter Physics*, 3:35–55, 2012.

[111] Tom Fennell, P.P. Deen, A.R. Wildes, K. Schmalzl, D. Prabhakaran, A.T. Boothroyd, R.J. Aldus, D.F. McMorrow, and S.T. Bramwell. Magnetic Coulomb phase in the spin ice $Ho_2Ti_2O_7$. *Science*, 326(5951):415–417, 2009.

[112] D.A. Garanin and Benjamin Canals. Classical spin liquid: Exact solution for the infinite-component antiferromagnetic model on the kagomé lattice. *Physical Review B*, 59(1):443, 1999.

[113] Tomonari Mizoguchi, L.D.C. Jaubert, and Masafumi Udagawa. Clustering of topological charges in a kagome classical spin liquid. *Physical Review Letters*, 119(7):077207, 2017.

[114] Tomonari Mizoguchi, L.D.C. Jaubert, Roderich Moessner, and Masafumi Udagawa. Magnetic clustering, half-moons, and shadow pinch points as signals of a proximate Coulomb phase in frustrated Heisenberg magnets. *Physical Review B*, 98(14):144446, 2018.

[115] Leon Balents, Matthew P.A. Fisher, and Steven M. Girvin. Fractionalization in an easy-axis kagome antiferromagnet. *Physical Review B*, 65(22):224412, 2002.

[116] S.V. Isakov, Yong Baek Kim, and Arun Paramekanti. Spin-liquid phase in a spin-1/2 quantum magnet on the kagome lattice. *Physical Review Letters*, 97(20):207204, 2006.

[117] Yin-Chen He, D.N. Sheng, and Yan Chen. Chiral spin liquid in a frustrated anisotropic kagome Heisenberg model. *Physical Review Letters*, 112(13):137202, 2014.

[118] Samuel Bieri, Laura Messio, Bernard Bernu, and Claire Lhuillier. Gapless chiral spin liquid in a kagome Heisenberg model. *Physical Review B*, 92(6):060407, 2015.

[119] Yasir Iqbal, Harald O. Jeschke, Johannes Reuther, Roser Valentí, I.I. Mazin, Martin Greiter, and Ronny Thomale. Paramagnetism in the kagome compounds $(Zn, Mg, Cd)Cu_3(OH)_6Cl_2$. *Physical Review B*, 92(22):220404, 2015.

[120] F.A. Gómez Albarracín and Pierre Pujol. Degenerate and chiral states in the extended Heisenberg model on the kagome lattice. *Physical Review B*, 97(10):104419, 2018.

[121] Tao Li. A continuous family of fully frustrated Heisenberg models on the kagome lattice. *EPL (Europhysics Letters)*, 133(4):47001, 2021.

[122] Finn Lasse Buessen and Simon Trebst. Competing magnetic orders and spin liquids in two-and three-dimensional kagome systems: Pseudofermion functional renormalization group perspective. *Physical Review B*, 94(23):235138, 2016.

[123] Han Yan, Rico Pohle, and Nic Shannon. Half moons are pinch points with dispersion. *Physical Review B*, 98(14):140402, 2018.

[124] Robert Schaffer, Yejin Huh, Kyusung Hwang, and Yong Baek Kim. Quantum spin liquid in a breathing kagome lattice. *Physical Review B*, 95(5):054410, 2017.

[125] Tom Fennell, Michel Kenzelmann, Bertrand Roessli, M.K. Haas, and Robert Joseph Cava. Power-law spin correlations in the pyrochlore antiferromagnet $Tb_2Ti_2O_7$. *Physical Review Letters*, 109(1):017201, 2012.

[126] Romain Sibille, Nicolas Gauthier, Han Yan, Monica Ciomaga Hatnean, Jacques Ollivier, Barry Winn, Uwe Filges, Geetha Balakrishnan, Michel Kenzelmann, Nic Shannon, et al. Experimental signatures of emergent quantum electrodynamics in $Pr_2Hf_2O_7$. *Nature Physics*, 14(7):711–715, 2018.

[127] Solène Guitteny, Julien Robert, Pierre Bonville, Jacques Ollivier, Claudia Decorse, Paul Steffens, Martin Boehm, Hannu Mutka, Isabelle Mirebeau, and Sylvain Petit. Anisotropic propagating excitations and quadrupolar effects in $Tb_2Ti_2O_7$. *Physical Review Letters*, 111(8):087201, 2013.

[128] Shu Zhang, Hitesh J. Changlani, Kemp W. Plumb, Oleg Tchernyshyov, and Roderich Moessner. Dynamical structure factor of the three-dimensional quantum spin liquid candidate $NaCaNi_2F_7$. *Physical Review Letters*, 122(16):167203, 2019.

[129] E. Lhotel, S. Petit, M. C. Hatnean, J. Ollivier, H. Mutka, E. Ressouche, M.R. Lees, and G. Balakrishnan. Evidence for dynamic kagome ice. *Nature communications*, 9(1):1–6, 2018.

[130] Rico Pohle, Han Yan, and Nic Shannon. How many spin liquids are there in $Ca_{10}Cr_7O_{28}$? *arXiv preprint arXiv:1711.03778*, 2017.

[131] Christian Balz, Bella Lake, Johannes Reuther, Hubertus Luetkens, Rico Schönemann, Thomas Herrmannsdörfer, Yogesh Singh, A.T.M Nazmul Islam, Elisa M. Wheeler, Jose A. Rodriguez-Rivera, et al. Physical realization of a quantum spin liquid based on a complex frustration mechanism. *Nature Physics*, 12(10):942–949, 2016.

Résumé

Le magnétisme quantique frustré a attiré beaucoup d'attention au cours des dernières décennies, en particulier due à la possibilité de trouver des systèmes hébergeant des états magnétiques exotiques tels que des liquides de spin quantiques présentant des excitations fractionnaires et des propriétés topologiques. Une manière d'étudier ces phases liquides de spins est d'effectuer une construction en parton de l'hamiltonien de Heisenberg quantique. Cette méthode de type champ moyen possède le précieux avantage de traiter sur un pied d'égalité les états magnétiquement ordonnés et les états de type liquide de spin. Dans le cadre de cette thèse, nous avons employé une telle méthode basée sur la théorie des bosons de Schwinger en champ moyen (SBMFT) afin d'étudier deux systèmes magnétiquement frustrés. Après une brève introduction de concepts fondamentaux en frustration magnétique dans le chapitre 1, nous présenterons la théorie des bosons de Schwinger et les outils numériques associés dans le chapitre 2. Dans le chapitre 3, nous présenterons le diagramme de phase complet du modèle de Heisenberg $J_1 - J_2$ sur le réseau square-kagome. Ce dernier comporte un état fondamental particulièrement intéressant : un liquide de spin nématique et topologique. Nous établirons ensuite des liens avec un composé récemment synthétisé présentant une géométrie square-kagome. Dans le dernier chapitre de ce manuscrit, nous nous tournerons vers le modèle de Heisenberg $J_1 - J_2 - J_3$ sur le réseau kagome dans le cas où $J_2 = J_3 = J$. Une fois encore, un diagramme de phase complet est obtenu grâce à notre procédure SBMFT auto-cohérente. Il est composé de trois états fondamentaux distincts : un liquide de spin chiral pour $J < 1/3$, un ordre chiral à longue portée pour $J > 1/2$ et un liquide de spin régulier dans la région intermédiaire. Nous établirons enfin des liens avec les précédentes études quantiques et classiques, notamment en discutant de la présence de motifs en demi-lune dans le facteur de structure statique d'un état excité du modèle pour $J > 1/2$. En conclusion, nous avons révélé des diagrammes de phase à la fois riches et complexes présentant divers états exotiques de type liquide de spin sur les deux systèmes frustrés étudiés dans ce manuscrit.
Mots-clefs : Magnétisme quantique, Théorie et numérique, Matière condensée

Abstract

Frustrated quantum magnets have received a lot of attention in the past decades for they are expected to host exotic magnetic states such as quantum spin liquids exhibiting fractionalized excitations and topological properties. One way to study these spin liquid phases is to perform a parton construction of the quantum Heisenberg Hamiltonian. This mean-field method has the valuable advantage of treating magnetically ordered states and spin-liquid states on an equal footing. In this thesis, we have employed such a method based on the Schwinger boson mean-field theory (SBMFT) to study two magnetically frustrated systems. After a brief introduction of the core concepts behind frustrated magnetic systems in chapter 1, we will introduce the Schwinger boson theory and the associated numerical tools in chapter 2. In chapter 3, we will present the full phase diagram of the $J_1 - J_2$ Heisenberg model on the square-kagome lattice with a particurlarly interesting ground state in the form of a topological nematic spin liquid. We will then make connections with a recently synthesized compound exhibiting perfect square-kagome geometry. In the final chapter of this manuscript, we will turn to the $J_1 - J_2 - J_3$ Heisenberg model on the kagome lattice in the case where $J_2 = J_3 = J$. Once again, a full phase diagram is obtained thanks to our SBMFT self-consistent procedure. It is composed of three distinct ground states: a chiral spin liquid for $J < 1/3$, a chiral long-range order for $J > 1/2$ and a symmetric spin liquid in between. Finally, we will make connections with previous quantum and classical works, especially by discussing the presence of half-moon patterns in the static structure factor of an excited state of the model for $J > 1/2$. In conclusion, we have revealed both rich and complex phase diagrams presenting various exotic spin-liquid states on the two frustrated systems studied in this manuscript.
Keywords: Quantum magnetism, Theory and numerics, Condensed Matter